Master's thesis

2019

Kaia Ingerdatter Sørland

NTNU
Norwegian University of
Science and Technology
Faculty of Natural Sciences
Department of Physics

Kaia Ingerdatter Sørland

The spoiler recovery CEST: A new approach for shortening the acquisition time

SR-CEST for characterization of CEST agents in solution using Bloch-McConnell fitting

June 2019

NTNU
Norwegian University of
Science and Technology

NTNU
Norwegian University of
Science and Technology

NTNU
Norwegian University of
Science and Technology

The spoiler recovery CEST: A new approach for shortening the acquisition time

SR-CEST for characterization of CEST agents in solution using Bloch-McConnell fitting

Kaia Ingerdatter Sørland

Master of Science in Applied Physics and Mathematics
Submission date: June 2019
Supervisor: Pål Erik Goa
Co-supervisor: Trygve Andreassen, Maria Tunset Grinde

Norwegian University of Science and Technology
Department of Physics

Abstract

Nuclear magnetic resonance (NMR) is a tool for investigating matter, where the magnetic processes occurring even on the atomic level are well described. Chemical exchange saturation transfer (CEST) is, among many, a novel and emerging NMR technique, intended to produce image contrast. CEST imaging and spectroscopy uses selective saturation of exchangeable protons to indirectly detect dilute labile protons via bulk water signal changes. This offers a substantial enhancement of sensitivity, which has led to numerous biomedical applications. In this work a regular CEST pulse sequence is combined with a spoiler recovery (SR) approach, giving a new and faster SR-CEST sequence to create CEST spectra. This combination can reduce the spectral acquisition time by more than 70%, without any significant impairment in the quality of the spectra. The conventional approach to analyze CEST spectra is a magnetic transfer ratio asymmetry analysis. This approach neglects effects often concomitant to CEST, such as nuclear Overhauser effects and semi-solid macromolecular magnetization transfer. In this work the Bloch-McConnell (BM) equations is least square curve fitted to CEST spectra from creatine, myo-inositol and glutamate samples. This BM fitting separates the CEST effect from the concomitant effects, and provides several physical characteristics of the CEST agents. The estimated parameters of most importance are the exchange rate between the CEST agent and surrounding bulk water, and the concentration of the CEST agent. Both are promising biomarkers for detection of diseases and monitoring effects of treatment. The CEST spectra to fit in this work was acquired for aqueous samples containing known metabolite concentrations on a 600 MHz NMR spectrometer. For aqueous samples at high static fields the longitudinal relaxation time T_1 of the water protons become very long, leading to long acquisition times. The SR-CEST sequence can therefore be particularly useful for these types of samples. The BM fitting of the SR-CEST spectra and regular CEST spectra provides overall the same estimated parameters as output, and succeeds in separating the different CEST effects. Due to the reduced aquisition time, SR-CEST is thus a promising tool for CEST MRI. Improvements in spectral acquisition and BM fitting is discussed based on the results

obtained, as well as the practical utility of SR-CEST and BM fitting for *in vivo* MRI.

Sammendrag

Kjernemagnetisk resonans (NMR) er en utbredt metode for å undersøke materie, hvor de magnetiske prosessene som skjer selv på atomnivå er godt beskrevet. Kjemisk utveksling av metning (CEST) er en forholdsvis ny og fremvoksende teknikk innen NMR, utviklet for å produsere bedre kontrast ved magnetresonanstomografi (MRI). I CEST MRI og spektroskopi blir utvalgte protoner i såkalte CEST-agenter, for eksempel metabolitter, mettet. Disse mettede protonene kan bytte plass med protoner i bulkvannet, noe som gir en endring i bulkvannets netto magnetisering. Ved å se på denne endringen kan man med vesentlig økt sensitivitet måle tilstedeværelsen av ulike forbindelser indirekte, noe som kan utnyttes i en rekke nye biomedisinske applikasjoner. I dette arbeidet kombineres en vanlig CEST-pulssekvens med en spoiler recovery (SR)-sekvens. Dette har gitt den nye og raskere SR-CEST-sekvensen, som kan redusere tiden det tar å generere et CEST-spektrum med mer enn 70%, uten at kvaliteten i spektret svekkes nevneverdig. Analyse av CEST-spektre har konvensjonelt gått via en $\mathrm{MTR}_{\mathrm{asym}}$-analyse, som ser på asymmetrien i CEST-spektra som følge av utvekslingen av magnetisme. Denne tilnærmingen tar ikke hensyn til effekter som ofte skjer samtidig med CEST, som for eksempel kjerne-Overhauser-effekter (NOE) og semi-solid makromolekylær magnetiseringsoverføring (MT). I dette arbeidet er Bloch-McConnell(BM)-ligningene kurvetilpasset CEST-spektre for kreatin-, myo-inositol- og glutamatprøver med minste kvadraters metode. Denne BM-tilpasningen skiller CEST-effekten fra andre forstyrrende effekter, og estimerer flere av de fysiske egenskapene til CEST-agentene. De estimerte egenskapene med størst betydning er utvekslingsraten mellom vann- og CEST-agentproton, og konsentrasjonen av CEST-agentene. Begge er lovende biomarkører for å påvise sykdommer og overvåke effekter av sykdomsbehandling. CEST-spektra brukt i dette arbeidet ble laget for vandige prøver av kjente metabolittkonsentrasjoner med et 600 MHz NMR-spektrometer. For vandige prøver ved høye statiske felt blir den longitudinale relaksasjonsstiden T_1 for vannprotonene svært lang, noe som gir tidkrevende eksperiment. SR-CEST-sekvensen kan derfor være spesielt nyttig for prøver av denne typen. BM-tilpasning av SR-CEST-spektra

og vanlige CEST-spektra gir samlet sett de samme estimerte parameterne, og lykkes i å separere de ulike CEST-effektene. På grunn av den reduserte eksperimentelle tiden er SR-CEST dermed en lovende metode for CEST MRI. Forbedringer i eksperimentelt design og BM-tilpasning diskuteres basert på resultatene funnet her, samt den praktiske bruken av SR-CEST og BM-tilpasning for *in vivo* MRI.

Preface

The work leading to this thesis began in fall '18 when I did a project report on *in vitro* measurements of CEST at 600 MHz. Coming from a year of theoretical physics studies, I was happy to do this experimental work in collaboration with the MR Centre at ISB. Working with high field NMR research was new to me, and doing this without the guidance of my supervisor Trygve Andreassen at ISB would have been absolutely impossible.

In the course of this fall, it became apparent to me how immense the field of research within CEST is. When Christmas came, and I finished the report, I felt as though I had barely scratched the surface. Therefore I am content with being able to continue the project work in this thesis. Among the main concerns of the CEST work during fall, was how time-consuming the experiments were. This eventually led to the SR-CEST sequence, which I hope will be used in future research.

I would like to thank my supervisors Trygve Andreassen and Maria Tunset Grinde at ISB, for always being available to my questions. The SR-CEST sequence would also not have come to life had it not been for my dad, which is why he deserves a special thanks.

Table of Contents

Chapter 1

Introduction

Nuclear magnetic resonance (NMR) spectroscopy and imaging are noninvasive methods used to obtain information from nuclear spins in samples or in the body of animals and humans. This information can in a large variety of ways be connected to the properties, such as dynamics and abundance, of the substances under consideration. Magnetic resonance imaging (MRI) and spectroscopy (MRS) is commonly utilized in diagnostic medicine and biomedical research [1]. In this work proton NMR is considered, where it is the spins from ^{1}H-atoms that are detected. These are to a large extent found in water, but also in all other molecules containing hydrogen, including lipids, proteins and metabolites.

Often samples contain an abundance of water, and the signal from metabolites or other compounds of low concentration can be difficult to detect [2]. *In vivo* MRI and MRS have been used for more than three decades to monitor metabolic and physiologic processes, where one often aims at detecting these low concentration metabolites [3]. The presence of varying metabolites can indicate the state of tissue, and can be utilized in numerous ways. However, performing conventional MRS *in vivo* is limited by a low sensitivity, which results in a low spatial resolution [4].

Chemical exchange saturation transfer (CEST) is an effect utilized especially in MRI to enhance signal from solute protons of low concentration, which has sparked numerous biomedical applications [5]. It has been developed and employed in multiple clinical imaging research centers worldwide, and preliminary clinical CEST MRI studies have shown promising practical utility for evaluating cerebrovascular stroke [6], breast cancer [7], osteoarthritis [6], muscle physiology [6], lymphedema [6], sold tumors [6] and tumor metabolism [8], multiple sclerosis, and other neurological disorders [6].

In CEST selected protons on for instance metabolites are saturated, and their saturation is transferred to the abundance of surrounding water. As more saturation is transferred to

the water the sensitivity for detecting the selected protons is enhanced. The CEST effect is utilized to create CEST spectra, where low concentration metabolites such as creatine, glucose, myo-inositol, glutamate, glycogen, glycosaminoglycan and mobile proteins and peptides rich in amide protons can be detected [9, 10]. The main requirement is that the molecule contains protons that undergo chemical exchange. By further analyzing the CEST spectra one can find, among others, CEST agent concentrations and exchange rates, and through these detect changes in microenvironmental properties such as temperature and pH [5].

Creating a CEST spectrum for aqueous solutions at high fields is time consuming. To achieve quantitative CEST spectra a series of delays in the order of $5 \cdot T_1$ is required, giving a total acquisition time above 30 minutes for a single spectrum. In the current work a new CEST sequence is established. By combining a regular CEST sequence with a spoiler recovery approach the acquisition time can be reduced by more than 70%, without any significant reduction of signal to noise ratio [11]. In the spoiler recovery CEST (SR-CEST) sequence a set of radio frequency pulses and gradients are frequently applied to spoil the net nuclear magnetization in the system under consideration, substituting the delays of $5 \cdot T_1$.

CEST-MRI is a promising contrast agent *in vivo*, but *in vivo* CEST quantification is challenging due to several concomitant effects: While the selected protons in the CEST agent are saturated, other types of magnetization transfer than CEST can occur. These can be direct saturation of water, semisolid macromolecular magnetization transfer (MT) and nuclear Overhauser effects (NOE) [9], which makes separating and analyzing the CEST effect challenging. In samples with multiple CEST agents present the interpretation of the spectra can only be addressed when also the individual CEST effects originating from various metabolites are characterized [12].

In order to analyze the CEST contrast mechanisms and separating them from other overlapping effects, mathematical models with both numerical and analytical solutions have been established [5]. They involve the Bloch-McConnell (BM) equations, which are a set of linear equations describing how the net nuclear magnetization in a system changes during chemical exchange [13]. It is challenging to obtain the exact analytical solutions of the BM equations, and a set of approximations have to be made [14]. Alternatively, the BM equations can be solved numerically. This has been done here to fit CEST and SR-CEST spectra acquired on a Bruker Avance 600 MHz NMR spectrometer, for aqueous samples containing known concentrations of metabolites with hydroxyl, guanidinium or amino protons.

This numerical solution does not require approximations to solve the BM equations,

and provides information on the exchange rate, concentration, offset frequency and relaxation time parameters of the CEST agent or agents under consideration. Through the numerical BM fitting it can therefore be proven that the SR-CEST and the regular CEST yield the same information, and that SR-CEST can successfully be applied to reduce the acquisition time for CEST spectroscopy significantly.

Chapter 2

Theory

Nuclear magnetic resonance (NMR) is a phenomenon of high practical utility where the physics are well described. It origins in atoms with an odd number of nuclei in the presence of a magnetic field. In this thesis work the focus have been ^{1}H-NMR, where the hydrogen atom consisting of a nucleus with a single proton is utilized. In Section 2.1 a brief introduction to NMR is given to outline the basic theory and some main concepts used in chemical exchange saturation transfer (CEST) experiments. In Section 2.2 an introduction to CEST is given, and in Section 2.3 the spoiler recovery CEST sequence is introduced. Methods to analyze CEST spectra is considered in Section 2.4, including a presentation of the set of Bloch-McConnell equations and their numerical solution.

2.1 Introduction to nuclear magnetic resonance

In this section basic principles of nuclear magnetic resonance is treated. It is if not stated otherwise based on Chapter 1-2 in *Principles of Magnetic Resonance* by C. P. Slichter [15].

2.1.1 Classical treatment of motion of isolated spins

To understand what happens in NMR experiments, it is reasonable to begin with understanding how a single spin acts in a magnetic field. Consider a single spin with magnetic moment $\boldsymbol{\mu}$ in a magnetic field $\boldsymbol{H}$. The rate of change of the angular magnetic moment $\boldsymbol{J}$ is given by the torque acting on the spin

$$\frac{d\boldsymbol{J}}{dt} = \boldsymbol{\mu} \times \boldsymbol{H}. \tag{2.1}$$

The magnetic moment is given by the gyromagnetic ratio γ mulitplied by the angular magnetic moment, $\boldsymbol{\mu} = \gamma \boldsymbol{J}$. Using this relation Eq. 2.1 can be rewritten as

$$\frac{d\boldsymbol{\mu}}{dt} = \boldsymbol{\mu} \times (\gamma \boldsymbol{H}). \tag{2.2}$$

To solve the equation it is expedient to translate the problem to the rotating frame of reference: Consider a coordinate system consisting of three unit vectors $\boldsymbol{e_i}, i = 1, 2, 3$, rotating with an instantaneous angular velocity $\boldsymbol{\omega}$. By expressing $\boldsymbol{\mu}$ in terms of these unit vectors, and using that

$$\frac{d\boldsymbol{e_i}}{dt} = \boldsymbol{\omega} \times \boldsymbol{e_i}, \tag{2.3}$$

the time derivative of $\boldsymbol{\mu}$ can be written as

$$\frac{d\boldsymbol{\mu}}{dt} = \frac{d}{dt}(\mu_i \boldsymbol{e_i}) = \boldsymbol{e_i}\frac{d\mu_i}{dt} + \mu_i(\boldsymbol{\omega} \times \boldsymbol{e_i}) = \frac{\delta \boldsymbol{\mu}}{\delta t} + \boldsymbol{\omega} \times \boldsymbol{\mu}, \tag{2.4}$$

where $\frac{\delta \boldsymbol{\mu}}{\delta t}$ represents the time rate of change of $\boldsymbol{\mu}$ with respect to the coordinate system $\boldsymbol{e_i}$, and Einstein summation convention is used. Combining with Eq. 2.2 the relation

$$\frac{\delta \boldsymbol{\mu}}{\delta t} = \boldsymbol{\mu} \times (\boldsymbol{\omega} + \gamma \boldsymbol{H}) \tag{2.5}$$

is obtained. Letting $\boldsymbol{\mu}$ remain fixed with respect to the rotating frame it is clear that $\frac{\delta \boldsymbol{\mu}}{\delta t} = 0$. This gives

$$\boldsymbol{\omega} = -\gamma \boldsymbol{H}. \tag{2.6}$$

That is, $\boldsymbol{\mu}$ rotates at an angular velocity $\boldsymbol{\omega} = -\gamma \boldsymbol{H}$ with respect to the laboratory system. Letting $\boldsymbol{H}$ be a static field in one direction, $\boldsymbol{H} = H_0 \boldsymbol{e_3}$, the angular frequency $\omega_0 = \gamma H_0$ is obtained, also called the Larmor or resonance frequency.

It can be shown that treating the system quantum mechanically yields a similar equation, with the one exception that $\boldsymbol{\mu}$ is substituted with the expectation value $\langle \boldsymbol{\mu} \rangle$ [15, p. 19]. In other words, the expectation value of $\boldsymbol{\mu}$ obeys the classical equation of motion for $\boldsymbol{\mu}$. If the spins are assumed not to interact with each other, the equation can be extended to count for the quantum mechanical expectation value of the total magnetization of an ensemble of spins. Under the assumption of non-interacting spins the classical picture can therefore be used to describe the dynamics of the net magnetization of a system. Eq. 2.2 holds true for a time-dependent magnetic field $\boldsymbol{H}$, which means that the classical picture can even be used for studying effects produced by an alternating magnetic field.

2.1.2 Effect of alternating magnetic fields

During NMR experiments alternating magnetic fields are applied on an ensemble of spins, often under the name radio frequency (RF) pulses, and the physical description of their effect becomes important.

An alternating magnetic field $\boldsymbol{H}_1$ can be expressed as

$$\boldsymbol{H}_1(t) = H_1(\boldsymbol{e}_1 \cos(\omega_z t) + \boldsymbol{e}_2 \sin(\omega_z t)) \tag{2.7}$$

where ω_z can be either positive or negative. The field is broken down into two rotating components, where a negative sign of ω_z yields the component rotating clockwise, and a positive sign yields the counter-rotating component of the field.

The equation of motion of a single spin including the effects of both $\boldsymbol{H}_1(t)$ and the static field $\boldsymbol{H}_0 = H_0\boldsymbol{e}_3$ is then

$$\frac{d\boldsymbol{\mu}}{dt} = \boldsymbol{\mu} \times \gamma(\boldsymbol{H}_0 + \boldsymbol{H}_1(t)), \tag{2.8}$$

where $\boldsymbol{H}_1(t)$ is assumed perpendicular to $\boldsymbol{H}_0$. Again it is convenient to transfer the problem to the rotating frame of reference. The time dependence of $\boldsymbol{H}_1$ can be eliminated by using a coordinate system that rotates about the direction of $\boldsymbol{H}_0$, referred to as z-direction, at frequency ω_z. In such a system $\boldsymbol{H}_1$ will be static. As will $\boldsymbol{H}_0$, as the axis of rotation coincides with the direction of $\boldsymbol{H}_0$. If one of the axes perpendicular to $\boldsymbol{H}_0$ is aligned with $\boldsymbol{H}_1$, referred to as the x-axis, the equation of motion (2.8) becomes

$$\frac{\delta\boldsymbol{\mu}}{\delta t} = \boldsymbol{\mu} \times [\boldsymbol{e}_3(\omega_z + \gamma H_0) + \boldsymbol{e}_1 \gamma H_1], \tag{2.9}$$

with $\boldsymbol{H}_1(t) = H_1(t)\boldsymbol{e}_1$. By choosing $\omega_z = -\omega$ this can be rewritten as

$$\frac{\delta\boldsymbol{\mu}}{\delta t} = \boldsymbol{\mu} \times \gamma[\boldsymbol{e}_3(H_0 - \frac{\omega}{\gamma}) + H_1\boldsymbol{e}_1] = \boldsymbol{\mu} \times \gamma\boldsymbol{H}_{\text{eff}}, \tag{2.10}$$

with

$$\boldsymbol{H}_{\text{eff}} = (H_0 - \frac{\omega}{\gamma})\boldsymbol{e}_3 + H_1\boldsymbol{e}_1. \tag{2.11}$$

This can be compared to Eq. 2.2, and physically it means that in the rotating frame of reference the magnetic moment acts as though it experiences a static magnetic field $\boldsymbol{H}_{\text{eff}}$. It will therefore precess in a cone of fixed angle about the direction of $\boldsymbol{H}_{\text{eff}}$, with an angular frequency γH_{eff}.

At resonance frequency $\omega = \gamma H_0$ the effective field is aligned in the x-direction, with

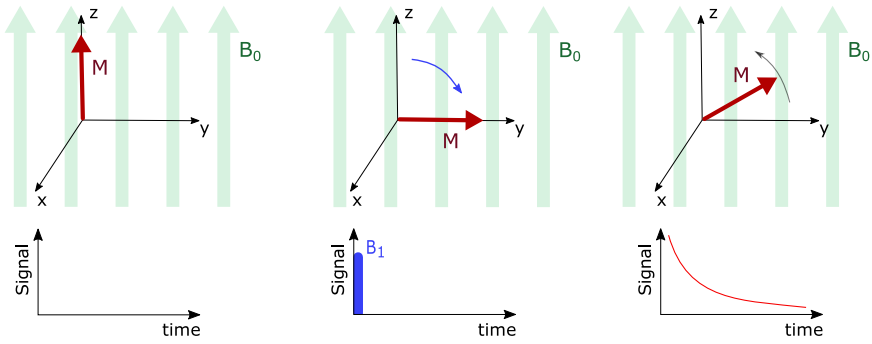

Figure 2.1: Simplified illustration of how the net magnetization vector $\boldsymbol{M}$ behaves in the rotating frame of reference under influence of both an external, constant magnetic field $\boldsymbol{B}_0$ in z-direction, and a magnetic field $\boldsymbol{B}_1(t)$ of well defined duration and amplitude in the x-direction. $\boldsymbol{M}$ is initially aligned with the z-direction, but after a perturbation it will be translated to the transverse plane. A $\boldsymbol{B}_1(t)$ in x-direction gives $\boldsymbol{M}$ in y-direction. Momentarily after the perturbation the magnetization vector begins to realign with $\boldsymbol{B}_0$, inducing an electric current giving out a detectable signal.

magnitude H_1. This means that a magnetic moment initially aligned along the static field will then precess perpendicular to $\boldsymbol{H}_1$ in the y-z plane. At times it will be opposed to $\boldsymbol{H}_0$, and at times lined up in the same direction. If $\boldsymbol{H}_1$ is applied for a defined time t_ω, the angle of $\boldsymbol{\mu}$ relative to the z-direction is given by

$$\theta = \gamma H_1 t_\omega, \tag{2.12}$$

as $\boldsymbol{H}_1$ is treated as a constant in the rotating frame of reference. This angle is often referred to as the flip angle. By adjusting the magnetic field strength and duration of the pulse the direction of $\boldsymbol{\mu}$ can then be controlled. If t_ω is chosen such that $\theta = \pi$ the moment is inverted. This is called a "180 degree pulse". For a 90 degree pulse ($\theta = \pi/2$) the magnetic moment is turned to align with the y-axis (see Fig. 2.1) in the rotating frame of reference. Considering the laboratory frame of reference, the moment will precess in the x-y-plane, normal to the static field $\boldsymbol{H}_0$.

To utilize this theory, an ensemble of spins has to be considered, as that is what is detectable in NMR experiments. In an external magnetic field $\boldsymbol{H}_0$ the spins in the ensemble will split into two states: one low energy state with spins aligned with the field (state α), and one higher energy state with spins aligned against the field (state β). The energy difference between these states are proportional to the resonance frequency of the spins, and there is a slight overweight of spins in state α. This causes a net magnetization

$\boldsymbol{M} = \chi_0 \boldsymbol{H} = \chi_0 \boldsymbol{H}_0$, with χ_0 being the magnetic susceptibility. As stated in Section 2.1.1, the classical description for $\boldsymbol{\mu}$ can under some assumptions also be applied to $\boldsymbol{M}$. A simplified illustration of the behaviour of this magnetization vector is found in Fig. 2.1.

The process of using an RF field $\boldsymbol{H}_1$ to change direction of $\boldsymbol{M}$ will later be referred to as excitation of spins. The magnetic field strength will in the following also be referred to in terms of the magnetic induction $\boldsymbol{B} = \mu \boldsymbol{H}$, with μ as the magnetic permeability.

2.1.3 Relaxation processes

An ensemble of spins that has been subject to an RF excitation pulse as described above, will be subject to relaxation processes. Using a 90 degree excitation pulse as an example, the ensemble of spins will in the rotating frame of reference be completely aligned with the y-axis after the pulse (see Fig. 2.1). It will not remain there, but gradually move towards again being aligned with the static field $\boldsymbol{B}_0$ at thermal equilibrium. This process is described by two relaxation constants, namely T_1 and T_2.

2.1.3.1 Longitudinal relaxation

After the perturbation from $\boldsymbol{B}_1$ the net magnetization will move towards thermal equilibrium and alignment with $\boldsymbol{B}_0$. The behaviour of the longitudinal magnetization (magnetization in z-direction) in time can be described by the equation

$$\frac{dM_z}{dt} = \frac{M_0 - M_z}{T_1}, \tag{2.13}$$

which is referred to as one of the Bloch equations. M_0 is the thermal equilibrium net magnetization and T_1 is the exponential time constant of the process. T_1 depends on the nuclear isotope and the sample, including parameters such as temperature and viscosity if the sample is a liquid [1, p. 33]. The solution of Eq. 2.13 is given by [1, p. 32]

$$M_z(t) = M_0(1 - e^{-t/T_1}), \tag{2.14}$$

where t is the time after the applied RF pulse. This means that at $t = T_1$ about 63% of the thermal equilibrium net magnetization is regained. After $t = 5 \cdot T_1$ one often assume that the system has returned to equilibrium, as seen in Figure 2.2.

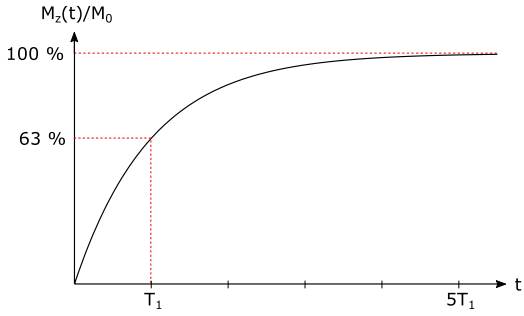

Figure 2.2: The build-up of longitudinal net magnetization when the initial condition is no net magnetization in z-direction in the presence of an external magnetic field $\boldsymbol{B}_0 = B_0\hat{\boldsymbol{z}}$. The curve follows the equation $M_z(t) = M_0(1 - e^{-t/T_1})$, where $M_z(t)$ is the time dependent net magnetization in z-direction, M_0 is the thermal equilibrium net magnetization and T_1 is the exponential time constant of the process.

2.1.3.2 Transversal relaxation

The return of $\boldsymbol{M}$ to equilibrium consists of more than restoration of its longitudinal component, it also consists of destruction of the transverse component (magnetization in the x-y-plane). Excited spins in the laboratory frame of reference will precess in the x-y-plane at a frequency given by Eq. 2.10. So far all protons are considered to experience the same external magnetic field $\boldsymbol{B}_0$, and thus precess with the same resonance frequency. This turns out to be incorrect for most substances. Although macroscopically homogeneous, the microscopic environment of protons can cause perturbations in $\boldsymbol{B}_0$, making protons at different sites experience slightly different fields. This in turn makes the spins precess at slightly different frequencies. Initially the ensemble of spins will precess synchronically, giving a well defined net transverse magnetization. As time passes, the frequency differences between the spins will cause a dephasing between them and the net transverse magnetization decreases. In its simplest form, this transverse magnetization decay can in the laboratory frame of reference be described by the Bloch equations

$$\frac{dM_x}{dt} = \gamma(\boldsymbol{M} \times \boldsymbol{B})_x - \frac{M_x}{T_2} \tag{2.15}$$

$$\frac{dM_y}{dt} = \gamma(\boldsymbol{M} \times \boldsymbol{B})_y - \frac{M_y}{T_2}, \tag{2.16}$$

where $\boldsymbol{B}$ is the magnetic field experienced by the nuclei, and T_2 is the transverse relaxation time constant, different from T_1. These time constants are often for convenience expressed as the rates $R_1 = 1/T_1$ and $R_2 = 1/T_2$.

For the NMR of small molecules in liquids, the transverse relaxation time constant T_2 is typically in the same order of magnitude as T_1, i.e. several seconds. Whereas for solids or large molecules in liquids, T_2 may be as short as milliseconds. [1, p. 35]

2.1.4 Chemical shift

The previously mentioned perturbations of $\boldsymbol{B}_0$ can originate in the electron configuration in outer atomic shells and in chemical bonds surrounding the spin, as the electrons generate small magnetic fields that add to or subtract from $\boldsymbol{B}_0$ [1, Ch. 3.7]. Hence the magnetic field experienced by a spin, and therefore also its resonance frequency, is dependent on the location of the spin in the molecule, and on details of the electronic structure. The shift in resonance frequency of the spins is called chemical shift. The field-independent expression for the chemical shift is

$$\delta(\text{ppm}) = \frac{\omega^0 - \omega^0_{\text{ref}}}{\omega^0_{\text{ref}}} \cdot 10^6, \tag{2.17}$$

where ω^0 is the resonance frequency of a particular nucleus and ω^0_{ref} is the resonance frequency of the same isotope in a reference compound exposed to the same static field. If the static field increases both ω^0 and ω^0_{ref} increases in the same proportion, giving a field independent δ [1, Ch. 3.7].

2.1.5 Detection of NMR signal

When spins subject to relaxation processes begin to realign with the static field, the changing net transverse magnetization induces an electric current in a receiver coil surrounding the spins, as seen in Figure 2.1. This signal is detected, and can be used to extract information from the sample under consideration.

The signal obtained varies with which pulse sequences that have been applied, where most of them are beyond the scope of this thesis. Considering a system of spins that has been excited by an RF pulse, and then allowed to freely realign with the external static field, a free induction decay (FID) is gained. This is what happens in Figure 2.1. The signal strength and appearance of this FID depends on both the number of excited spins in the system, and their chemical shifts. By Fourier transforming the FID the individual components of the signal become visible, separated by their different chemical shifts [1, p. 96].

A further description of Fourier transforms will not be given in this thesis.

2.1.6 Radiation damping

When considering molecules dissolved in aqueous buffers consisting of 90-95% H_2O (and the rest being D_2O) the concentration of protons in the solvent can be thousands of times higher than those in the solute. Standard NMR methods overlook the possibility that individual spins can influence the bulk nuclear magnetization of the whole sample, predominantly those of the water spins [16]. Radiation damping is an intrinsic physical phenomenon in all NMR experiments, but is normally observed in experiments with high proton concentration, like aqueous solutions, at high fields. It is a sort of feedback that gives rise to a broadening effect seen in NMR signals [16]:

Consider an ensemble of spins aligned with an external magnetic field $\boldsymbol{B}_0 = B_0\hat{\boldsymbol{z}}$ in the laboratory frame of reference, making the net magnetization directed in the z-direction at thermal equilibrium. An applied RF pulse pushes the net magnetization away from the thermal equilibrium, and makes all or parts of it precess in the transverse plane. The precessing transverse magnetization of the water protons will induce an electromagnetic field in the receiver coil. This creates an oscillating current which generates a transverse magnetic field at the same frequency. The induced field affects the solvent spins, and rotates them towards their thermal equilibrium in z-direction [16]. This happens before other relaxation mechanisms can take effect, and gives a discrepancy between the theoretical predictions of relaxation times and experimental observation [17].

It is inevitable that RD will affect the spectrum of molecules in solvents containing a high concentration of protons, and in experiments concerning high static field strengths this effect should be taken into consideration. The increased sensitivity of high field NMR spectrometers over the past decades allows the aquisition of NMR data for samples at lower concentrations, but also makes it possible to observe RD effects which were previously considered negligible [16].

2.2 Introduction to chemical exchange saturation transfer

Chemical exchange saturation transfer (CEST) is a novel NMR technique intended to produce image contrast. CEST imaging detects dilute labile protons indirectly, via changes in the bulk water signal following a selective saturation of exchangeable protons. This offers a substantial sensitivity enhancement, and has sparked numerous biomedical applications [5]. This section will describe the mechanisms underlying CEST, and is if not stated otherwise based on reference [2].

Consider spins aligned with an external magnetic field $\boldsymbol{B}_0$ in a sample of different compounds or solutes. As the protons in different molecules, and in different sites in molecules, experience different chemical shifts, they will also precess with different resonance frequencies ω. For simplicity, a model where two pools that exchange protons is considered, but the theory is extendable to multiple pools. The first pool (s) is a small pool for water-exchangeable solute protons. These are called CEST agents, and can for example be amide protons of mobile cellular proteins and peptides of mM concentration in tissue [14]. The second and much larger pool (w) reflects the bulk water protons. This is illustrated with the organic acid creatine as solute in Figure 2.3. In particular, protons connected to a solute (pool s) will resonate at a frequency that is different from the bulk water protons (pool w). To employ CEST, these solute protons also have to be exchangeable.

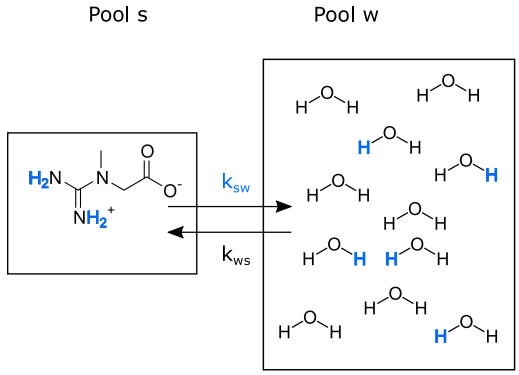

Figure 2.3: A small solute pool (s) consisting of creatine, and a much larger water pool w. The protons marked blue in pool s are saturated by an RF pulse, and the saturation of pool (w) increases due to chemical exchange with the saturated protons in pool s. The forward exchange rate k_{sw} is assumed to be much larger than the back exchange rate k_{ws}.

During a CEST experiment the solute protons are selectively saturated using a weak RF field, which can either be a continuous wave or a pulse train [14]. Saturation here refers to equilibrating the populations of the proton energy levels α and β, meaning that the net magnetization from the protons with resonance frequency corresponding to the frequency of the RF pulse decreases. Often the solute protons are of low concentration, and this has a limited effect on the signal obtainable from the sample. By exchanging with the bulk water, this effect is enhanced:

Being exchangeable, the saturated protons in the solute have the ability to switch places with the unsaturated protons in the bulk water. This happens with an exchange

rate k_{sw}, and as time passes the water signal also becomes increasingly saturated. As pool w is much larger than pool s, one can assume that each exchanging saturated solute proton is replaced by a non-saturated water proton, which is then again saturated.

If the solute protons have a sufficiently fast exchange rate (residence time in millisecond range) and the saturation time t_{sat} is sufficiently long (second range), the saturation effect eventually becomes visible on the water signal with prolonged irradiation. There will also be a back exchange k_{ws} of saturated protons from pool w to s, and the CEST effects build up towards a steady-state with a time constant in the order of T_1, where the steady-state signal is reached after long saturation periods ($\sim 5 \cdot T_1$) [18]. This effect allows the presence of low-concentration solutes to be imaged indirectly:

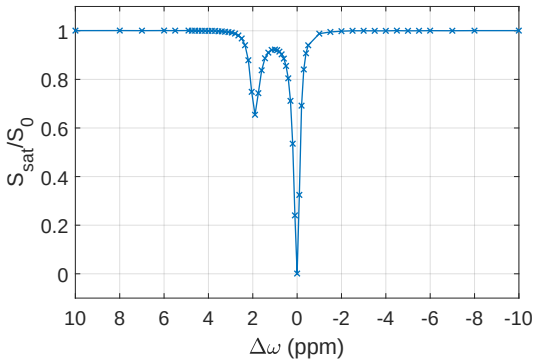

Figure 2.4: CEST spectrum of a sample of 47.5 mM creatine acquired at 298.1 K with a saturation field strength of 1 μT. The dip at 0 ppm is a result of the direct saturation (DS) of water protons. There is another dip about 2 ppm, as a result of CEST of guanidinium protons in creatine. The density of offset frequencies is largest between 1 and 5 ppm, as that is where the CEST effect is expected to be.

By varying the frequency of the saturation pulse, different protons (or no protons) will be saturated. Plotting the signal S_{sat} normalized with the unsaturated signal S_0 as a function of saturation frequencies then indicates for which frequencies there is a CEST effect in the sample, and thus gives information about the solutes in it. This is called a CEST spectrum, or Z-spectrum. A CEST spectrum obtained on a Bruker Avance 600 MHz NMR spectrometer for a sample of 47.5 mM creatine with a saturation field strength of 1 μT can be seen in Figure 2.4. Pre-saturating at the resonance frequency of water, called direct saturation (DS), makes most of the signal disappear, giving a characteristic dip in the centre of the spectrum (see Figure 2.4). This is why the resonance frequency of water ω_0 in these spectra is set to 0 ppm, and the saturation frequencies ω are presented as offsets from water frequency: $\Delta\omega = \omega - \omega_0$. The CEST effects of amide, imino, amine and

hydroxyl groups are expected to be found at positive offsets, defined downfield, in a range of 0 to 7 ppm above the water frequency [2], where the most interesting range is 1 to 5 ppm above the water frequency [14].

2.2.1 The CEST pulse sequence

An example of a CEST pulse sequence is found in Figure 2.5. The sequence initiates with a system in thermal equilibrium, meaning that the net nuclear magnetization is aligned with the external magnetic field $\boldsymbol{B}_0$ in the spectrometer. A saturation pulse of strength B_1 is then applied for a certain offset frequency ω. The saturation time t_{sat} is typically in the order of seconds. After saturation a gradient is applied to destroy potential magnetization in the plane transverse to $\boldsymbol{B}_0$. This is followed by a read pulse; an RF pulse that rotates the net magnetization away from thermal equilibrium. The system's subsequent realigning with $\boldsymbol{B}_0$ then gives rise to a FID, which signal corresponds to the net magnetization of the protons in water. This FID will have a decreasing signal intensity as the total saturation in the sample increases.

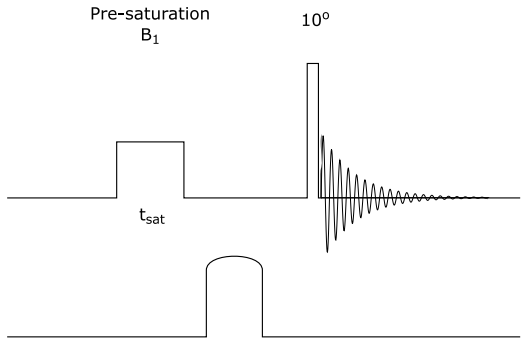

Figure 2.5: Example of a CEST pulse sequence. To begin with, the system is placed in an external magnetic field, and is assumed to be in thermal equilibrium. Then the system is saturated with a magnetic field strength B_1 at a specific offset frequency ω for a time t_{sat}. A gradient is applied to destroy potential magnetization in the transverse plane, as cause of the the saturation, and a read pulse is applied to create a FID. The magnitude of the read pulse can vary. Here 10° is applied, to avoid a FID signal strong enough to interfere with the signal acquisition through e.g. radiation damping.

2.2.2 Effects of CEST on NMR spectral line shapes

The chemical exchange processes can occur over a very wide range of time-scales, from nanoseconds to many seconds or longer, or from larmor to relaxation time-scale [1, Ch. 19.2]:

- *Larmor time-scale.* The characteristic Larmor time-scale is given by τ^0, where $|\omega^0\tau^0| \sim 1$, with ω^0 being the Larmor frequency. Processes on this time-scale are responsible for the longitudinal relaxation.

- *Spectral time-scale.* Consider a spin system containing two spins with chemical shift frequencies Ω_1^0 and Ω_2^0. Then the spectral time-scale τ_{spec} is given by $|(\Omega_1^0 - \Omega_2^0)\tau_{\text{spec}}| \sim 1$. It represents the inverse width of the NMR spectrum measured in frequency units. Processes on this time-scale strongly affects the NMR line shapes. In random processes, such as chemical exchange, the spectra typically broaden.

- *Relaxation time-scale.* Usually in the order of seconds, from the value of the longitudinal relaxation time constant T_1. Processes on this time-scale do not significantly affect the NMR line shapes, but may still be detected by NMR through their influence on the dynamics of spin populations.

Considering chemical exchange between a water pool w and a solute pool s, the forward exchange k_{sw} is assumed to be much larger than the back exchange k_{ws}. This gives an asymmetric two-site exchange which can affect the NMR spectral line shape, if the exchange rate is in a suitable time-scale. The time-scale, and thus the effect of the exchange process on the NMR spectrum, depends on the difference in the chemical shift frequencies $\omega_\Delta = \omega_{\text{s}}^0 - \omega_{\text{w}}^0$ of the two sites, the population of each pool and the exchange rate k_{sw} [1, Ch. 19.5] [19].

NMR spectra affected by chemical exchange are segregated into three exchange regimes denoted slow ($k_{\text{sw}} \ll \omega_\Delta$), intermediate ($k_{\text{sw}} \approx \omega_\Delta$) and fast ($k_{\text{sw}} \gg \omega_\Delta$). In the slow exchange regime there is not significant s $\leftrightarrow$ w interconversion during the frequency detection period of the NMR experiment. In this limit both states s and w are observed in the ^{1}H-NMR spectra reflecting their distinct chemical shifts, intensities and linewidths, where the intensity of each peak directly reports on the population of that species. In the intermediate exchange regime an increasing exchange rate gives significant s $\leftrightarrow$ w interconversion during the detection period, causing an exchange broadened linewidth that eventually leads to the two peaks merging into one signal [19]. This is because the s $\leftrightarrow$ w interconversion causes an averaging during the detection period of the NMR experiment. Regarding CEST experiments the CEST contrast can especially in

the intermediate exchange regime become imperceptible. Also at the fast exchange limit only one signal is observed from the two pools in the NMR spectra, but with a linewidth decreasing with increasing k_{sw} [19]. Its position is given by the mean of the two chemical shifts, weighted by the equilibrium concentrations of the two species [1, Ch. 19.5]:

$$\omega_{peak} = \frac{[s]_{eq}\omega_s^0 + [w]_{eq}\omega_w^0}{[s]_{eq} + [w]_{eq}} = \frac{\omega_s^0 + K\omega_w^0}{1 + K}, \tag{2.18}$$

where $[s]_{eq}$ and $[w]_{eq}$ are the equilibrium concentrations of the two species and $K = k_{sw}/k_{ws}$ is the equilibrium constant of the exchange, equal to the ratio of species concentrations when the reaction is in equilibrium[1].

2.3 The spoiler recovery CEST approach

To create a CEST spectrum a CEST sequence has to be run for a range of offset frequencies. To ensure that the system returns to its thermal equilibrium state between each offset scan, a wait time (TR) of $5 \cdot T_1$ is applied between each scan. For aqueous solutions at high fields the longitudinal relaxation times become very long, giving TR up to 30 seconds. With 60 offset frequencies the TR alone contributes to 30 minutes of the total scan time. In order to make the CEST experiment less time consuming, a spoiler recovery pulse sequence (SR) can be applied [11]:

With the SR sequence a long TR is no longer required. It produces a situation where the net nuclear magnetic moment of the nuclear spins is zero. Instead of waiting for the system to fully re-equilibrate after each CEST sequence, the magnetization in the sample is destroyed after each CEST sequence. The system is reset, and the state of the nuclear spins after the SR sequence is comparable to the state without any external magnetic field.

The SR sequence is initiated with a 90° RF-pulse that flips the magnetization initially aligned with the z-axis into the transverse (x-y) plane. This pulse is followed by a relatively long gradient pulse of gradient strength GS1, which dephases the nuclear spin vectors in the x-y-plane. The idea of SR is to spoil the magnetization uniformly in space, not just in the transverse plane. To achieve this, another 90° RF-pulse is applied. This is followed by a new gradient pulse of opposite polarity and gradient strength GS2 to the first one.

When more than two RF-pulses are applied in a pulse sequence, such as the spoiler recovery sequence, several echoes may be generated. These should be suppressed, in order to not interfere with the signal desired to be measured. A way to do this is to employ the concept of coherence transfer pathways[2] to construct a sequence that avoids gradient

[1] This neglects the distinction between the concentration and kinetic activity of a substance.

[2] The coherence transfer pathway is given by

echoes. The basic requirement for avoiding gradient echoes after application of the second gradient pulse in the spoiler recovery sequence is the relation

$$\gamma \mathrm{GS1} \int_0^{\delta_{\mathrm{GS1}}} z_1(t)\mathrm{d}t \neq \gamma \mathrm{GS2} \int_0^{\delta_{\mathrm{GS2}}} z_2(t)\mathrm{d}t, \tag{2.20}$$

where δ_{GS1} and δ_{GS2} are the durations of the spoiler gradient pulses, $z_{1,2}(t)$ are the molecular positions at the time of the two gradient pulses, and γ is the gyromagnetic ratio. By adjusting the spoiler gradient strengths GS1, GS2 and their durations, the coherent signal following the two RF-pulses from different locations along the length of the sample can be crushed. This follows from Eq. 2.20, where proper settings of the spoiler gradients and their durations produce location dependent phases that varies from 0 to for example 40π. The sum of the contributions will then give a net 0 magnetization. Consequently, any coherence transfer pathway arising from the two first 90° RF-pulses does not contribute to any significant signal after application of the third RF-pulse, the read pulse [11, Ch. 1.7].

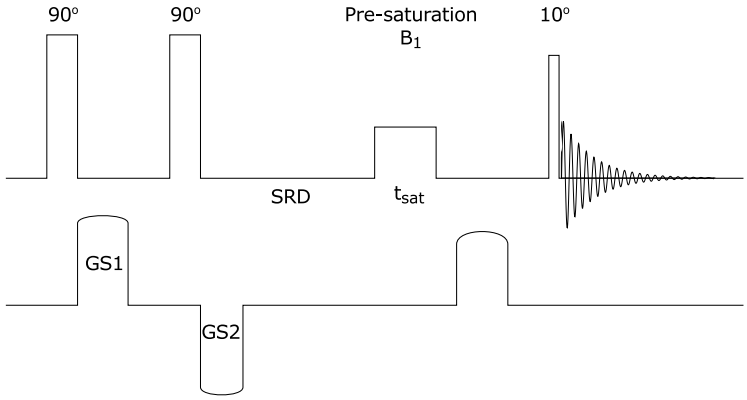

Figure 2.6: The proposed SR-CEST pulse sequence. First the net magnetization is destroyed by two 90°-pulses and corresponding bipolar gradients GS1 and GS2. During a spoiler recovery delay (SRD) the magnetization present at thermal equilibrium is partially regained, and a regular CEST sequence follows.

Immediately after the gradient spoiling, the net nuclear magnetization will begin to realign with the external magnetic field. This is a result of T_1 relaxation processes, and

$$\phi = \sum_{j=1}^{n} \Delta p_j \phi_j, \tag{2.19}$$

where ϕ is the accumulated phase change determined by the product of the change in coherence order Δp_j and the phase ϕ_j of the RF-pulse number j. n equals the number of RF-pulses applied in the experiment [11, Ch. 1.7].

follows the equation

$$M(\text{SRD}) = M_0(1 - e^{\frac{\text{SRD}}{T_1}}), \tag{2.21}$$

where M is the time dependent net magnetization of the nuclear spins, M_0 is the magnetization at thermal equilibrium, T_1 is the longitudinal relaxation time of the system and SRD is the spoiler recovery delay time; the time passed between the gradient spoiling and the pre-saturation [11]. This signifies that after an SRD equal to T_1, 63% of the signal present at thermal equilibrium is already regained. The CEST sequence does not require that 100% of the signal is regained. On the contrary, a reoccurring problem in CEST experiments on aqueous solutions is that the signal generated in the FID is too strong, creating problems such as radiation damping (see Section 2.1.6). By applying the CEST sequence after an SRD of T_1 the delay time between scans is reduced by 80%, compared to a regular CEST sequence with TR = $5 \cdot T_1$. A further reduction of SRD will reduce experimental time even more, in addition to a reduction in signal obtained from the FIDs. The pulse sequence proposed in this thesis, the SR-CEST, is conducting this, and can be seen in Figure 2.6.

It is worth mentioning that the net magnetization of the nuclear spins will continue to re-equilibrate during t_{sat} (usually in the order of seconds), giving a larger increase in magnetization than what is portrayed in Eq. 2.21.

2.4 CEST spectrum analysis

When it comes to analyzing the CEST spectra, the direct saturation (DS) of water at 0 ppm may interfere with the detection of CEST effects. Magnetization transfer ratio asymmetry (MTR_{asym}) analysis is conventionally used to suppress the DS effect. It employs the symmetry of the DS, by subtracting the signal intensity ratio upfield from the one downfield:

$$MTR_{\text{asym}} = MTR(\Delta\omega) - MTR(-\Delta\omega) = \frac{S_{\text{sat}}(-\Delta\omega)}{S_0} - \frac{S_{\text{sat}}(\Delta\omega)}{S_0}, \tag{2.22}$$

with

$$MTR = 1 - \frac{S_{\text{sat}}}{S_0}. \tag{2.23}$$

This approach may work well as a first approximation, but it assumes that the only effect seen upfield is the DS of water. This is often wrong, especially considering in-vivo studies [2], mainly due to the nuclear Overhauser effects (NOE) and semi-solid

macromolecular magnetization transfer (MT):

- **The nuclear Overhauser effect (NOE)** is a type of cross-relaxation that can happen between all magnetic nuclei in spatial proximity [2], and an effect from dipoles transfering polarization between one-another. If a weak RF field is applied at the resonance frequency of one of the spins in a molecule for a sufficiently long time, the longitudinal magnetization of non-irradiated spins in spatial proximity can in some cases be enhanced [1, p. 566]. Regarding CEST experiments, the NOE thus provides of another magnetization transfer pathway that may contribute to the signals displayed in the CEST spectra. In short, protons saturated in a CEST experiment can transfer their polarization through dipol-dipol-coupling with nearby water. This results in dips in the CEST spectra, although not originating from chemical exchange. The chemical exchange and dipolar cross-relaxation pathways are active together in most magnetization transfer experiments, and difficult to separate completely from one-another [2]. In comparison to the CEST effect the NOE occurs upfield from water, breaking the asymmetry around the DS of water in the CEST spectra.

- **The semi-solid macromolecular magnetization transfer (MT)** is another magnetization transfer pathway, and a non-selective effect scattered across the CEST spectrum with broad resonance linewidths [18]. It results from the saturation of protons bound to the surface of macromolecules and protons in water molecules restricted by a semi-solid matrix, which can be surfaces of proteins, cell membranes and structure elements like collagen fibers in cartilage, bone and skin. T_2 times in the order of μs make MT appear as strongly broadened peaks in the CEST spectra, corresponding to strongly broadened resonances. Macromolecular MT is mainly governed by the proton transfer ratio from the macromolecular pool to the water pool of about 40 s^{-1} and the concentration of the pool of protons with restricted mobility relative to that of the free pool [18]. The macromolecular MT effect is the foundation of magnetization transfer contrast (MTC) imaging, which is used clinically. In conventional MTC imaging experiments the two pools are treated as having identical chemical shift, and are contrary to CEST experiments only distinguished by relaxation parameters [14]. The exchange rate for CEST experiments is also much larger than the average exchange rate for MTC, which opens up a new range of labeling approaches that cannot be applied to MTC [2].

With these effects present, the conventional asymmetry analysis MTR_{asym} will measure a mixed contribution. Resolving individual contributions then becomes necessary [9].

This can be done by curve fitting the CEST spectra to a set of modified Bloch equations corresponding to the physical system, as described in the following section.

2.4.1 Bloch-McConnell equations for two-pool exchange

The change both in transversal and longitudinal magnetization of a solute pool s and a water pool w can be described by the Bloch equations introduced in Section 2.1.3, with additional terms for chemical exchange and an applied RF saturation field $\boldsymbol{B}_1$ [13]. These are called the Bloch-McConnell (BM) equations.

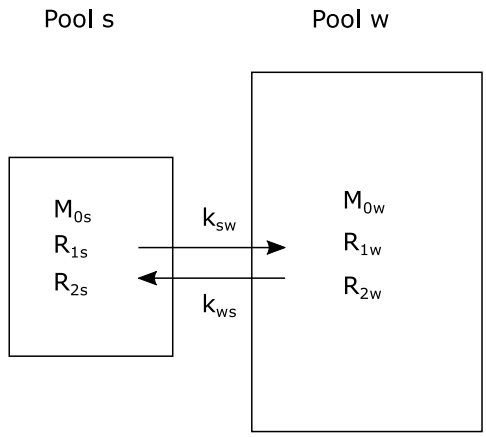

Figure 2.7: Schematic model of two-pool proton exchange, where pool s reflects the dilute exchangeable solute protons, and pool w reflects bulk water protons. R_{1s}, R_{2s}, and M_{0s} are respectively the longitudinal relaxation rate, transverse relaxation rate and equilibrium magnetization for pools s. k_{sw} is the exchange rate of protons from pool s to pool w. Exchanging s and w gives the corresponding parameters for pool w.

Consider a two-pool system with thermal equilibrium magnetizations $\boldsymbol{M}_{0s}$ and $\boldsymbol{M}_{0w}$ and forward exchange rate k_{sw} in a static magnetic field $\boldsymbol{B}_0 = (0, 0, B_0)$ (see Figure 2.7), where the subscripts s and w denotes pool s and pool w. In the rotating frame of reference, defined by the frequency of the oscillating field $\boldsymbol{B}_1(t) = \gamma\boldsymbol{\omega}_1$, the BM equations then read [18]

$$\frac{\mathrm{d}}{\mathrm{d}t}\boldsymbol{M} = A \cdot \boldsymbol{M} + \boldsymbol{C}, \tag{2.24}$$

with A being a 6-by-6 matrix describing the physical system, and the six-dimensional magnetization vector

$$\boldsymbol{M} = \begin{pmatrix} M_{\mathrm{xw}} \\ M_{\mathrm{xs}} \\ M_{\mathrm{yw}} \\ M_{\mathrm{ys}} \\ M_{\mathrm{zw}} \\ M_{\mathrm{zs}} \end{pmatrix}.$$

The constant vector $\boldsymbol{C}$ is given by

$$\boldsymbol{C} = \begin{pmatrix} 0 \\ 0 \\ 0 \\ 0 \\ R_{1\mathrm{w}} M_{0\mathrm{w}} \\ R_{1\mathrm{s}} M_{0\mathrm{s}} \end{pmatrix},$$

where $R_{1\mathrm{s}}$ and $R_{1\mathrm{w}}$ are the longitudinal relaxation rates for the pools. The matrix A can be expressed by [18]

$$A = \begin{pmatrix} -R_{2\mathrm{w}} - f_{\mathrm{b}} k_{\mathrm{sw}} & k_{\mathrm{sw}} & -(\omega_{0\mathrm{w}} - \omega) & 0 & 0 & 0 \\ f_{\mathrm{b}} k_{\mathrm{sw}} & -R_{2\mathrm{s}} - k_{\mathrm{sw}} & 0 & -(\omega_{0\mathrm{s}} - \omega) & 0 & 0 \\ \omega_{0\mathrm{w}} - \omega & 0 & -R_{2\mathrm{w}} - f_{\mathrm{b}} k_{\mathrm{sw}} & k_{\mathrm{sw}} & -\omega_1 & 0 \\ 0 & \omega_{0\mathrm{s}} - \omega & f_{\mathrm{b}} k_{\mathrm{sw}} & -R_{2\mathrm{s}} - k_{\mathrm{sw}} & 0 & -\omega_1 \\ 0 & 0 & \omega_1 & 0 & -R_{1\mathrm{w}} - f_{\mathrm{b}} k_{\mathrm{sw}} & k_{\mathrm{sw}} \\ 0 & 0 & 0 & \omega_1 & f_{\mathrm{b}} k_{\mathrm{sw}} & R_{1\mathrm{s}} - k_{\mathrm{sw}} \end{pmatrix},$$

where the proton fraction f_{b} is given by

$$f_{\mathrm{b}} = \frac{M_{0\mathrm{s}}}{M_{0\mathrm{w}}} = \frac{n_{\mathrm{s}}[\mathrm{s}]}{n_{\mathrm{w}}[\mathrm{w}]}, \tag{2.25}$$

where [s] and [w] are the concentrations of pool s and w, respectively, and n_{s} and n_{w} are the numbers of exchanging protons per molecule for the respective proton pools.

ω is the current offset frequency, and hence A changes for each offset scan. A strong dependence of T_{1w} of the CEST effect is explained by the fact that the signal reduction because of saturation transfer is counterbalanced with signal recovery from longitudinal relaxation of the bulk water signal. Likewise, T_{2w} comes into play through the concomitant RF spillover effect [5].

2.4.2 Numerical solution of the BM equations

It is at the least challenging to solve Eq. 2.24 analytically without making several assumptions. Zhou *et al.* [14] obtained an expression for the amide proton transfer ratio by assuming that pool s is saturated instantly, and assuming that the RF field only affects pool s. The assumption of the system being at a saturation steady state also often have to be made in analytic solutions. This, as discussed previously, does not happen before $\sim 5 \cdot T_1$, corresponding to very time consuming CEST experiments.

The advantage of a numerical solution of the BM equations is that it does not require any of these assumptions. The BM equations are first-order ordinary differential equations with an inhomogeneous term $\boldsymbol{C}$, and the formal solution is [18]

$$\boldsymbol{M} = (\boldsymbol{M}_0 + A^{-1}\boldsymbol{C})\exp\{A \cdot t_{sat}\} - A^{-1}\boldsymbol{C}. \tag{2.26}$$

A is not a diagonal matrix, and must be diagonalised in order to take the exponential of it.

$$A = XDX^{-1}, \tag{2.27}$$

where X is a matrix whose columns are given by the eigenvectors of A, X^{-1} is the inverse of X and D is a diagonal matrix with diagonal elements equal to the eigenvalues of A [1, p. 656]. This gives

$$\exp\{A \cdot t_{sat}\} = X\exp\{D \cdot t_{sat}\}X^{-1}. \tag{2.28}$$

Eq. 2.26 can be used to simulate the system under consideration, both for the CEST and spoiler recovery CEST (SR-CEST) experiments. The simulation has to be run for each offset frequency ω, beginning completely off-resonance and moving through the spectrum. After running through all ω a simulated CEST spectrum can be created. This is employed in a numerical fitting of the CEST spectra, where the goal is to find the simulated spectrum that gives the best fit to an experimentally obtained spectrum. An example of this is seen in Figure 2.8, with a spectrum obtained with regular CEST for a sample of 47.5 mM

creatine with a saturation field strength of $B_1 = 1$ μT. The difference between the fitted normalized spectrum and the experimental spectrum indicates how good the fit is, and will be used further in this work.

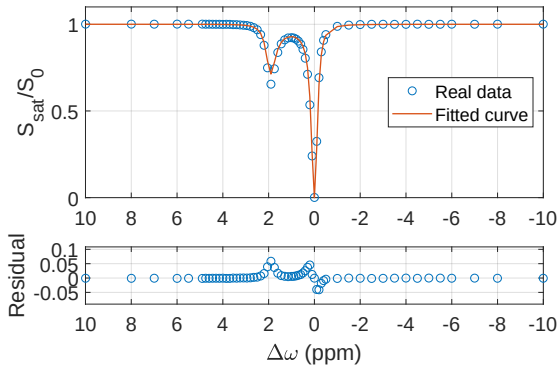

Figure 2.8: CEST spectrum of a sample of 47.5 mM creatine at 298.1 K acquired with a saturation field strength B_1 of 1 μT and corresponding numerically fitted curve. The fitted curve represents the CEST spectrum based upon fitting the experimental data to the numerical soultion of the BM equations, and the residuals are the differences between the fitted and the experimental spectrum.

2.4.2.1 Regular CEST

The numerical solution differs between regular CEST and SR-CEST. In regular CEST the simulation begins with constructing the A-matrix for each ω. Initially, there is only magnetization in the z-direction, giving

$$\boldsymbol{M}_0 = \begin{pmatrix} 0 \\ 0 \\ 0 \\ 0 \\ M_{\mathrm{zw}} \\ M_{\mathrm{zs}} \end{pmatrix}.$$

In this work the saturation time t_{sat} have been 5 seconds, and Eq. 2.26 becomes

$$\boldsymbol{M} = (\boldsymbol{M}_0 + A^{-1}\boldsymbol{C})\exp\{A \cdot 5\} - A^{-1}\boldsymbol{C}. \tag{2.29}$$

After saturation, a gradient is applied to spoil magnetization in x- and y-direction. In Matlab this is simulated by setting $\boldsymbol{M}(1:4) = 0$. $\boldsymbol{M}(5)$ is then the simulated magnetization of the water pool in z-direction after saturation for a certain offset frequency ω, which is what gives a single point in the CEST spectrum. Subsequently, the relaxation of the system is simulated. This is done by first removing the effect of the RF saturation pulse in A:

$$A' = \begin{pmatrix} -R_{2w} - f_b k_{sw} & k_{sw} & -(\omega_{0w} - \omega) & 0 & 0 & 0 \\ f_b k_{sw} & -R_{2s} - k_{sw} & 0 & -(\omega_{0s} - \omega) & 0 & 0 \\ \omega_{0w} - \omega & 0 & -R_{2w} - f_b k_{sw} & k_{sw} & 0 & 0 \\ 0 & \omega_{0s} - \omega & f_b k_{sw} & -R_{2s} - k_{sw} & 0 & 0 \\ 0 & 0 & 0 & 0 & -R_{1w} - f_b k_{sw} & k_{sw} \\ 0 & 0 & 0 & 0 & f_b k_{sw} & R_{1s} - k_{sw} \end{pmatrix},$$

that is, to set $\omega_1 = 0$. Eq. 2.26 then becomes

$$\boldsymbol{M'} = (\boldsymbol{M} + A'^{-1}\boldsymbol{C})\exp\{A' \cdot \mathrm{TR}\} - A'^{-1}\boldsymbol{C}, \tag{2.30}$$

with TR being the repetition time before next offset frequency is applied in the CEST sequence. This is often set to $\sim 5 \cdot T_1$. With sufficient TR $\boldsymbol{M'}$ approaches and becomes equal to $\boldsymbol{M}_0$. This is important, as $\boldsymbol{M'}$ is what is used as $\boldsymbol{M}_0$ for the next offset frequency ω.

2.4.2.2 Spoiler recovery CEST

The initial conditions for SR-CEST differs from the regular one. After the two spoiling gradients, a net magnetization of 0 in all directions is assumed. In this case, the initial magnetization vector $\boldsymbol{M}_0$ is

$$\boldsymbol{M}_0 = \begin{pmatrix} 0 \\ 0 \\ 0 \\ 0 \\ 0 \\ 0 \end{pmatrix}.$$

After spoiling of the magnetization the system begins to return to thermal equilibrium, gaining magnetization in the z-direction. This can also be simulated by Eq. 2.26, with

$$A' = \begin{pmatrix} -R_{2w} - f_b k_{sw} & k_{sw} & -(\omega_{0w} - \omega) & 0 & 0 & 0 \\ f_b k_{sw} & -R_{2s} - k_{sw} & 0 & -(\omega_{0s} - \omega) & 0 & 0 \\ \omega_{0w} - \omega & 0 & -R_{2w} - f_b k_{sw} & k_{sw} & 0 & 0 \\ 0 & \omega_{0s} - \omega & f_b k_{sw} & -R_{2s} - k_{sw} & 0 & 0 \\ 0 & 0 & 0 & 0 & -R_{1w} - f_b k_{sw} & k_{sw} \\ 0 & 0 & 0 & 0 & f_b k_{sw} & R_{1s} - k_{sw} \end{pmatrix},$$

that is, again $\omega_1 = 0$. To gain the nuclear magnetization in the system after a spoiler recovery delay (SRD) Eq. 2.26 becomes

$$\boldsymbol{M} = (\boldsymbol{M}_0 + A'^{-1}\boldsymbol{C})\exp\{A' \cdot \mathrm{SRD}\} - A'^{-1}\boldsymbol{C}, \tag{2.31}$$

with SRD being the time between gradient spoiling and pre-saturation. To simulate the saturation A' is reconstructed to A, and to again contain ω_1. Eq. 2.26 is then

$$\boldsymbol{M'} = (\boldsymbol{M} + A^{-1}\boldsymbol{C})\exp\{A \cdot 5\} - A^{-1}\boldsymbol{C}. \tag{2.32}$$

As before $\boldsymbol{M'}(1:4)$ is set to 0, to simulate the spoiling of the magnetization in the transverse plane, and $\boldsymbol{M'}(5)$ gives the signal strength that is used in the simulated CEST spectrum. For SR-CEST, the recovery is excessive to simulate, as the net magnetization is destroyed again before next ω_1 is applied.

2.4.2.3 Multiple pools

It is straightforward to extend the numerical solution to account for three or more pools. By assigning pools to the NOE and MT effects, also these can be taken account for in the numerical BM fitting.

Chapter 3

Methods

Several saturation recovery and CEST experiments were run on a Bruker Avance III 600 MHz Ultrashielded Plus (Bruker BiosSpin GmbH, Rheinstetten, Germany) spectrometer equipped with a 5 mm QCI Cryoprobe. The sample tubes used were Bruker SampleJet NMR tubes with a diameter of 5.00 mm.

3.1 Samples

Experiments were run for several samples of different CEST agents in a buffer containing phosphate. The samples contained 10% D_2O to provide a lock signal for the NMR instrument, and are listed in Table 3.1.

Sample	Metabolite concentration (mM)	Phosphate concentration (mM)
Creatine	10	37.5
Glutamic acid	10	37.5
Myo-inositol	10	37.5
Creatine + glutamic acid	10 + 10	37.5
Creatine	47.5	37.5
Creatine	45	0
Creatine	45	10
Creatine	45	37.5

Table 3.1: Concentration of CEST agents in each sample. The samples were aqueous solutions of the CEST agents, mixed with a buffer containing phosphate of varying concentration. One sample had no buffer. All samples contained 10% D_2O, including the buffer-free sample.

The exact procedure used to make the samples and phosphate buffer is found in Appendix A.1. Most experiments were run at 310 K to assimilate an *in vivo* setting. The exception is the sample of 47.5 mM creatine, which was experimented on at 298.1 K.

3.2 CEST experiment

In the regular CEST experiments the samples were first saturated with a saturation field strength B_1 at a certain offset frequency ω. This pre-saturation was on for 5 seconds, with 61 different offset frequencies ranging from -10 to 10 ppm and two additional offsets at -500 and +500 ppm. All offset frequencies used are listed in Appendix A.2. The density of offset frequencies was largest downfield, as that is where the CEST effects are expected to be. After saturation an excitation pulse with a flip angle of 10° was applied, and the free induction decay (FID) was acquired. A figure displaying the CEST sequence graphically is found in Figure 2.5. Between each scan a relaxation recovery delay (TR) of $\sim 5 \cdot T_1$ has been applied, giving TR in the order of 20 s.

After acquiring the FID signal for all offset frequencies, each FID was 1D Fourier transformed in Bruker's software package TopSpin 4.0.6. A data set consisting of all the transformed FIDs was further processed in Matlab, where the integral over the water peak in the center of each transformed FID was calculated. The integration borders were -0.8 and 0.8 ppm, which were expected to enclose approximately all of the water signal. The integrated water signal was then plotted as a function of offset frequencies, giving a CEST spectrum as described in Section 2.2. The Matlab script used to generate the CEST spectra was provided by Vitaliy Khlebnikov at University Medical Center Utrecht, modified to fit the experimental conditions in this work.

3.3 SR-CEST experiment

For the spoiler recovery CEST, two 90° pulses were applied before the identical CEST sequence, eached followed by a sine-shaped spoiling gradient as seen in Figure 2.6. The first gradient was on for 1 ms with gradient power 30 G/cm, and the second gradient was one for 2 ms with a gradient power of −5 G/cm. The delay between the 90° pulses was 5 ms, and the TR between each subsequent offset scan was set to 30 ms. This left SRD and t_{sat} the most time consuming parts of the experiments, in addition to a signal acquisition time of 2.73 s. The process of generating a CEST spectrum was identical for SR-CEST as for regular CEST.

3.4 T1 relaxation measurements

The water T_1 relaxation times in the samples had to be measured in order to do the further numerical analysis. Due to a strong signal from water protons, an inversion recovery sequence could not be used to find T_1. Instead, a saturation recovery sequence was used: The samples were placed in the spectrometer, in the external, constant field $\boldsymbol{B}_0$. The water signal was then saturated for 5 seconds, making the net magnetization disappear. After saturation, the magnetization will gradually recover and move towards realignment with $\boldsymbol{B}_0$. By using an excitation pulse with flip angle of 10° after a delay ΔT, a FID can be measured. The signal strength of the FID indicates how much of the magnetization is recovered, and by varying ΔT different signal strengths will be measured. The experiment was conducted for 13 different ΔT: 4 µs, 30 ms, 0.1 s, 0.2 s, 0.5 s, 1 s, 2 s, 4 s, 8 s, 12 s, 16 s and 24 s. To find the signal originating from the water protons, the FID signals were 1D Fourier transformed in Bruker's software package TopSpin 4.0.6, and the integral over the water peak was calculated in Matlab. With the resonance frequency of water at 0 ppm, the integral was taken from -0.8 to 0.8 ppm. The characteristic relaxation time T_1 was then found by curve fitting the mono-exponential behaviour of the relation between the acquired water proton signal and delay time ΔT. The Matlab script conducting this was also provided by Vitaliy Khlebnikov at University Medical Center Utrecht.

3.5 Numerical analysis

For the CEST spectra acquired for the simple samples in this work, where no effects originating in NOE or MT were expected to be present, an MTR_{asym} analysis as discussed in Section 2.4 could have been applied. This is not the case for more complex samples, and for better transferability to more complex experiments, a curve fitting has been applied instead. By numerically solving the Bloch-McConnell equation from Section 2.4.1 and finding the coefficients giving the least square error in comparison to the experimental spectra, several physical quantities in the samples can be estimated. It is straightforward to extend the solution for three or more pools, which was done for the last sample of 10 mM creatine and 10 mM glutamic acid. For several numerical solutions, experiments conducted with different B_1 for the same sample have been fitted simultaneously in order to gain a global solution. This is under the assumption that the relevant characteristics of the samples are independent of saturation field strength.

The fitting was done in Matlab, using the nonlinear least-squares solver *lsqcurvefit*. The data to be fitted was the experimental CEST spectra, and the function to be fitted for was the set of BM equations found in Eq. 2.26. A script conducting a BM numerical fit of

CEST spectra generated *in vivo*, simultaneously across varying pH and saturation field strength B_1, was provided by Vitaliy Khlebnikov at University Medical Center Utrecht. This script was further modified and adjusted to the *in vitro* setting with a single pH value of this work. The script was also modified to account for the spoiler recovery approach SR-CEST where necessary, and confidence intervals of the estimated parameters were added. To get an estimation of the security in the solutions obtained, the built-in Matlab function *nlparci* was utilized. As input it uses the Jacobian of the function fitted for at the solution obtained, and returns the 95% confidence intervals for the nonlinear least squares parameter estimates.

An example of a script used to fit SR-CEST spectra generated for 10 mM creatine with varying B_1 and a spoiler recovery delay of 200 ms is found in Appendix E.

3.5.1 Boundary values

In the Bloch-McConnell fitting several quantities were assumed to be known, and set as constants: The T_1 of water was measured by saturation recovery, and the concentrations of the metabolite samples were known. The concentration of water was set to 110.3 M at temperature 310 K and 111.2 M at temperature 298.1 K. All metabolites were expected to have multiple protons labile for chemical exchange. The number of labile protons was set to 3 for creatine, 6 for myo-inositol and 3 for glutamate, obtained from [10]. This left only forward exchange rate k_{sw} (in direct relation to back exchange k_{ws}), solute offset frequencies $\Delta\omega$, T_1 of the solutes and T_2 of water and solutes to be estimated.

The T_1 of the solute, $T_{1\mathrm{s}}$, was expected to be similar to $T_{1\mathrm{w}}$, as the molecules under consideration were relatively small. The initial guess for this was therefore $T_{1\mathrm{w}}$, with upper bound $T_{1\mathrm{w}}$ and lower bound 2 s.

By considering the linewidth of the metabolites in the ^{1}H-NMR spectra of the samples, an estimate for T_2^* of the solutes can be found, using the formula [1]

$$\nu_{1/2} = \frac{1}{\pi T_2^*}, \tag{3.1}$$

where $\nu_{1/2}$ is the full width at half maximum of the metabolite peak and T_2^* is the effective time constant depending on the magnetic field homogeneity. T_2 cannot be lower than this, and T_2^* was thus used as a lower bound for the BM fitting. For simplicity, the same lower boundary values were used for all pools (including water), as the estimate for T_2^* was similar ($\gtrapprox 0.4$ s) for all solutes and expected to be much lower than the real T_2 value. As T_2 cannot be higher than T_1, T_1 of water was set as upper bound for all relaxation parameter estimations.

Metabolite	Parameter	Initial guess	Lower bound	Upper bound
Creatine	k_{sw} (Hz)	810	200	3000
	ω_{0s} (ppm)	2.00	1.7	2.3
Glutamic acid	k_{sw} (Hz)	7480	4000	15000
	ω_{0s} (ppm)	3.20	2	5
Myo-inositol	k_{sw} (Hz)	2090	300	10000
	ω_{0s} (ppm)	1.00	0.7	1.3

Table 3.2: The initial guesses for exchange rate and frequency offset of solutes were retrieved from [10], where samples with pH = 7 were experimented on at 310 K. In this work pH has been 7.4, which should have some impact on the exchange rate of the solutes.

The initial guesses for ω_{0s} and k_{sw} were retrieved from [10], see Table 3.2. The upper and lower bound for the exchange rates were found by trial and error. With bounds closer to the initial guess, the numerical BM fitting did not succeed in estimating the exchange rate[1] for all experiments.

[1]The numerical BM fit tended to give the upper bound of the exchange rate as estimated parameter, indicating that the experimental spectra yielded a faster exchange rate.

Chapter 4

Results

4.1 pH measurement

The pH of a solution of 50 mM creatine in 100% H_2O was measured four times on a VWR Symphony SB70P pH meter at room temperature, giving an average of pH = 6.3. In comparison, the phosphate buffer used in the samples containing buffer had pH = 7.4.

4.2 T_1 relaxation measurements

The calculated T_1 for all samples can be found in Table 4.1, with corresponding 95% confidence intervals[1]. Plots containing the mono-exponential fit for all samples can be found in Appendix B.

[1]For the sample of combined 10 mM creatine and 10 mM glutamic acid, the 95% confidence interval obtained in Matlab was significantly larger than what was obtained for the other samples. A T_1 of 4.308 s was obtained with curve fitting in Bruker's software package TopSpin 4.0.6, and this is the T_1 value used in the numerical BM fitting.

Sample	Metabolite concentration (mM)	Phosphate concentration (mM)	T_1 (s)
Creatine	10	37.5	4.31 ± 0.03
Glutamic acid	10	37.5	4.39 ± 0.03
Myo-inositol	10	37.5	4.28 ± 0.04
Creatine + glutamic acid	10 + 10	37.5	4.18 ± 0.14
Creatine*	47.5	37.5	3.40 ± 0.03
Creatine**	45	0	4.12 ± 0.03
Creatine	45	10	4.26 ± 0.03
Creatine	45	37.5	4.11 ± 0.03

Table 4.1: Estimated T_1 for all the different samples at 310 K. * was measured at 298.1 K. ** was not in a buffer, but in pure H_2O with 10% D_2O.

4.3 Test and verification of the SR-CEST

The proposed spoiler recovery approach (SR-CEST) was tested on a 47.5 mM creatine sample at 298.1 K for eight different spoiler recovery delays (SRD): 1 ms, 100 ms, 500 ms, 1 s, 2 s, 3 s, 6 s and 16 s, in addition to a regular CEST sequence for comparison. The goal was to document the performance of the spoiler recovery approach combined with the CEST sequence, and verify that the results correspond with what is found with regular CEST and with what is expected of the system. A change in signal from the CEST effect as a function of SRD is expected, following Eq. 2.21. An SRD of 16 s yields the same scan time as regular CEST with repetition time TR = 16 s, while shorter SRDs reduce it. In this experiment the shortest SRD was 1 ms, to explore how the sequence work even with minimal SRD.

4.3.1 Comparison between SR-CEST and regular CEST

CEST spectra were generated for the regular CEST and all SR-CEST experiments. The spectrum for regular CEST and the spectrum for SR-CEST with SRD = 16 s are found in Figures 4.2a) and 4.2b). All other CEST spectra are found in Appendix C.

With increasing SRD, a decreasing signal (meaning an increasing amplitude) from the creatine dip was observed, as the net magnetization has more time to re-equilibrate before the regular CEST sequence is conducted. This enables more magnetization for saturation, and can be seen in Figure 4.1. The signal strength seems to follow an exponential decay $f(\text{SRD}) = a - b \cdot e^{-c \cdot \text{SRD}}$, with $a = 0.6531, b = -0.06294, c = 0.3679$. From Eq. 2.21 a

relaxation time of $T_1 = 1/c = 2.7181$ is obtained. This is not necessarily reflecting the water T_1 relaxation time of the system, as the change in signal also is driven by T_1 of creatine, chemical exchange between water and creatine and other parameters modelled for in the numerical BM fitting.

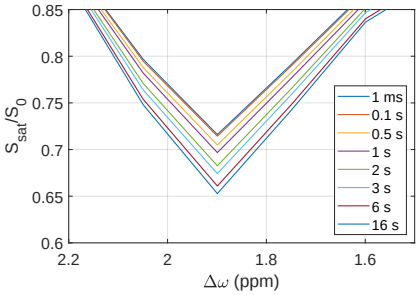

(a) The amplitude of the CEST dip around 2 ppm for different SRDs.

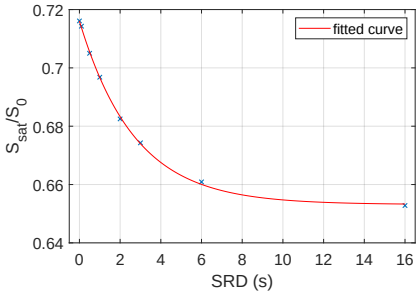

(b) The change in amplitude of the CEST dip as a function of SRD.

Figure 4.1: The change in signal of the creatine dip as a result of varying SRDs. a) shows the part of the obtained spectra found between 1.6 ppm and 2.2 ppm for varying SRDs. It is clear that the normalized signal of the creatine dip decreases as SRD increases. This behaviour is seen in b), where a mono-exponential curve is fitted for the normalized signal of the creatine dip as a function of SRD.

With a T_1 of 3.4 s is it expected that that the system is very close to thermal equilibrium with an SRD of 16 s, and there should be no difference between SR-CEST and regular CEST. The difference between the normalized spectra for these cases can be seen in Figure 4.2c). There is a notable difference between the spectra at 0 ppm, but it is still quite small (less than one percent of the normalized spectra). This could be caused by a slight phase shift between the spectra, possibly originating in an imprecise transmitter frequency offset during acquisition. There is no significant difference observed around 2 ppm, where the creatine CEST dip is located. This indicates that the CEST contrast is identical for SR-CEST with SRD = 16 s and regular CEST with TR = 30 s.[2]

[2] As this sample had a calculated T_1 of 3.4 s, a TR of 16 s for the regular CEST spectrum should yield the same result. The difference between spectra with TR = 16 s and TR = 30 s is negligible in this case.

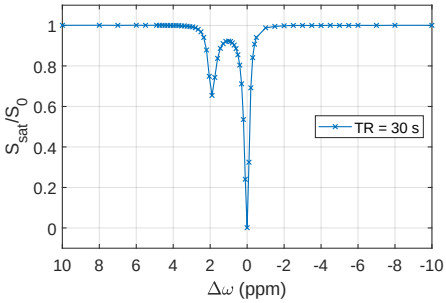

(a) Regular CEST with TR = 30 s.

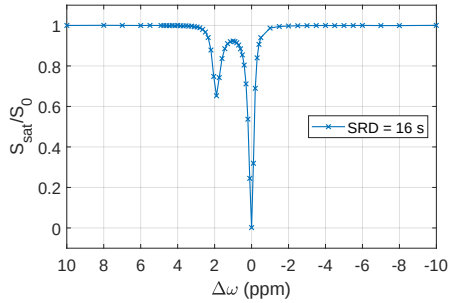

(b) SR-CEST with SRD = 16 s.

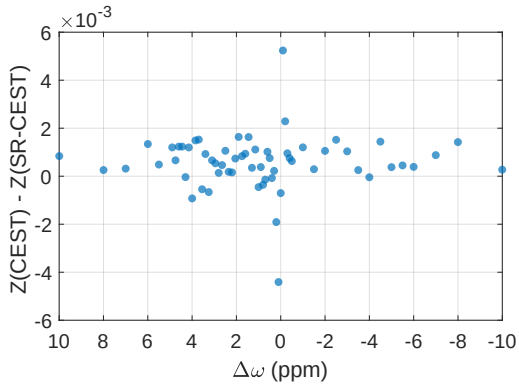

(c) Difference between the normalized CEST spectra created with a) regular CEST with TR = 30 s and b) SR-CEST with SRD = 16 s.

Figure 4.2: CEST spectra obtained with: a) a regular CEST sequence with a repetition time (TR) of 16 s and b) with SR-CEST with a spoiler recovery delay (SRD) of 16 s. The difference between the two spectra is found in c). There is an observable difference between the spectra at 0 ppm, which could be caused by a slight phase shift between the spectra. The temperature is 298.1 K, and the sample is 47.5 mM creatine in a phosphate buffer. $B_1 = 1$ μT.

4.3.2 Numerical BM fitting of CEST and SR-CEST spectra

If the new SR-CEST sequence is functioning as expected, the SR-CEST spectra should yield the same information about the sample under consideration as the regular CEST spectra. To investigate this the numerical BM fitting described in Section 2.4.2 was applied to the regular and spoiler recovery CEST spectra. In this fitting, the signal change as a result of SRD has been taken into account (see Section 2.4.2.2), and the estimated exchange rate k_{sw}, offset frequency $\Delta\omega$ and relaxation parameters should be the same for every fit.

All the fitted spectra can be found in Appendix D.1, whereas the residuals from the BM fitting for all SR-CEST spectra is found in Figure 4.3a). For the lowest SRDs the

algorithm succeeds in making a suitable fit, but as SRD increases, the residuals around 2 ppm increases. This shows that the amplitude of the fitted creatine dip does not reach the experimentally obtained dip. Also for the spectrum obtained with regular CEST in Figure 4.4a) the numerical fitting gives a significantly smaller amplitude of the dip, indicating that this underestimation does not origin in the SR-CEST approach. For all spectra there are notable residuals around 0 ppm. This is where the change in signal is strongest, making the residual plot more prone to high residuals. It is thus expected that this is where the highest residuals are. Nevertheless, the residuals seem to follow a pattern of being positive downfield of 0 ppm and negative upfield of 0 ppm, indicating that there is a slight phase shift between the experimental and fitted spectra.

Table 4.2: Estimated quantities with a 95% confidence interval in a sample of 47.5 mM creatine in a phosphate buffer for different SRDs, with last row for regular CEST. The temperature is 298.1 K and $B_1 = 1$ μT, and T_1 of water was measured to be 3.4 s. * indicates that the estimation has reached a lower or upper bound.

SRD (s)	k_{sw} (s^{-1})	$\Delta\omega$ (ppm)	T_{2s} (s)	T_{2w} (s)	T_{1s} (s)
0.001	746 ± 54	1.93 ± 0.01	2.8 ± 319	3.4* ± 1.5	3.4 ± 14
0.1	747 ± 55	1.93 ± 0.01	3.4* ± 449	3.4* ± 1.5	3.4 ± 15
0.5	757 ± 54	1.93 ± 0.01	3.4* ± 466	3.4* ± 1.5	3.4* ± 17
1	767 ± 71	1.93 ± 0.01	3.4* ± 676	3.4* ± 1.8	3.4* ± 20
2	783 ± 94	1.93 ± 0.01	3.4* ± 942	3.4* ± 2.3	3.4* ± 28
3	787 ± 116	1.93 ± 0.02	3.4* ± 1280	3.3 ± 2.5	3.4* ± 38
6	785 ± 159	1.93 ± 0.03	3.4* ± 1941	2.9 ± 2.5	3.4* ± 76
16	782 ± 209	1.93 ± 0.03	3.4* ± 2850	2.7 ± 2.4	3.4* ± 241
Reg. CEST	788 ± 201	1.93 ± 0.03	3.4* ± 2840	2.9 ± 2.6	3.4* ± 279

The estimated parameters found in the Bloch-McConnell (BM) fitting can be seen in Table 4.2. The estimate for the exchange rate k_{sw} is quite consistent, although increasing with increasing SRD. This can be interpreted as an attempt to make the amplitude of the CEST dip greater, but as seen in the increasing residuals in Figure 4.3a) it does not succeed in making a perfect fit. It is as though the concentration used in the script is too low to provide a good fit. The estimate for $\Delta\omega$ is stable for all SRDs, but the fit repeatedly reaches the upper bound for all relaxation time parameters. The 95% confidence interval of the relaxation time parameters is very large, especially for T_{2s} and T_{1s}. These parameters in the current conditions have a relatively small impact on the shape of the CEST spectrum, which makes it challenging to find their exact value through least square curve fitting. This is why exchange rate and offset frequency should be considered the most important

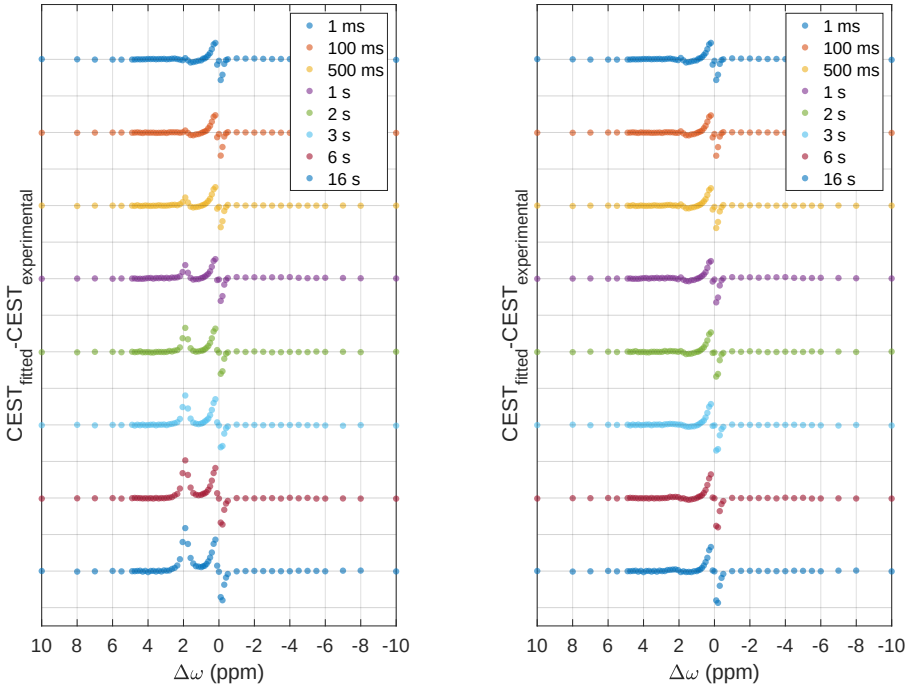

(a) Residuals of BM fitting for SR-CEST spectra obtained with eight varying spoiler recovery delays (SRD), and keeping concentration a fixed parameter.

(b) Residuals of BM fitting for SR-CEST obtained with eight varying spoiler recovery delays (SRD), and letting concentration of creatine vary between 30 and 70 mM.

Figure 4.3: The difference between the CEST spectra simulated in the BM fitting and the experimental CEST spectra as a function of offset frequency. All residual plots are aligned around 0 signal difference on the y-axis, and the difference between two horizontal lines is 0.05, or 5% of the normalized CEST spectra. Each residual plot represents an experiment conducted for a certain SRD. In a) the fit is made for the known concentration of the sample, whereas b) shows the fit made when the concentration is a parameter free to vary between 30 mM and 70 mM. A positive residual indicates that the amplitude of the fit is too small, giving a lesser CEST dip than what is experimentally obtained. The temperature is 310 K, saturation field strength B_1 is 1 μT and the sample is 47.5 mM creatine in a phosphate buffer.

variables to extract from the BM fitting.

As a test the concentration was used as a variable in the BM fitting, although the exact concentration was known. The resulting quantities can be found in Table 4.3. All the fitted spectra can be found in Appendix D.1, whereas the residuals of the fitting are found in Figures 4.3b) and 4.4b). As expected, the estimated concentration increases with increasing

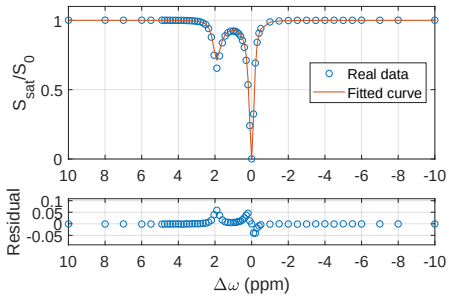

(a) Fitting of a regular CEST spectrum with concentration kept a fixed parameter.

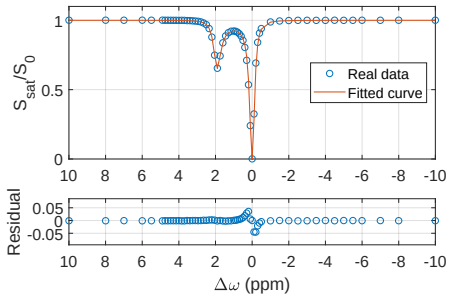

(b) Fitting of a regular CEST spectrum with concentration as a variable.

Figure 4.4: BM fitting of regular CEST spectra obtained with a repetition time (TR) of 30 s. The temperature is 298.1 K, and the sample is 47.5 mM creatine in phosphate buffer. $B_1 = 1$ μT. In Figure 4.4a) the concentration is kept a fixed quantitiy in the fitting, while it in Figure 4.4b) is free to vary between 30 mM and 70 mM. It is then estimated to be 57.0 mM.

SRD, providing an excellent fit for all SRDs and the regular CEST experiment. This can be seen in the residual plots in Figures 4.3b) and 4.4b), where there are no longer increasing residuals around 2 ppm for increasing SRD. This shows that estimated parameters that does not correspond to the physical parameters can be solutions of the numerical BM fitting. In the case of varying concentration, the estimated exchange rate decreases with increasing SRDs, and the estimations for the relaxation time constants are unstable. The calculated confidence interval increases with increasing SRD for both concentration and exchange rate of creatine. Both exchange rate and concentration contributes to the magnitude of the creatine dip, and the concomitant change in insecurity can mirror a difficulty in separating the contributions from these two variables.

Although the change in exchange rate with increasing SRD shows different behavior for the BM fitting with fixed concentration and varying concentration, it is worth noting that both the exchange rate and offset frequency of creatine is estimated to be quite similar for both fittings.

Table 4.3: Estimated quantities in a sample of 47.5 mM creatine in a phosphate buffer for different SRDs, with last row for regular CEST. Here concentration of the solute [s] is free to vary between 30 mM and 70 mM. The temperature is 298.1 K and $B_1 = 1$ μT, and T_1 of water was measured to be 3.4 s. * indicates that the estimation has reached a lower or upper bound.

SRD (s)	k_{sw} (s^{-1})	[s] (mM)	$\Delta\omega$ (ppm)	T_{2s} (s)	T_{2w} (s)	T_{1s} (s)
0.001	746 ± 53	47.5 ± 2.0	1.93 ± 0.01	3.4* ± 450	3.4* ± 1.6	3.4 ± 16
0.1	745 ± 53	47.7 ± 2.1	1.93 ± 0.01	3.4* ± 422	3.4* ± 1.6	3.0 ± 14
0.5	741 ± 61	48.8 ± 2.2	1.93 ± 0.01	3.4* ± 605	3.4* ± 1.7	3.4* ± 19
1	739 ± 64	49.9 ± 2.4	1.93 ± 0.01	3.4* ± 710	3.4* ± 1.7	3.4* ± 21
2	730 ± 75	52.0 ± 2.8	1.93 ± 0.01	3.4* ± 931	3.4* ± 1.8	2.0* ± 9
3	724 ± 111	53.4 ± 3.7	1.93 ± 0.01	0.4* ± 22	3.4* ± 2.3	2.0* ± 12
6	714 ± 122	55.7 ± 4.7	1.93 ± 0.02	0.4* ± 24	3.4* ± 2.5	2.0* ± 22
16	707 ± 142	57.2 ± 16.2	1.93 ± 0.02	0.4* ± 27	3.4* ± 3.1	2.0* ± 185
Reg. CEST	708 ± 154	57.0 ± 22.7	1.93 ± 0.02	0.4* ± 27	3.4* ± 3.7	2.0* ± 294

4.4 Impact of the phosphate buffer on chemical exchange rate

The phosphate buffer used to control the pH in the samples may work as a catalyst for the chemical exchange, modifying the exchange rate of the system under consideration. To examinate this, CEST experiments were run on a sample of 45 mM creatine solute in pure water, with 10% D_2O to obtain a lock signal for the experiment. To compare with the buffer-free solution, a sample of 45 mM creatine in two different buffer concentrations were experimented on: one with a buffer containing 10 mM phosphate, and another containing 37.5 mM phosphate. The concentration of phosphate in the buffer used for all other samples in this work was 37.5 mM, while 10 mM phosphate assimilate an *in vivo* setting [10].

4.4.1 CEST spectra without phosphate buffer

The pH in the solution of 45 mM creatine in H_2O was measured to be 6.3 at room temperature in section 4.2. In comparison, the phosphate buffer provides a pH of 7.4. The CEST experiments were run at 310 K, giving some insecurity in the actual pH value during the experiments. The CEST sequences were run for six different saturation field strengths, $B_1 = 1, 2, 3, 4, 5$ and 8 μT. This was done for regular CEST with TR = $5 \cdot T_1$, and SR-CEST with SRD = 200 ms and SRD = T_1 = 4.1 s, which gives a total of 18 different CEST spectra.

All spectra can be seen in Figure 4.5.

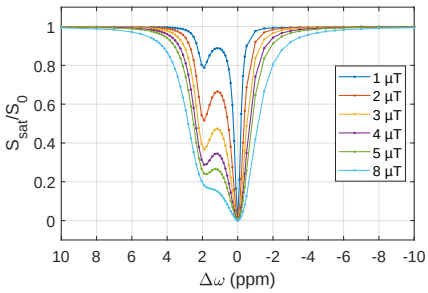

(a) SR-CEST with SRD = 200 ms.

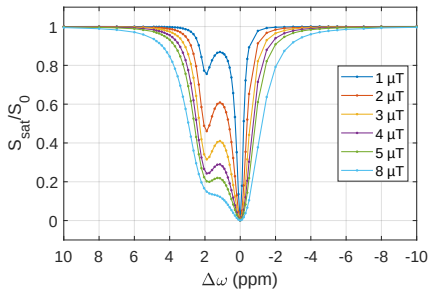

(b) SR-CEST with SRD = 4.1 s.

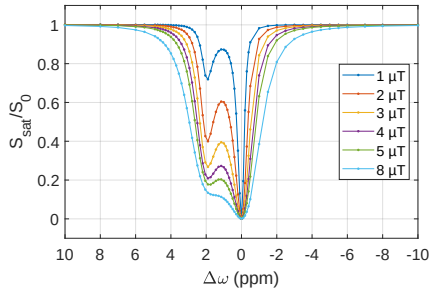

(c) Regular CEST.

Figure 4.5: CEST spectra generated with different CEST sequences for varying B_1. The amplitude of the creatine dip around 2 ppm is smallest for SRD = 200 ms, and largest for the regular CEST. The temperature is 310 K and the sample is 45 mM creatine in water with 10% D_2O.

4.4.1.1 Numerical BM fitting of CEST spectra

The spectra obtained for the different saturation field strengths were BM fitted simultaneously, giving three global solutions (one for each SRD, and one for the regular CEST). The residuals of the fitted CEST spectra can be found in Figure 4.6, with all corresponding estimated parameters in Table 4.4. Figures for all fitted CEST spectra can be found in Appendix D.2.

In Figure 4.6a), for SRD = 200 ms, the amplitude of the creatine dip around 2 ppm is repeatedly estimated to be larger than what is obtained experimentally. For the case of SRD = 4.1 s in Figure 4.6b) the amplitude of the creatine dip differs between being too small and too large, while the estimates for regular CEST in Figure 4.6c) tend to be too small. This shows a similar behavior to what was seen in Section 4.3, where the change in amplitude of the creatine dip with varying SRD was examined.

It appears that the quality of the fit differs with B_1, indicating difficulties with obtaining a valid global solution for all B_1.

Table 4.4: Estimated quantities with a 95% confidence interval in a sample of 45 mM creatine in water with 10% D_2O at 310 K, where T_1 of water was measured to be 4.12 s. * indicates that the estimation has reached a lower or upper bound.

SRD	k_{sw} (s^{-1})	$\Delta\omega$ (ppm)	T_{2s} (s)	T_{2w} (s)	T_{1s} (s)
200 ms	1237 ± 52	1.98 ± 0.01	0.40^* ± 2.12	1.82 ± 0.33	0.40^* ± 1.72
4.1 s	1581 ± 54	2.00 ± 0.01	0.40^* ± 4.42	2.43 ± 0.38	4.12^* ± 94
Reg. CEST	1556 ± 74	2.02 ± 0.01	4.12^* ± 684	3.08 ± 0.73	4.12^* ± 101

Although the residuals are varying with varying B_1 and CEST sequence (SR-CEST or regular CEST), the exchange rate k_{sw} and offset frequency of creatine are estimated to similar values. The largest deviation is found for SR-CEST with SRD = 200 ms, while SR-CEST with SRD = 4.1 s and regular CEST have overlapping 95% confidence interval. The estimates for the relaxation time constants differs between all experiments, making it challenging to make any statements about them.

Given an exchange rate of 1500 s^{-1} and offset frequency of 2 ppm, the relation

$$\frac{k_{sw}}{\Delta\omega \cdot 600.23\ \text{MHz}} = \frac{1500\ \text{s}^{-1}}{2 \cdot 600.23\ \text{Hz}} = 1.25 \tag{4.1}$$

can be obtained, indicating an intermediate exchange regime.

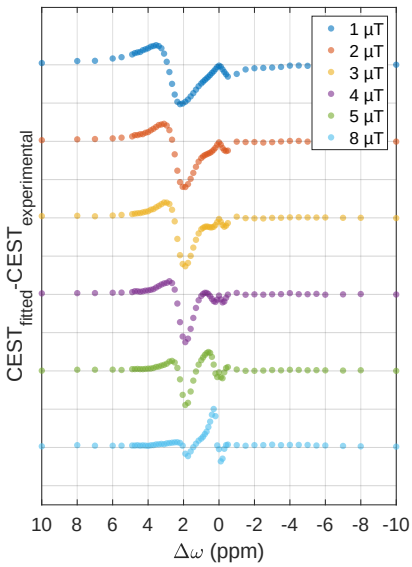

(a) SR-CEST with SRD = 200 ms.

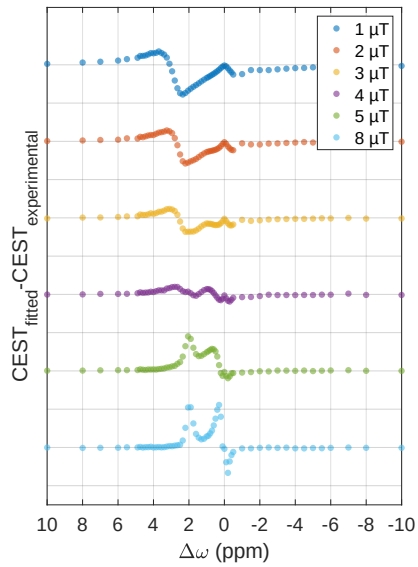

(b) SR-CEST with SRD = 4.1 s.

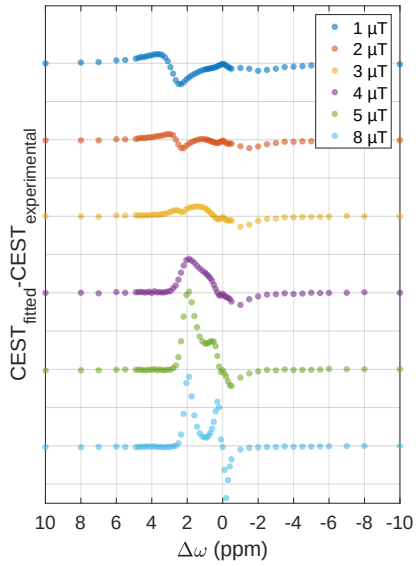

(c) Regular CEST.

Figure 4.6: The differences between the fitted and experimental CEST spectra as a function of offset frequency. Each figure represents a CEST sequence, conducted for six different saturation field strengths B_1. All residual plots are aligned around 0 signal difference on the y-axis, and the difference between two horizontal lines is 0.05, or 5% of the normalized CEST spectra. A positive residual indicates that the amplitude of the fit is too small, giving a lesser CEST dip than what is experimentally obtained. The temperature is 310 K, and the sample is 45 mM creatine in water with 10% D_2O.

4.4.2 CEST spectra with buffer containing 10 mM phosphate

Two different SR-CEST sequences were run for the sample of 45 mM creatine in a buffer containing 10 mM phosphate, with SRD = 200 ms and SRD = T_1 = 4.3 s. Both SR-CEST experiments were conducted for six different B_1: 1, 2, 3, 4, 5 and 8 µT. The generated CEST spectra can be found in Figure 4.7. The creatine dips in Figure 4.7 are wider than what was observed in Figure 4.5 for the case with no buffer present. Given the intermediate exchange regime of the sample with no phosphate buffer the widening of the peaks could indicate an increase in exchange rate (see Section 2.2.2).

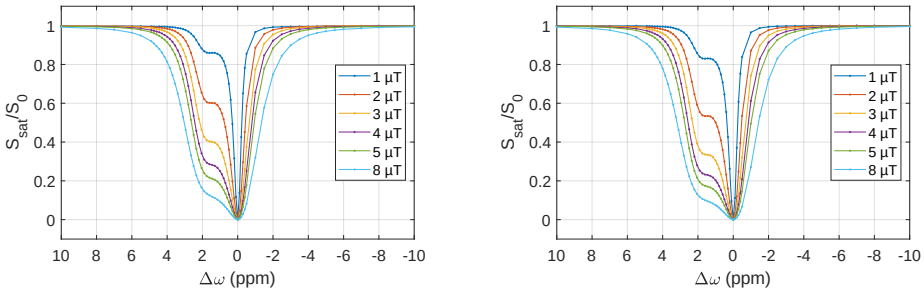

(a) SR-CEST with SRD = 200 ms.

(b) SR-CEST with SRD = 4.3 s.

Figure 4.7: CEST spectra generated with different SR-CEST sequences for varying B_1. The temperature is 310 K and the sample is 45 mM creatine in a buffer containing 10 mM phosphate.

4.4.2.1 Numerical BM fitting of CEST spectra

The spectra obtained for the different saturation field strengths were BM fitted simultaneously, giving two global solutions (one for each SRD). The residuals of the fitted CEST spectra can be found in Figure 4.8, with all corresponding estimated parameters in Table 4.5. Figures for all fitted spectra can be found in Appendix D.3.

In Figure 4.8a) for SRD = 200 ms the trend is that the creatine peak is estimated to be larger than what is experimentally obtained, giving negative residuals about 2 ppm. In Figure 4.8b) the trend appears to be opposite, although not as clear, with a smaller CEST dip than what is experimentally obtained. This can be seen in relation to the results presented in Section 4.3, where residuals around 2 ppm got more and more positive with increasing SRD.

In Table 4.5 the exchange rate of creatine is estimated to be around 2500 s^{-1} for both SRD = 200 ms and SRD = 4.3 s. This is about 1000 s^{-1} higher than for the 45 mM creatine solution with no buffer (Table 4.4), indicating that there is a drastic increase in exchange

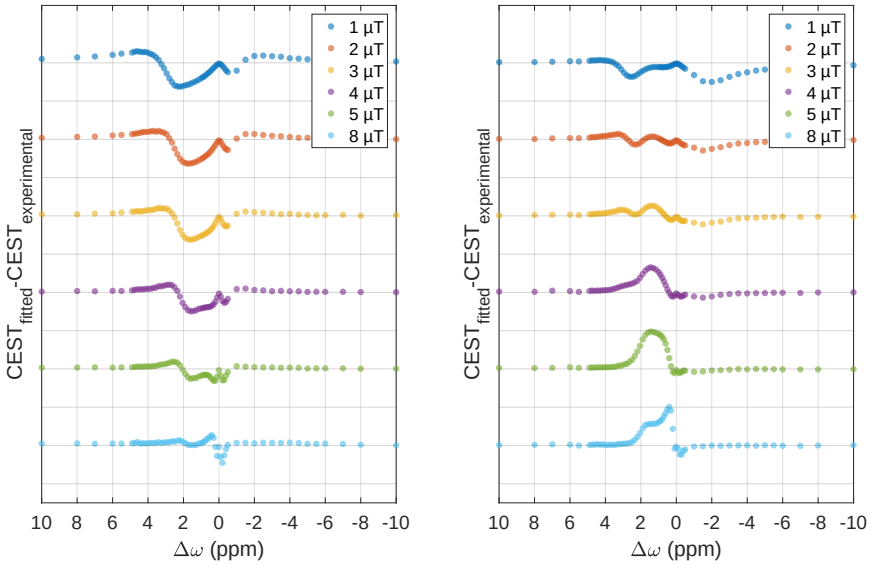

(a) SR-CEST with SRD = 200 ms.

(b) SR-CEST with SRD = 4.3 s.

Figure 4.8: The difference between the simulated CEST spectra and the experimentally obtained CEST spectra as a function of offset frequency. Each figure represents a CEST sequence, conducted for six different saturation field strengths B_1. All residual plots are aligned around 0 signal difference on the y-axis, and the difference between two horizontal lines is 0.05, or 5% of the normalized CEST spectra. A positive residual indicates that the amplitude of the fit is too small, giving a lesser CEST dip than what is experimentally obtained. The temperature is 310 K, and the sample is 45 mM creatine in a buffer containing 10 mM phosphate.

rate when a buffer containing 10 mM phosphate is added. The estimated $\Delta\omega$ in Table 4.5 has a larger variation than what was observed in Table 4.4, but is still situated around 2 ppm. The relaxation time parameters vary greatly, as seen before.

The pH difference between the solution with buffer (pH = 7.4) and without buffer (pH = 6.3) is 1.1. pH is known to have an impact on the exchange rate, and changes in pH is one of the microenvironmental properties detectable with CEST [2]. The 1000 s^{-1} increase in exchange rate could be caused by the buffer as a catalyst, but even more likely the change in pH. This is reflected in other literature [20], stating that the exchange rate of the creatine guanidinium protons can be catalyzed by increasing pH.

Table 4.5: Estimated quantities with a 95% confidence interval in a sample of 45 mM creatine in a buffer containing 10 mM phosphate at 310 K, where T_1 of water was measured to be 4.26 s. * indicates that the estimation has reached a lower or upper bound.

SRD	k_{sw} (s^{-1})	$\Delta\omega$ (ppm)	T_{2s} (s)	T_{2w} (s)	T_{1s} (s)
200 ms	2516 ± 59	1.97 ± 0.01	1.33 ± 0.49	4.26* ± 1.86	0.40* ± 0.81
4.3 s	2555 ± 65	2.05 ± 0.01	3.78 ± 11	1.64 ± 0.25	4.26* ± 76

4.4.3 CEST spectra with buffer containing 37.5 mM phosphate

Two different SR-CEST sequences were run for the sample of 45 mM creatine in a buffer containing 37.5 mM phosphate, with SRD = 200 ms and SRD = T_1 = 4.1 s. Both SR-CEST experiments were conducted for six different B_1: 1, 2, 3, 4, 5, and 8 µT. The generated CEST spectra can be found in Figure 4.9. The creatine dip is narrower than what was observed in Section 4.4.2 for a buffer containing 10 mM phosphate, but wider than what was observed with no buffer present in Section 4.4.1. This again indicates that the exchange rate of creatine has changed with phosphate concentration, this time towards a slower exchange regime.

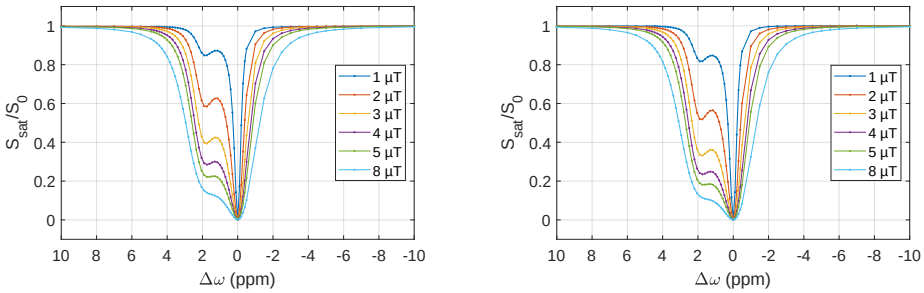

(a) SR-CEST with SRD = 200 ms.

(b) SR-CEST with SRD = 4.1 s.

Figure 4.9: CEST spectra generated with different SR-CEST sequences for varying B_1. The temperature is 310 K and the sample is 45 mM creatine in a buffer containing 37.5 mM phosphate.

4.4.3.1 Numerical BM fitting of CEST spectra

The spectra obtained for the different saturation field strengths were BM fitted simultaneously, giving two global solutions (one for each SRD). The residuals of the fitted CEST spectra can be found in Figure 4.10, with all corresponding estimated parameters in Table 4.6. Figures for all fitted spectra can be found in Appendix D.4.

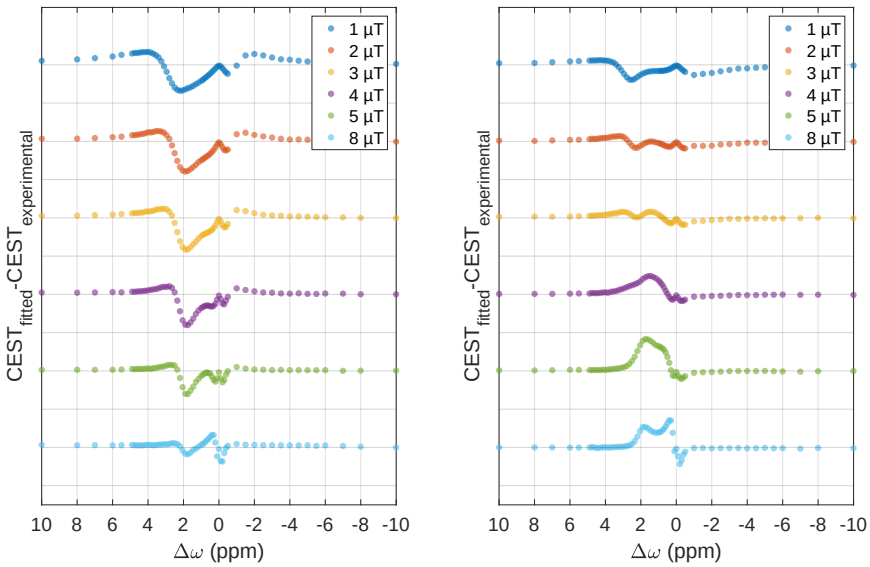

(a) SR-CEST with SRD = 200 ms.

(b) SR-CEST with SRD = 4.1 s.

Figure 4.10: The difference between the simulated CEST spectra and the experimentally obtained CEST spectra as a function of offset frequency. Each figure represents a CEST sequence, conducted for six different saturation field strengths B_1. All residual plots are aligned around 0 signal difference on the y-axis, and the difference between two horizontal lines is 0.05, or 5% of the normalized CEST spectra. A positive residual indicates that the amplitude of the fit is too small, giving a lesser CEST dip than what is experimentally obtained. The temperature is 310 K, and the sample is 45 mM creatine in a buffer containing 37.5 mM phosphate.

Also for this case of 37.5 mM phosphate content in the sample, the trend for SRD = 200 ms, in Figure 4.10a), is that the creatine peak is estimated to be larger than what is experimentally obtained. As in Section 4.4.2 the residuals around 2 ppm for SRD = T_1 vary between being positive or negative, although a too small amplitude of the creatine dip appears to have the strongest tendency.

In Table 4.6 the exchange rate of creatine is estimated to be around 2000 s^{-1}. This is a slower exchange rate than what was estimated in Section 4.4.2 for a buffer content of 10 mM phosphate, but faster than Section 4.4.1 with no buffer present. It is thus clear that the buffer modifies the exchange rate of the creatine samples, and supposedly also for the other metabolites.

In [20] the exchange rate of the creatine guanidinium protons was determined for five different buffer concentrations in the range of $c_{\text{buffer}} = [10, 150]$ mM at pH $\approx 6 \pm 0.2$ and fixed temperature T = 19°C. They observed no dominant exchange catalysis by solute

Table 4.6: Estimated quantities with a 95% confidence interval in a sample of 45 mM creatine in a buffer containing 37.5 mM phosphate, where T_1 of water was measured to be 4.11 s. * indicates that the estimation has reached a lower or upper bound.

SRD	k_{sw} (s^{-1})	$\Delta\omega$ (ppm)	T_{2s} (s)	T_{2w} (s)	T_{1s} (s)
200 ms	1897 ± 53	1.98 ± 0.01	0.40* ± 0.73	4.11* ± 1.58	0.40* ± 0.94
4.3 s	2096 ± 44	2.04 ± 0.01	4.04 ± 61	2.36 ± 0.36	4.11* ± 60

phosphate, but a reduction of the measured k_{sw} with increasing buffer concentration was detected. This is in agreement with the observations made in this work, and verifies a dominant base-catalyzed and a weak buffer-catalyzed proton exchange – the change in pH from 6.3 to 7.4 is likely to be what makes the exchange rate increase between the sample with no buffer content to the sample with a 10 mM phosphate buffer, but the concentration of the buffer can also alter the exchange rate.

It is not straightforward to transfer these result to phantoms containing other metabolites than creatine, but it is likely that the buffer chosen – whether it is the contents of the buffer or the pH – has impact on the exchange rate and thus the appearance of the CEST spectrum. A direct comparison with other literature where experiments in different buffer environments have been conducted is therefore not necessarily valid.

4.5 CEST of different metabolites

The proposed SR-CEST and regular CEST was applied on samples containing varying metabolites with protons expected to exchange. These were 10 mM creatine, 10 mM myo-inositol, 10 mM glutamic acid[3] and a sample containing both 10 mM glutamic acid and 10 mM creatine, all in a phosphate buffer containing 37.5 mM phosphate. The temperature for all experiments were 310 K.

Both creatine, myo-inositol and glutamic acid are among common cellular metabolites, and have all been reported to give high CEST contrast in brain [10] as well as in breast cancer [7].

4.5.1 Creatine

Experiments were run for the sample of 10 mM creatine with four different saturation field strengths B_1: 1, 2, 3 and 8 μT. Based on the assumed exchange rate of creatine (~ 800

[3]In other literature often referred to as its anion, glutamate.

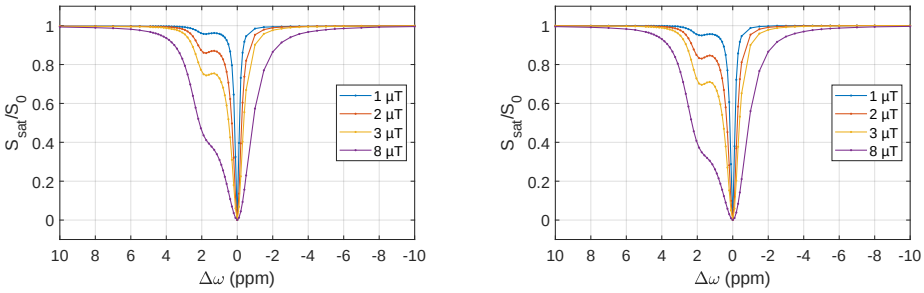

(a) SRD = 200 ms.

(b) SRD = T_1 = 4.3 s

Figure 4.11: SR-CEST spectra generated with a) SRD = 200 ms and b) SRD = 4.3 s for varying B_1. The temperature is 310 K and the sample is 10 mM creatine in a phosphate buffer.

s^{-1}) the CEST effect was expected to be best detectable for low B_1 [10], while B_1 = 8 μT was applied as an extreme, and to enable comparison with other samples where such a high saturation field strength was suitable.

For the creatine sample SR-CEST was run for SRD = 200 ms and SRD = T_1 = 4.3 s, with resulting CEST spectra in Figure 4.11.

4.5.1.1 Numerical BM fitting of creatine CEST spectra

The CEST spectra were BM fitted simultaneously over the varying B_1, giving one global solution for SRD = 200 ms and one for SRD = 4.3 s.

The residuals of the fitted CEST spectra can be found in Figure 4.12, with corresponding estimated parameters in Table 4.7. Figures containing all spectra with corresponding BM fitting can be found in Appendix D.5. The BM fitted spectra appear to give a good fit for both SRDs, although there are significant residuals for some B_1 values. The residuals around 2 ppm, where the creatine dip is located, are in some cases approaching 5% of the normalized CEST spectra. For SRD = 200 ms the estimated amplitude of the creatine dip appears to overall fit the experimentally obtained spectra, whereas the estimated dip is generally too small for SRD = 4.3 s.

The two solutions give similar estimations for the exchange rate and frequency offset of creatine and T_2 of water, while it is challenging to make a conclusion about the remaining relaxation parameters T_{1s} and T_{2s}. The estimated exchange rate of creatine, ~ 2100 s^{-1}, is more than 1000 s^{-1} higher than what was expected from [10], but other literature suggest a higher exchange rate in the range of 2000 s^{-1} [20]. The estimated exchange rate of ~ 2000 s^{-1} for 45 mM creatine in a 37.5 mM phosphate buffer corresponds with the exchange rate found here, although the results obtained for 10 mM creatine appear somewhat larger.

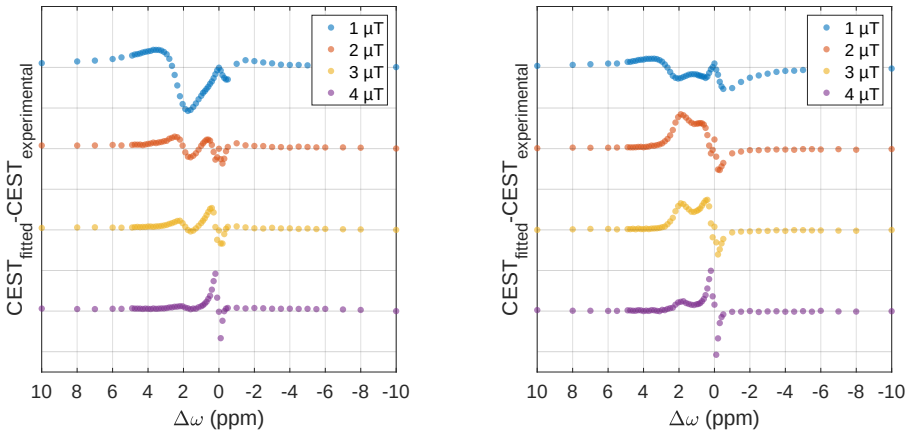

(a) SR-CEST with SRD = 200 ms.

(b) SR-CEST with SRD = 4.3 s.

Figure 4.12: The difference between the BM fitted and experimental CEST spectra as a function of offset frequency. All residual plots are aligned around 0 signal difference on the y-axis, and the difference between two horizontal lines is 0.05, or 5% of the normalized CEST spectra. Each residual plot represents an experiment conducted for a certain saturation field strength B_1, where a) shows residual plots for four different B_1 obtained with SRD = 200 ms, and b) shows four residual plots obtained with SRD = 4.3 s. A positive residual indicates that the amplitude of the fit is too small, giving a lesser CEST dip than what is experimentally obtained. The temperature is 310 K and the sample is 10 mM creatine in a phosphate buffer.

Equal exchange rates are expected between these two samples, as exchange rate should be independent of CEST agent concentration [21].

Table 4.7: Estimated quantities with a 95% confidence interval in a sample of 10 mM creatine in a phosphate buffer at 310 K, where T_1 of water was measured to be 4.31 s. * indicates that the estimation has reached a lower or upper bound.

SRD	k_{sw} (s^{-1})	$\Delta\omega$ (ppm)	T_{2s} (s)	T_{2w} (s)	T_{1s} (s)
200 ms	2061 ± 117	1.96 ± 0.02	0.40* ± 6	2.75 ± 0.42	2.08 ± 44
4.3 s	2259 ± 140	2.02 ± 0.02	3.00 ± 22	2.38 ± 0.33	4.31* ± 473

4.5.2 Myo-inositol

The sample of 10 mM myo-inositol was tested for six different saturation field strengths B_1: 1, 2, 3, 4, 5 and 8 μT. SR-CEST was run for SRD = 200 ms and SRD = T_1, in addition to a regular CEST sequence with B_1 = 1 μT for control. Compared to the sample of 10 mM

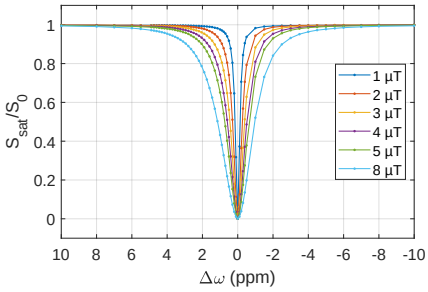

(a) SRD = 200 ms.

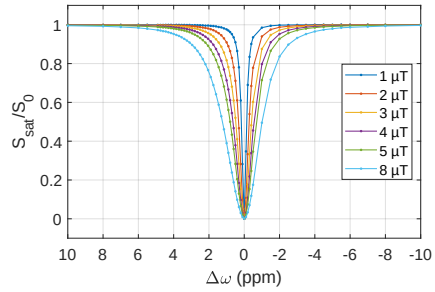

(b) SRD = T_1 = 4.3 s.

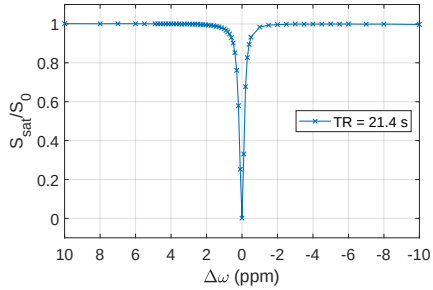

(c) Regular CEST.

Figure 4.13: SR-CEST spectra generated with a) SRD = 200 ms and b) SRD = 4.3 s for varying B_1, and a regular CEST spectrum c) for B_1 = 1 µT. The temperature is 310 K and the sample is 10 mM myo-inositol in a phosphate buffer.

creatine there is no visible dip downfield, but by visually examining the spectra in Figures 4.13a), 4.13b) and 4.13c) a slight asymmetry around 0 ppm can be recognized. It is most notable for high B_1, indicating that a high B_1 is required in this case to gain good CEST contrast.

4.5.2.1 Numerical BM fitting of myo-inositol CEST spectra

The spectra obtained for each SRD were BM fitted simultaneously, giving two global solutions; for SRD = 200 ms in Figure 4.14a) and SRD = 4.3 s in Figure 4.14b). Only the single regular CEST spectrum was subject to the regular fitting seen in Figure 4.15. All fitted spectra can be found in Appendix D.6. The corresponding estimations for all fittings can be seen in Table 4.8.

The estimations for the two SRDs are similar for all variables, but the estimations for the regular CEST differs greatly from these. The large deviation in the BM fitting of the regular CEST spectrum can to some extent be explained by the scarse data material. Only

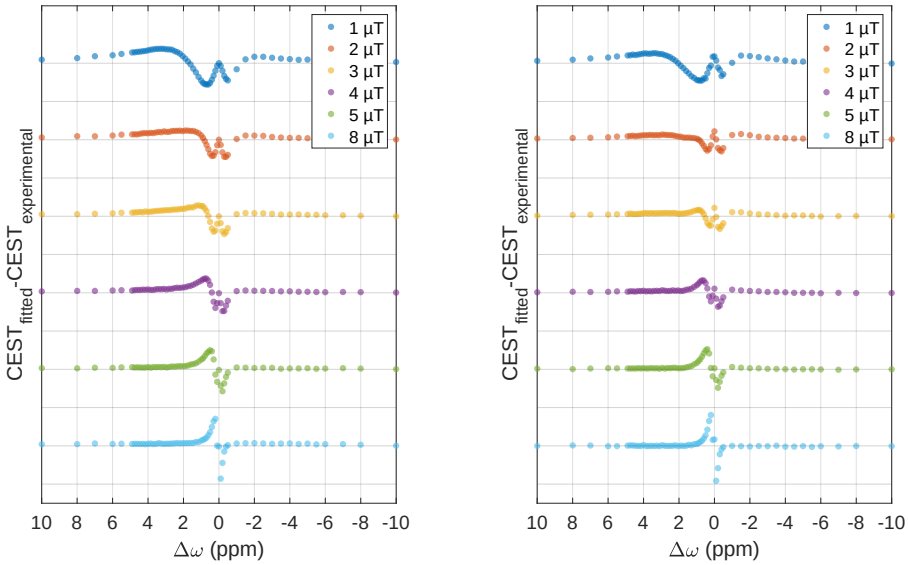

(a) SR-CEST with SRD = 200 ms.

(b) SR-CEST with SRD = 4.3 s.

Figure 4.14: The difference between the BM fitted and experimental CEST spectra as a function of offset frequency. All residual plots are aligned around 0 signal difference on the y-axis, and the difference between two horizontal lines is 0.05, or 5% of the normalized CEST spectra. Each residual plot represents an experiment conducted for a certain saturation field strength B_1, where a) shows residual plots for six different B_1 obtained with SRD = 200 ms, and b) shows six residual plots obtained with SRD = 4.3 s. A positive residual indicates that the amplitude of the fit is too small, giving a lesser CEST dip than what is experimentally obtained. The temperature is 310 K and the sample is 10 mM myo-inositol in a phosphate buffer.

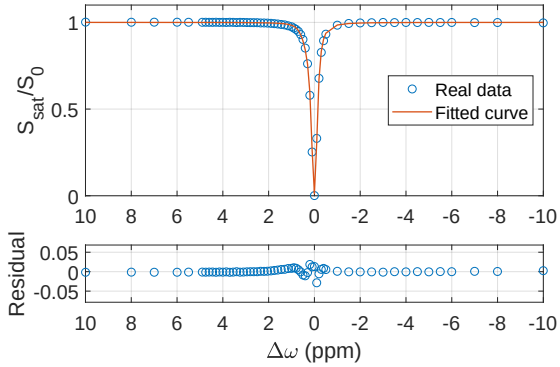

Figure 4.15: CEST spectrum generated with regular CEST for $B_1 = 1$ µT with corresponding numerical BM fit. The temperature is 310 K and the sample is 10 mM myo-inositol in a phosphate buffer.

Table 4.8: Estimated quantities with a 95% confidence interval for a sample of 10 mM myo-inositol in a phosphate buffer at 310 K, where T_1 of water was measured to be 4.28 s. * indicates that the estimation has reached a lower or upper bound.

SRD	k_{sw} (s^{-1})	$\Delta\omega$ (ppm)	T_{2s} (s)	T_{2w} (s)	T_{1s} (s)
200 ms	8727 ± 494	1.12 ± 0.04	0.63 ± 0.54	4.11 ± 0.86	2.33 ± 12
4.3 s	8089 ± 414	1.18 ± 0.04	1.09 ± 0.69	4.27 ± 0.89	2.00* ± 36
reg. CEST	2341 ± 796	0.70* ± 0.17	4.28* ± 5257	1.61 ± 0.57	2.00* ± 3630

a single spectrum is fitted for, prohibiting a solid, global solution. It is also possible that the low CEST contrast at 1 μT is too scarse to provide a good fit. Higher exchange rates tend to give better CEST contrast at higher B_1 [22]. Myo-inositol had an expected exchange rate of 2090 s^{-1} from [10], while the estimations of exchange rate here are approaching 8800 s^{-1}, indicating that a higher B_1 should have been attempted for the regular CEST.

An exchange rate of about 8400 s^{-1} and frequency offset 1.15 ppm gives[4] the relation

$$\frac{k_{sw}}{\Delta\omega \cdot 600.23\ \text{MHz}} = \frac{8400\ \text{s}^{-1}}{1.15 \cdot 600.23\ \text{Hz}} = 12.2, \tag{4.2}$$

indicating a fast intermediate exchange regime where the CEST contrast is low.

By visual examination of the residuals in Figure 4.14 the BM fitted curves appear to provide a good fit to the experimental spectra. The residuals are generally small, and besides the larger residuals at 0 ppm there is no peak of any sort standing out, which was the case for creatine. The lack of a distinct metabolite dip in the myo-inositol CEST spectra should be the reason for this.

The difference observed in the residuals of creatine between SRD = 200 ms and SRD = T_1 does not appear to be valid for myo-inositol. Here the change in residuals tend to show the same behaviour for SRD = 200 ms and SRD = T_1, although the residuals appear to be somewhat larger for SRD = 200 ms.

4.5.3 Glutamic acid

The sample of 10 mM glutamic acid was experimented on with six different saturation field strengths B_1: 1, 2, 3, 4, 5 and 8 μT. SR-CEST was run for SRD = 200 ms and SRD = T_1 = 4.4 s, in addition to a regular CEST sequence at B_1 = 5 μT for control. The exchange rate of glutamic acid was expected to be very high (~ 7000 [10]), which made a higher B_1

[4] Average exchange rate and frequency offset obtained for the global BM fitting of SR-CEST with SRD = 200 ms and SRD = 4.3 s.

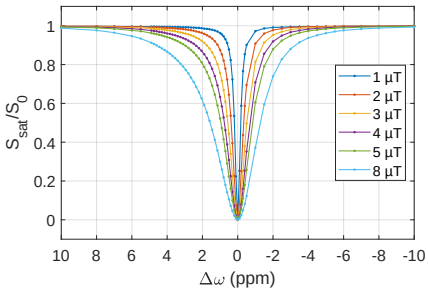

(a) SRD = 200 ms.

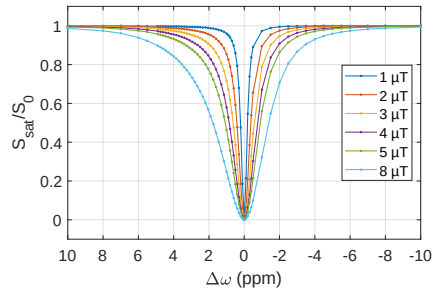

(b) SRD = T_1 = 4.4 s.

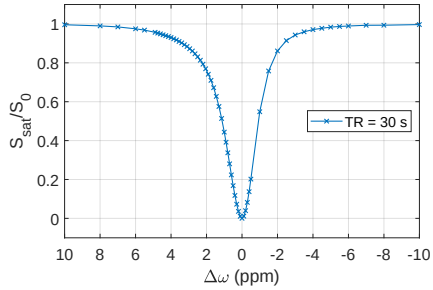

(c) Regular CEST with B_1 = 5 µT.

Figure 4.16: SR-CEST spectra generated with a) SRD = 200 ms and b) SRD = 4.4 s for varying B_1, and a regular CEST spectrum c) for B_1 = 5 µT. The temperature is 310 K and the sample is 10 mM glutamic acid in a phosphate buffer.

likely to give a better CEST contrast. All CEST spectra can be found in Figure 4.16.

As for the sample of myo-inositol there is no observable dip downfield, but by visually examining the spectra in Figure 4.16 there is a clear asymmetry around 0 ppm and the DS. It is strongest downfield, but even upfield the signal is more reduced than for the case of myo-inositol. This could indicate a stronger CEST effect from glutamic acid. This is remarkable: Myo-inositol was expected to have six labile protons at pH 7.4, whereas only three labile protons were expected for glutamic acid, suggesting higher CEST contrast for myo-inositol. An explanation to the more distinct CEST effect of glutamic acid could be in which time-scale the exchange is occuring (see Section 2.2.2). At the intermediate exchange regime the CEST contrast has been known to become imperceptible [19]. As the CEST contrast depends on both exchange rate and CEST agent concentration the three labile protons of glutamic acid can be situated at conditions more favourable of CEST contrast.

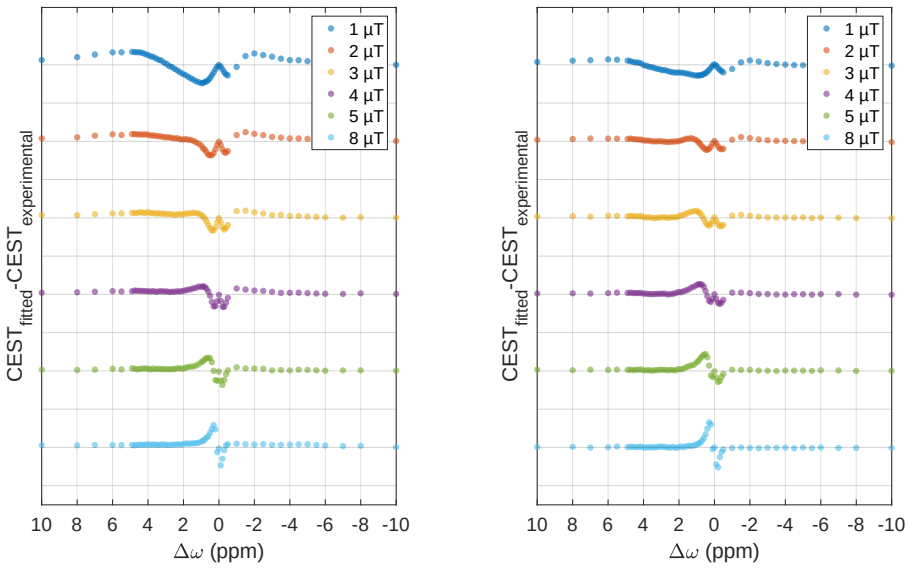

(a) SR-CEST with SRD = 200 ms.

(b) SR-CEST with SRD = 4.4 s.

Figure 4.17: The difference between the BM fitted and experimental CEST spectra as a function of offset frequency. All residual plots are aligned around 0 signal difference on the y-axis, and the difference between two horizontal lines is 0.05, or 5% of the normalized CEST spectra. Each residual plot represents an experiment conducted for a certain saturation field strength B_1, where a) shows residual plots for six different B_1 obtained with SRD = 200 ms, and b) shows six residual plots obtained with SRD = 4.4 s. A positive residual indicates that the amplitude of the fit is too small, giving a lesser CEST dip than what is experimentally obtained. The temperature is 310 K and the sample is 10 mM glutamic acid in a phosphate buffer.

4.5.3.1 Numerical BM fitting of glutamic acid CEST spectra

The spectra obtained for each SRD were BM fitted simultaneously, while only the single regular CEST spectrum took part in the regular fitting. The differences between the BM fitted and experimental SR-CEST spectra can be found in Figure 4.17, while the BM fitted regular CEST spectrum for $B_1 = 5$ µT is in Figure 4.18. All fitted spectra can be found in Appendix D.7. The estimated parameters for each global or single fit can be seen in Table 4.9.

The BM fitted spectra appear to provide a good fit to the experimental spectra, with the overall smallest residuals for SRD = 4.4 s.

The expected exchange rate for glutamic acid, as obtained in [10], was about 7000 s^{-1}. In this fitting the exchange rate seems to be situated about 13700 s^{-1}, but with exceptionally large 95% confidence intervals. As before, the relaxation time parameters

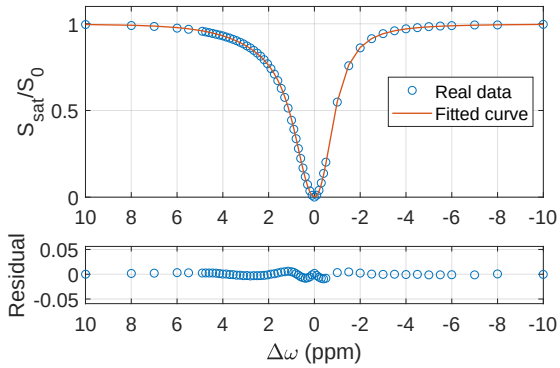

Figure 4.18: CEST spectrum generated with regular CEST for $B_1 = 5$ μT with corresponding numerical BM fit. The temperature is 310 K and the sample is 10 mM glutamic acid in a phosphate buffer.

Table 4.9: Estimated quantities with a 95% confidence interval in a sample of 10 mM glutamic acid in a phosphate buffer at 310 K, where T_1 of water was measured to be 4.39 s. * indicates that the estimation has reached a lower or upper bound.

SRD	k_{sw} (s^{-1})	$\Delta\omega$ (ppm)	T_{2s} (s)	T_{2w} (s)	T_{1s} (s)
200 ms	13444 ± 894	2.77 ± 0.13	0.58 ± 0.31	2.07 ± 0.38	2.01 ± 6
4.4 s	14064 ± 674	3.11 ± 0.11	3.87 ± 4.50	1.77 ± 0.18	2.44 ± 20
reg. CEST	12779 ± 1661	3.03 ± 0.30	0.41 ± 130	1.50 ± 0.22	2.00* ± 243

varies, making a conclusion about them challenging. The offset frequency of glutamic acid is situated around 3 ppm, but deviates between the solutions. The 95% confidence intervals of $\Delta\omega$ are also relatively large, compared to $\Delta\omega$ found for the other metabolites.

An exchange rate of about 13700 s^{-1} and frequency offset 2.94 ppm gives[5] the relation

$$\frac{k_{sw}}{\Delta\omega \cdot 600.23 \text{ MHz}} = \frac{13700 \text{ s}^{-1}}{2.94 \cdot 600.23 \text{ Hz}} = 7.76, \tag{4.3}$$

indicating, like for myo-inositol, a fast intermediate exchange regime where the CEST contrast can be low.

The exchange rates of amine protons in glutamic acid at $\Delta\omega = 3$ ppm have been reported to be 1000, 6000 and 25 000 s^{-1} at pH = 6, 7 and 8 at room temperature [20]. As this work have been conducted on a pH 7.4, slightly higher than in [10], and at a temperature 12° higher than in [20], the high estimated exchange rate could still be in

[5] Average exchange rate and frequency offset obtained for the global BM fitting of SR-CEST with SRD = 200 ms and SRD = 4.4 s.

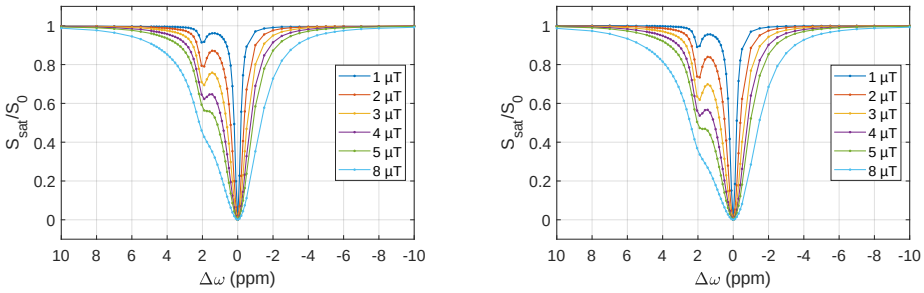

(a) SR-CEST with SRD = 200 ms.

(b) Regular CEST.

Figure 4.19: SR-CEST spectra generated with a) SRD = 200 ms and b) regular CEST for varying B_1. The temperature is 310 K and the sample is 10 mM creatine and 10 mM glutamic acid in a phosphate buffer.

agreement with other literature.

4.5.4 Creatine and glutamic acid

After experimenting on only single solutes in solution, a mix of 10 mM creatine and 10 mM glutamic acid was experimented on. One of the strengths of the BM fitting is its ability to separate different CEST effects from each other in addition to the direct saturation of water. The experiments on the mixed sample were run for SR-CEST with SRD = 200 ms and regular CEST, all with the six saturation field strengths B_1: 1, 2, 3, 4, 5 and 8 µT. The experimentally obtained spectra can be found in Figures 4.19a) and 4.19b).

The creatine dip in these experiments appears by visual examination more well-defined than for the experiments with 10 mM creatine. The width of the dip is approximately the same, but the amplitude is clearly greater. The glutamic acid in the sample is expected to affect the appearance of the creatine dip by adding a contribution from the wide glutamic acid peak to the amplitude, but the profound change in the dip indicates different physical properties of creatine in this sample.

4.5.4.1 Numerical BM fitting of creatine and glutamic acid CEST spectra

The BM fitting was executed simultaneously for the batch of SR-CEST experiments and batch of regular experiments, giving out a global solution for each batch. The plotted differences between the BM fitted and experimental CEST spectra can be found in Figure 4.20, with corresponding estimated parameters in Tables 4.10 and 4.11. All fitted spectra can be found in Appendix D.8

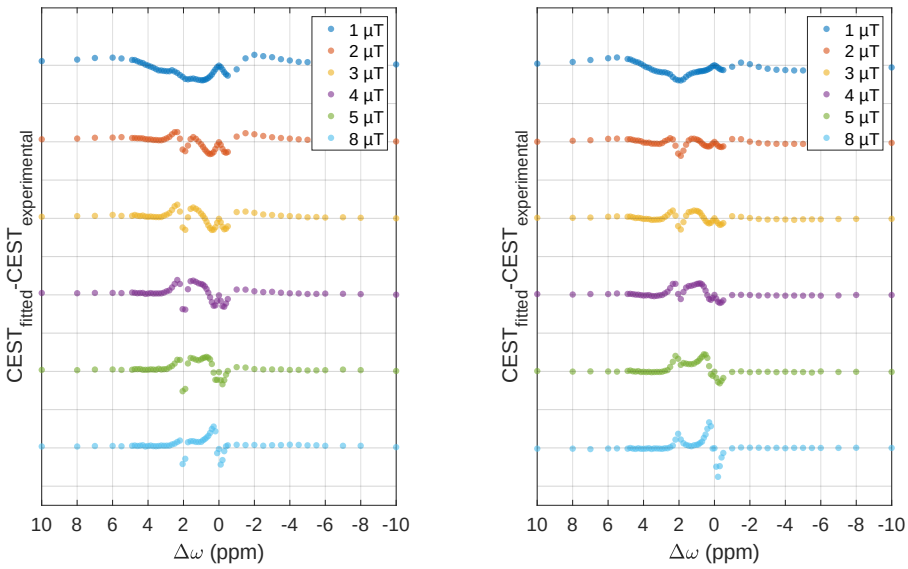

(a) SR-CEST with SRD = 200 ms.

(b) Regular CEST.

Figure 4.20: The difference between the BM fitted and experimental CEST spectra as a function of offset frequency. All residual plots are aligned around 0 signal difference on the y-axis, and the difference between two horizontal lines is 0.05, or 5% of the normalized CEST spectra. Each residual plot represents an experiment conducted for a certain saturation field strength B_1, where a) shows residual plots for six different B_1 obtained with SRD = 200 ms, and b) shows six residual plots obtained with regular CEST. A positive residual indicates that the amplitude of the fit is too small, giving a lesser CEST dip than what is experimentally obtained. The temperature is 310 K and the sample is 10 mM creatine and 10 mM glutamic acid in a phosphate buffer.

The residuals are nicely aligned around 0 signal difference, and the residuals of the regular CEST are generally smaller than for SR-CEST with SRD = 200 ms. The largest residuals are found between and about DS at 0 ppm and the creatine dip at 2 ppm for the different experiments.

Table 4.10: Estimated quantities in a sample with 10.0 mM creatine and 10 mM glutamic acid, done with SR-CEST with SRD = 200 ms. The temperature is 310 K, and T_1 of water is measured to be 4.31 s. * indicates that the estimation has reached a lower or upper bound.

Parameter	Unit	Creatine	Glutamic acid
k_{sw}	(s^{-1})	416 ± 20	12983 ± 989
$\Delta\omega$	(ppm)	2.00 ± 0.01	2.98 ± 0.13
T_{1s}	(s)	2.19 ± 1.20	2.10 ± 2.05
T_{2s}	(s)	2.17 ± 2.03	3.59 ± 1.16
T_{2w}	(s)	2.05 ± 0.37	

Table 4.11: Estimated quantities in a sample with 10.0 mM creatine and 10 mM glutamic acid, done with regular CEST. The temperature is 310 K, and T_1 of water is measured to be 4.31 s. * indicates that the estimation has reached a lower or upper bound.

Parameter	Unit	Creatine	Glutamic acid
k_{sw}	(s^{-1})	691 ± 44	11255 ± 1019
$\Delta\omega$	(ppm)	1.99 ± 0.01	2.97 ± 0.12
T_{1s}	(s)	4.31^* ± 204	2.00^* ± 120
T_{2s}	(s)	0.40^* ± 7	4.04 ± 220
T_{2w}	(s)	1.22 ± 0.14	

The exchange rate of creatine has had a significant decrease in comparison to the experiments done for 10 mM creatine in the same buffer environment and temperature. This is in agreement with the different appearances of the creatine dips between these two experiments, given the effect the exchange rate has on the appearance of spectra described in Section 2.2.2. The exchange rate of glutamic acid appears somewhat slower, but is roughly in the same region as what was obtained in Section 4.5.3. There is some variation between the estimated parameters from the SR-CEST and the regular CEST experiment. The estimated exchange rate for creatine increased by more than 200 s^{-1} from SR-CEST to regular CEST, while the exchange rate of glutamic acid shows opposite development. The offset frequencies $\Delta\omega$ are estimated to be the same for SR-CEST and regular CEST for both creatine and glutamic acid, whereas it still is difficult to make a statement about the relaxation time parameters.

Chapter 5

Discussion

There are three main points to discuss in this thesis work: The use of the proposed SR-CEST sequence, the characterization of the different metabolites, and the models used in the numerical fitting.

5.1 The spoiler recovery CEST approach

The new SR-CEST sequence, which is a combination of the spoiler recovery approach with short spoiler recovery delays (SRD) and the regular CEST experiment, can reduce the total scan time for an experiment by more than 70%, without any significant reduction of signal to noise ratio: The CEST dips in the spectra from SR-CEST with short SRD had smaller amplitudes, but these changes were taken account for in the numerical BM fitting. In this way the spoiler recovery approach produced less CEST contrast, but without conflicting with the numerical analysis. Although the initial conditions for the experiment is severly altered between regular CEST and SR-CEST, the analysis of SR-CEST and regular CEST spectra yield overall the same information. Both SR-CEST with SRD = T_1 and SRD = 200 ms, and regular CEST, tended to give similar estimations for exchange rate and offset frequency for the different metabolites. The most substantial exception was the BM fitting of the regular CEST spectrum obtained for myo-inositol at 310 K and B_1 = 1 μT, where a weak CEST contrast in these conditions was suggested as explanation.

In order to test the SR-CEST sequence SR-CEST spectra were generated for a sample of 47.5 mM creatine in a phosphate buffer, with varying SRD. Creatine is a good test subject as it has a distinct CEST dip at 2 ppm, well separated from the direct saturation of water at 0 ppm, and thus generate high CEST contrast. In the numerical BM fitting increasing

residuals around 2 ppm was observed with increasing SRD. This is presumably a problem intrinsic to the fitting, and not originating in the SR-CEST sequence itself. It will therefore be thoroughly discussed in Section 5.3.

In conclusion, the spoiler recovery approach should be applied when generating CEST spectra, as it reduces the acquisition time significantly. Choosing a short SRD enables faster acquisition times, but if a higher CEST contrast is needed, a longer SRD could be considered. An alternative to use longer SRDs is running experiments with short SRDs with several number of scans, likely to improve the CEST contrast more over the same time range. The value of 200 ms was chosen as a repeatable SRD in this work to ensure that any potential eddy currents originating in the gradient spoiling had time to attenuate to an insignificant level. This was a mere safeguard, and it is plausible that a shorter SRD would give just as good results. This should be investigated in further work.

5.2 CEST of different metabolites

In this work CEST and SR-CEST spectra of creatine, myo-inositol and glutamic acid have been obtained and analyzed. Creatine had a clearly visible dip in the CEST spectrum around 2 ppm, and was the easiest metabolite to detect visually. The CEST spectra for both myo-inositol, with estimated offset frequency around 1.2 ppm, and glutamic acid, with estimated offset frequency around 3.0 ppm, had no apparent dips. The only indication of a CEST effect being present in the myo-inositol and glutamic acid CEST spectra was a slight asymmetry around the direct saturation of water (DS). This is similar to what has been found by others (at pH 7.4 with field strengths 3 T and 7 T and higher metabolite concentrations) [12]. Although appearing similar by visual examination, the asymmetry was enough for the numerical BM fit to separate the metabolites by obtaining estimates that concurred over varying saturation field strengths B_1 and CEST sequences: The forward exchange rate k_{sw} and frequency offset from water $\Delta\omega$ was possible to estimate for all metabolites. The estimations across the same samples with varying CEST sequences were overall within, or almost within, the same 95% confidence interval for k_{sw} and $\Delta\omega$, but with a few exceptions. However, the 95% confidence interval of the relaxation time parameters was too large to make a reliable statement about $T_{2\mathrm{s}}$ and $T_{1\mathrm{s}}$. An estimate of $T_{2\mathrm{w}}$, which was expected to be close to the $T_{1\mathrm{w}}$ measured by saturation recovery, was reliably obtained in some cases, but also this parameter had tendencies to vary greatly. This is why exchange rate and offset frequency should be considered the most important parameters to extract from the numerical BM fitting. With metabolite concentrations and $T_{1\mathrm{w}}$ kept fixed, these are the variables with most impact on the appearance of the CEST

spectra, and therefore the parameters most convenient to fit.

To find reliable estimates of k_{sw} and $\Delta\omega$ a series of CEST spectra generated with different parameters should be fitted simultaneously to gain a global solution, instead of fitting a single CEST spectrum [10]. The parameters to vary could be B_1 and saturation time t_{sat}, but also parameters from the metabolite solution, such as pH and metabolite concentration. The parameters k_{sw} and $\Delta\omega$ are independent of metabolite concentration [21], and running a simultaneous fit over varying metabolite concentrations should be attempted. As an alternative to the simultaneous fitting, each spectrum could have been BM fitted separately. This would yield varying estimates for k_{sw}, $\Delta\omega$, T_{1s}, T_{1w} and T_{2w}, and an average with standard deviation should be obtained for the variables of interest. This approach is likely to give fits with smaller residuals, but larger insecurity in the estimates of k_{sw} and $\Delta\omega$. As a true solution ought to be valid across varying B_1 the simultaneous approach to the fitting has been deemed the best.

In this work CEST spectra generated with a series of B_1 have been fitted simultaneously, giving a single solution for all spectra generated for a sample with a specific CEST sequence. Residuals up to 5% of the normalized CEST spectrum were observed, indicating that a perfect fit across all B_1 is challenging. The varying results could simply be that it is difficult to obtain a perfect description of a real physical system, but it could also indicate that a larger number of spectra is required to achieve a reliable fit.

Characterizing CEST agents in samples with only one CEST agent present is considered easy, as compared to a more complex blend of several metabolites or substances that undergo CEST. Other studies have for instance shown that CEST can detect cancer aggressiveness and response to chemotherapy in water-soluble extracts of breast cell lines. These cancer models contain more than one CEST metabolite [7]. The numerical model is depending on suitable boundary values [9], and with several metabolites in one sample, the boundary values are believed to become even more important. By knowing which frequency offset and chemical exchange rate to expect for the CEST agents present, one is more likely to succeed with a numerical fit.

The numerical BM fitting can also estimate the concentration of the CEST agents, by using their concentration as a parameter free to vary. Both exchange rate and concentration of the agents have great impact on the size of the CEST dip, which could make their effects difficult to distinguish. A larger amount of parameters to fit also makes the fitting more challenging, as it opens up for a larger amount of possible, yet unreal, solutions. By knowing which exchange rate to expect a more reasonable estimate of concentration can be obtained for samples with unknown concentrations. The experiments of single solute metabolites conducted here can be utilized for this, by providing expected exchange

rate and frequency offset for the different metabolites. The solutions obtained here and in similar experiments could even be applied as fixed parameters in BM fittings of unknown samples. In order to do this, more experiments should be conducted to reduce the uncertainty in the estimated parameters.

In Section 4.5.4 CEST spectra acquired with a mix of 10 mM creatine and 10 mM glutamic acid in a 37.5 mM phosphate buffer at 310 K was analyzed. The numerical BM fitting enabled separation of the two metabolites by estimating distinguishable exchange rates and offset frequencies. While the estimations obtained for glutamic acid agreed with the estimations obtained for a sample with glutamic acid only (Section 4.5.3), the estimations for creatine were significantly slower than what was obtained with creatine only (Section 4.5.1). It appears as if the physical properties of creatine is altered with the presence of glutamic acid. Being an acid, it is possible that glutamic acid lowers the pH of the sample, giving a slower exchange rate of creatine, although the phosphate buffer should counteract this. In further work it should be investigated whether this is a weakness in the numerical BM fitting, or whether the conditions really change with the presence of glutamic acid. It is indispensable that the model succeeds in curve fitting CEST spectra with multiple pools of CEST agents for it to have further applicability. Experiments on more samples consisting of multiple metabolites should ideally be conducted.

5.3 Numerical BM fitting

The common approach to analyze CEST spectra have been MTR_{asym}-analysis [2]. By applying the numerical BM fitting effects concomitant to CEST that otherwise would interfere with the MTR_{asym}-analysis can be taken into account. In addition, separation of the various contribution to the CEST effect is enabled, such as metabolite concentration and exchange rate [18].

There are two main challenges in the numerical BM fitting: The uncertainty in the estimated parameters, and the apparent underestimation seen for the amplitude of the creatine dip. In the test of the spoiler recovery approach in Section 4.3, the numerical BM fitting tended to give a too low amplitude of the creatine CEST dip. The exception was for short SRDs, where the fit was found to be quite accurate. It is possible that also the CEST dips of myo-inositol and glutamic acid are underestimated in the experiments concerning these, but that the shape and size of the spectra makes the difference imperceptible.

When performing the numerical BM fitting, concentration and exchange rate have a great impact on the amplitude and shape of the dips of the CEST agents. The estimates of the exchange rates obtained here were overall high compared to what was obtained by

others [10]. If there is a broadening effect present in the CEST spectra, this would also change the estimate of exchange rate: Considering the estimations obtained for a sample containing creatine at 298.1 K, an exchange rate of 750 s^{-1} and offset frequency 1.93 ppm gives a relation of

$$\frac{k_{sw}}{\Delta\omega \cdot 600.23\ \text{MHz}} = \frac{750\ s^{-1}}{1.93 \cdot 600.23\ \text{Hz}} = 0.65, \tag{5.1}$$

which indicates an intermediate exchange regime (see Section 2.2.2). A broadening of the CEST dip will therefore give a higher estimated exchange rate, while a narrower CEST dip yields a lower estimated exchange rate. Considering the BM simulation of the creatine CEST spectra, a lower exchange rate of creatine should give a larger amplitude of the creatine dip, possibly mending the gap between the estimated and experimental spectra. This could indicate that there are effects disturbing the creation of CEST spectra, making them broader than theoretically expected.

In the following sections suggested explanations for this misfit and the uncertainty in the estimated parameters is discussed, as well as potential amends.

5.3.1 T_1 of water

In the numerical BM fitting T_1 of water has been kept a constant, which was measured for all samples at all temperatures using the saturation recovery method. The T_1 values were estimated with a mono-exponential fit of the water peak signal after multiple saturation recovery times.

This build-up curve is usually approximately exponential [1, p. 32], but the assumption of a mono-exponential curve fitting is not always valid. For instance, the presence of bi-exponential T_1 relaxation in tissues such as muscle, cartilage, gray matter and white matter has been acknowledged for some time [23]. Rioux *et al.* introduces an apparent T_1, called T_1^*, that is composed by a short component ($\ll T_1$) and a longer component ($> T_1$). They argue that, using inversion recovery experiments as example (see for instance [1, Ch. 12.1]), a short inversion time (TI) yield an increased dependency on the short T_1-component. As TI increases and becomes much greater than the value of the short T_1-component, the short component no longer contributes to signal change during the acquisition. In that case, to good approximation, T_1^* becomes equal to the long T_1 component, and it becomes valid to use a mono-exponential model [23].

SR-CEST is not an inversion recovery experiment, and has no TI-variable. In this work it has also been performed on aqueous solutions, and not on tissue samples. Still, it is possible that the assumption of a mono-exponential fit becomes less valid when

operating with short SRDs, such as SRD = 200 ms. The bi-exponential behaviour of T_1 is also known to be more prominent at higher fields [23], which 14.1 T certainly is. It should be noted that in addition to the possibility of a bi-exponential behaviour, the longitudinal relaxation time has been known to be composed of a larger number of T_1s [24], being a so-called T_1 distribution. In Section 4.3 short SRDs provided a good BM fitting, whereas the CEST peak was more and more underestimated with longer SRD. It is possible that a shorter T_1-component of water has been predominating for the shorter SRDs, giving more relaxation (and hence more saturation) than expected. This could also explain the differences seen between numerical BM fittings conducted for CEST spectra of varying metabolite samples created with SRD = 200 ms and SRD = T_1, and between SRD = 200 ms and regular CEST.

Using a higher T_1 of water for the higher SRDs would also yield a better fit[1], indicating that the predominant T_1 of water could vary between SR-CEST experiments, and should be changed between experiments. T_1 of water is one of the parameters with most impact on the shape of the CEST spectra, and should be possible to estimate. The argument of using a fixed T_{1w} is the already vast number free of parameters to be fitted for. T_{1w} is one of the parameters most accessible to be measured in the samples, and was therefore set as constant.

5.3.2 Labile protons

All metabolites in this work have several protons labile for chemical exchange. Creatine was expected to have four, myo-inositol six, and glutamic acid three [10]. Different sites in molecules and different molecule structures may give protons different properties, such as exchange rate, offset frequency, T_1 and T_2. In the numerical BM fittings all labile protons were expected to have the same physical characteristics. This was an approximation, which was made because the differences of the physical characteristics between the labile protons were assumed small [10]. What is visible in the CEST spectra is thus an average over the labile proton population, and the differences between labile protons has to be negligible to obtain a good fit.

The pH dependence of the number of labile protons n_s in creatine has been investigated by others [20] who found an average value of $n_s = (3.92 \pm 0.33)$ at pH = 6.4 and T = 21°C. Creatine is expected to deprotonate with higher pH and temperature. As this work has been conducted at pH 7.4 with temperatures 298.1 K or 310 K different degrees of deprotonation should be expected. This indicates that the constant $n_s = 4$ could need

[1] This was tested by varying T_{1w} in the numerical BM fitting, where longer T_{1w}s gave smaller residuals for long SRDs.

modification to a lower value, which would create an even larger deviation between the amplitude of the estimated creatine dip and the experimentally obtained dip.[2]

Considering this, a numerical solution with a pool for each labile proton could have been attempted for. This was not done for several reasons: Firstly, CEST is an effect intended for MRI, where several CEST agents will be present. Assigning all labile protons with a unique pool would result in a vast number of pools. This would both make the numerical solution more time consuming, and increase the uncertainty in the estimated parameters: As the numerical solution gains more variables, it also gains more possible solutions. This means a higher probability of finding an inaccurate solution. Secondly, the assumption of identical pools is in many cases acceptable. The cumbersome implementation of multiple pools in the numerical BM fitting does not have to be necessary, and is best left out.

5.3.3 Radiation damping

Radiation damping (RD) is known to disturb NMR experiments such as relaxation measurements and two-dimensional spectroscopy, but can also give rise to unexpected effects in CEST spectroscopy [17].

Williamson *et al.* argues that the RD narrows the CEST spectrum [17]. The narrowing occurs because the secondary RF field induced by the rotating transverse magnetization opposes the effects of the applied B_1 saturation field. This, they argue, reduces the effective RF amplitude. In this work the applied RF saturation field was assumed to be of a strength too low to generate RD. A narrower CEST spectrum is also expected to yield better fittings than those obtained here, indicating that the narrowing effect from RD during saturation is minimal.

In comparison to the saturation field strength of 5 μT, the RF excitation pulse of 587 μT is significantly stronger. To avoid radiation damping (RD), an excitation pulse of only 10° was applied at the end of the CEST sequences. Still, the CEST spectra has been acquired with aqueous solutions at very high magnetic field, both implicating a higher damping field (see Section 2.1.6). Generally the water signal peak observed in the Fourier transformed FID of the different samples was remarkably wide, indicating shorter transverse relaxation times than $T_2 \approx T_1$. This is typically a result of RD, implying that the phenomenon is present.

For the regular CEST experiments there are no hard RF pulses that are expected to generate RD before the read pulse. This means that although there are indications of

[2] A lower n_s give fewer protons to create the CEST effect in the numerical BM fitting. This yields a smaller amplitude for the estimated CEST dip.

shorter relaxation times due to radiation damping *after* the excitation pulse, this is not the case *before* the excitation pulse. This is where the system is simulated, and RD should not have any impact during the simulating period. RD will give the water signal peak a shorter amplitude and a longer width, but as it is the integral over all of the water signal that is used to generate the CEST spectra this should be of low impact.

For SR-CEST, there are two hard pulses applied before the regular CEST sequence; the two 90°-pulses applied with subsequent spoiler gradients. These pulses spoil the net magnetization in the sample, resulting in no transverse magnetization to generate a damping field. RD will therefore also here presumably have no impact before the excitation pulse.

Although radiation damping is not expected to interfere with the system during saturation, the phenomenon could affect the appearance of the CEST spectrum. At the frequency offset $\Delta\omega = 0$ the water protons themselves are saturated, giving a net nuclear magnetization assumed to be 0. As one is stepping away from the direct saturation of water protons, the net nuclear magnetization of the sample increases. This increase in magnetization could give rise to an increasing radiation damping effect, gradually altering the spectrum with changing $\Delta\omega$. This would give most RD at the edges of the spectrum, where S_0 is obtained to normalize the spectrum, and least RD at 0 ppm, which again would yield a narrower spectrum.

Several methods to control radiation damping effects using both hardware and software modifications exists [16]. The simplest simplest way to minimize the effect of RD is to reduce the flip angle of the excitation pulse. There are also more sophisticated methods, such as including RD in the Bloch equations that describe the system [16]. In many NMR experiments where RD is present the water protons are saturated to reduce RD, but this is not suitable for CEST experiments where the signal from water protons is being measured. Including RD in the numerical fitting could be attempted, but the approach is complex [16] and likely to yield time consuming fittings. Using a spectrometer with lower field strength would reduce the radiation damping [16], and could indicate to which extent radiation damping is interfering with the signal. A further reduction of the flip angle of the excitation pulse should also be attempted in further work. Another possible way of reducing RD is applying SR-CEST with short SRDs in the millisecond range. This prohibits parts of the net nuclear magnetization to return to thermal equilibrium before the excitation pulse, suppressing the bulk water proton signal. In fact, short SRDs combined with short saturation times can significantly reduce the bulk water proton signal.

5.3.4 T_2 of water

One of the variables used in the numerical BM fitting was T_2 of both water and metabolites. As mentioned previously, the numerical fitting takes advantage in having few parameters and more constants. This is why the longitudinal relaxation time T_1 of water was measured. Measuring T_2 of water, T_{2w}, has proven to be challenging: Carr–Purcell–Meiboom–Gill (CPMG) is a method consisting of a series of spin echoes often used to measure T_2 [1, Ch. 12.2]. When applying CPMG to a system undergoing chemical exchange, the decay measured is expected to be a sum of several exponential terms [25]. The BM simulation requires the T_{2w} unperturbed by chemical exchange, and another approach than CPMG is thus needed. Alternatively, the CPMG could be applied on a similar sample without CEST agents present, such as a sample with phosphate buffer only. This is requires that the presence of the different metabolites do not alter T_{2w} significantly. Among the samples containing 10 mM metabolites, the largest variation in T_1 of water was 0.21 s, justifying this assumption.

For complex samples with several metabolites or *in vivo* application of the CEST and SR-CEST sequences, creating an environment with no chemical exchange to execute CPMG on becomes challenging. This, combined with the uncertainty in the method of measurement, makes it more practical to use T_2 of water as a parameter free to vary.

5.3.5 Ideal B_1

Although large values of B_1 enable the highest degree of saturation of solute protons, the use of a large B_1 value can obscure the true CEST effect [26]. Due to the competition of RF saturation and spillover effects, there is an optimal RF irradiation power that maximizes the CEST contrast. This power varies with both exchange rate and labile proton frequency. For labile protons well separated from the bulk water resonance, the spillover effects should be negligible and the optimal RF power has been postulated to be approximately equal to the chemical exchange rate [22].

For creatine the exchange rate was measured to be approximately 2000 Hz at 310 K, with an offset frequency of about 1.9 ppm. An RF power of 2000 Hz on a 600.23 MHz spectrometer yields an ideal B_1 power of about 3 μT, given sufficient separation from the bulk water resonance. The offset frequency of glutamic acid was indeed estimated to be about 3 ppm, but due to the large width of the glutamic acid dip the spillover effects cannot be neglected. Also for myo-inositol with an offset frequency about 1.2 ppm from bulk water the spillover effects are assumed to be too large to neglect, and the optimal RF saturation power cannot be approximated with this method.

By conducting CEST experiments at B_1 values closer to the ideal B_1, the numerical BM

fitting is likely to be improved because of increased CEST contrast. Instead of choosing a range of B_1 from 1 to 8 μT for the creatine CEST experiments at 310 K, a series of B_1 closer to the ideal B_1 should be considered. B_1-values of, for instance, 2.5, 2.75, 3, 3.25 and 3.5 μT could have been attempted, as these values are likely to give more CEST contrast, giving more prominent CEST data to fit for. It is more challenging to suggest ideal values of B_1 for glutamic acid and myo-inositol. Glutamic acid is likely to require a higher B_1 value because of the high exchange rate [10], but the same indication cannot be made for myo-inositol, due to the closeness to bulk water resonance.

To find the ideal B_1 values and thus optimize CEST contrast, more experiments should be conducted. Combined with an ideal B_1 the ideal saturation time t_{sat} should also be investigated. This variable has been kept fixed throughout this work, but others have proved that varying t_{sat} can improve CEST contrast [10].

5.3.6 D_2O

All samples contained 10% D_2O, but the numerical BM fitting assumed 100% H_2O. With 10% deuteration of the bulk water, 10% of the exchanging sites will contain the deuterium isotope. This means that molecules with multiple exchanging sites have many ways of combining the isotope labelling. The chemical shift of a spin in a particular nuclear site is known to depend slightly on the nuclear isotopes in neighbouring nuclear sites [1, Ch. 9.1]. The presence of deuterium close to exchanging sites could therefore have some impact on the chemical shift of the labile protons. An isotopic effect on the exchange rate could also be expected. In theory each of these combinations could have been treated as separate pools in the BM model, but the number of pools would be excessive. In other work coaxial inserts with D_2O and sample in respectively outer and inner tube have been employed [10], and others again have performed CEST experiments without the deuterium lock [12]. The deuterium lock was here considered indispensable to keep the spectrometer operating at a constant net magnetic field. Using coaxial inserts for samples similar to the ones used in this work can indicate to which extent the presence of D_2O is interfering with the CEST effect, and should be attempted in further work.

5.4 Further work

CEST as a contrast mechanism have most utility for *in vivo* MRI and MRS, and not in the spectrometer setting of this work. This is because the low concentration metabolites is usually clearly visible in high field NMR spectra. *In vivo*, however, MRS is insensitive and only high concentration metabolites are visible [18]. CEST MRI enables identification of

some of the low concentration metabolites, but to enable a similar numerical BM fitting as in this work for CEST spectra aquired *in vivo* there are several considerations to be made.

To run a numerical BM fit on spectra generated for CEST agents with low concentration (< 10 mM), as expected *in vivo*, acquiring CEST spectra with several number of scans (NS) should be considered. The SR-CEST approach has proven to save a significant amount of time, which could be spent on several NS. As the spoiler recovery approach is spoiling the magnetization uniformly in space (see Section 2.3), this should not interfere with the image acquisition. To run a numerical BM fit on SR-CEST spectra generated with multiple NS, the impact of NS on the spectra must be taken into account.

Another method to achieve fast CEST spectral acquisition has been adopted recently in CEST spectroscopy [27]. This method simultaneously applies RF irradiation and a gradient along a direction in which the sample is considered to be homogeneous, which enables collecting all offset frequencies in a single acquisition [27]. This combined with the spoiler recovery approach can drastically reduce the acquisition time of a series of CEST spectra, enabling CEST spectra with enough data points to conduct numerical BM fitting *in vivo* or facilitating multiple NS.

Based on the results of the current work the CEST sequence itself could be further optimized. The expected chemical shift $\Delta\omega$ found for the different metabolites can be utilized in better selecting which offset frequencies to use in generating the CEST spectra. The metabolites considered here are for instance expected to be found for $\Delta\omega < 4$ ppm, suggesting that the spectra could go from -5 ppm to 5 ppm, instead of -10 ppm to 10 ppm. With the same density of offset frequencies, this would yield a CEST experiment with fewer offset frequencies, giving a shorter acquisition time. The reduction in the acquisition time should be weighted up against a higher uncertainty in the numerical BM fit caused by fewer data points to fit.

By optimizing the CEST sequence as described, different low concentration metabolites can likely be characterized with CEST and numerical BM fitting performed *in vivo*. As a start, the sequence should be tested on samples containing more CEST visible metabolites. This could, for instance, be cell extracts or organiods; cell cultures grown in three dimensions and used as models for human organs. If this approach succeeds in estimating the exchange rate of CEST agents with a satisfactory certainty, the numerical BM fitting can be applied in the clinic. Studies have for instance demonstrated that the intracellular pH of solid tumors is maintained within a range of 7.0–7.2, whereas the extracellular pH is acidic [3]. In general, the exchange rate is slower at a low pH than at a high pH because of base catalysis of proton exchange [3]. Thus a change in pH can be determined by measuring exchange rates. Metabolite concentrations of glutamic acid, myo-inositol

and creatine have also shown to decrease with increasing breast cancer aggressiveness [7], giving metabolite concentration as another parameter of interest to gain from the BM fitting.

Chapter 6

Conclusion

Chemical exchange saturation transfer (CEST) is known to substantially enhance sensitivity in NMR imaging and spectroscopy by increasing the contrast from dilute labile protons of low concentrations. The CEST effect is sensitive to the concentration and exchange rate of the labile protons, and therefore also parameters that affect the exchange rate, such as pH and temperature. In this work a new sequence, the SR-CEST, has been developed. It was successfully implemented and tested using aquaeous samples, and yielded the same results as the regular CEST sequence. The SR-CEST sequence significantly reduces the acquisition time, thus making the CEST experiment more applicable. The CEST spectra have been least square curve fitted with the Bloch-McConnell equations, providing estimates for the exchange rate and offset frequency. Knowing the exact exchange rate of relevant metabolites at selected pH and temperatures increases the possibility of determining the CEST agent concentrations. Changes in exchange rate can also be exploited as inherent biomarkers for detection of disease and monitoring the effects of treatment. Among the weaknesses of the numerical BM fitting was a distinct deviation between the estimated and experimental creatine dip in the creatine CEST spectra. This could be explained by a multi-exponential T_1 distribution, but radiation damping, averaging over labile protons and the unaccounted presence of 10% D_2O in the samples have also been discussed as possible explanations. The exchange rates found were overall higher than what was observed by others. Reasons for this were discussed, where varying sample compositions and experimental conditions was the most prominent explanation. In further experiments where long repetition times are required between each offset frequency scan, SR-CEST should be used to reduce acquisition times significantly. SR-CEST is also a promising tool for *in vivo* CEST MRI, which should be further investigated.

Bibliography

1. Levitt, M. H. *Spin dynamics: basics of nuclear magnetic resonance* (Wiley, 2008).

2. Van Zijl, P. C. & Yadav, N. N. Chemical exchange saturation transfer (CEST): what is in a name and what isn't? *Magnetic resonance in medicine* **65,** 927–948 (2011).

3. Zhang, X., Lin, Y. & Gillies, R. J. Tumor pH and its measurement. *Journal of Nuclear Medicine* **51,** 1167–1170 (2010).

4. López-Villegas, D., Kimura, H., Tunlayadechanont, S. & Lenkinski, R. E. High spatial resolution MRI and proton MRS of human frontal cortex. *NMR in Biomedicine: An International Journal Devoted to the Development and Application of Magnetic Resonance In Vivo* **9,** 297–304 (1996).

5. Kim, J., Wu, Y., Guo, Y., Zheng, H. & Sun, P. Z. A review of optimization and quantification techniques for chemical exchange saturation transfer MRI toward sensitive in vivo imaging. *Contrast media & molecular imaging* **10,** 163–178 (2015).

6. Jones, K. M., Pollard, A. C. & Pagel, M. D. Clinical applications of chemical exchange saturation transfer (CEST) MRI. *Journal of Magnetic Resonance Imaging* **47,** 11–27 (2018).

7. Chan, K. W. *et al.* CEST-MRI detects metabolite levels altered by breast cancer cell aggressiveness and chemotherapy response. *NMR in biomedicine* **29,** 806–816 (2016).

8. Goldenberg, J. M. & Pagel, M. D. Assessments of tumor metabolism with CEST MRI. *NMR in Biomedicine,* e3943 (2018).

9. Zhou, I. Y. *et al.* Quantitative chemical exchange saturation transfer (CEST) MRI of glioma using Image Downsampling Expedited Adaptive Least-squares (IDEAL) fitting. *Scientific reports* **7,** 84 (2017).

10. Khlebnikov, V., van der Kemp, W. J., Hoogduin, H., Klomp, D. W. & Prompers, J. J. Analysis of chemical exchange saturation transfer contributions from brain metabolites to the Z-spectra at various field strengths and pH. *Scientific reports* **9,** 1089 (2019).

11. Sørland, G. H. *Dynamic Pulsed-field-gradient NMR* (Springer, 2014).

12. Lee, J.-S., Xia, D., Jerschow, A. & Regatte, R. R. In vitro study of endogenous CEST agents at 3 T and 7 T. *Contrast media & molecular imaging* **11,** 4–14 (2016).

13. McConnell, H. M. Reaction rates by nuclear magnetic resonance. *The Journal of Chemical Physics* **28,** 430–431 (1958).

14. Zhou, J., Wilson, D. A., Sun, P. Z., Klaus, J. A. & Van Zijl, P. C. Quantitative description of proton exchange processes between water and endogenous and exogenous agents for WEX, CEST, and APT experiments. *Magnetic Resonance in Medicine: An Official Journal of the International Society for Magnetic Resonance in Medicine* **51,** 945–952 (2004).

15. Slichter, C. P. *Principles of Magnetic Resonance* 3rd ed. (Springer, 1992).

16. Krishnan, V. V. & Murali, N. Radiation damping in modern NMR experiments: progress and challenges. *Progress in nuclear magnetic resonance spectroscopy* **68,** 41 (2013).

17. Williamson, D. C., Närväinen, J., Hubbard, P. L., Kauppinen, R. A. & Morris, G. A. Effects of radiation damping on Z-spectra. *Journal of Magnetic Resonance* **183,** 203–212 (2006).

18. Zaiss, M. & Bachert, P. Chemical exchange saturation transfer (CEST) and MR Z-spectroscopy in vivo: a review of theoretical approaches and methods. *Physics in Medicine & Biology* **58,** R221 (2013).

19. Kleckner, I. R. & Foster, M. P. An introduction to NMR-based approaches for measuring protein dynamics. *Biochimica et Biophysica Acta (BBA)-Proteins and Proteomics* **1814,** 942–968 (2011).

20. Goerke, S., Zaiss, M. & Bachert, P. Characterization of creatine guanidinium proton exchange by water-exchange (WEX) spectroscopy for absolute-pH CEST imaging in vitro. *NMR in Biomedicine* **27,** 507–518 (2014).

21. Dixon, W. T. *et al.* A concentration-independent method to measure exchange rates in PARACEST agents. *Magnetic resonance in medicine* **63,** 625–632 (2010).

22. Sun, P. Z. & Sorensen, A. G. Imaging pH using the chemical exchange saturation transfer (CEST) MRI: correction of concomitant RF irradiation effects to quantify CEST MRI for chemical exchange rate and pH. *Magnetic Resonance in Medicine: An Official Journal of the International Society for Magnetic Resonance in Medicine* **60,** 390–397 (2008).

23. Rioux, J. A., Levesque, I. R. & Rutt, B. K. Biexponential longitudinal relaxation in white matter: characterization and impact on T1 mapping with IR-FSE and MP2RAGE. *Magnetic resonance in medicine* **75,** 2265–2277 (2016).

24. Komu, M., Alanen, A., Määttänen, H. & Kormano, M. Method dependence of proton spin-lattice relaxation analysis in biologic tissues. *Acta Radiologica* **30,** 97–100 (1989).

25. Allerhand, A. & Thiele, E. Analysis of Carr—Purcell spin-echo NMR experiments on multiple-spin systems. II. The effect of chemical exchange. *The Journal of Chemical Physics* **45,** 902–916 (1966).

26. Woessner, D. E., Zhang, S., Merritt, M. E. & Sherry, A. D. Numerical solution of the Bloch equations provides insights into the optimum design of PARACEST agents for MRI. *Magnetic Resonance in Medicine: An Official Journal of the International Society for Magnetic Resonance in Medicine* **53,** 790–799 (2005).

27. Zhou, I. Y. *et al.* Fast Tissue Characterization with Quantitative High Resolution Magic Angle Spinning (HRMAS) CEST Z-Spectroscopy. *Analytical chemistry* **88,** 10379 (2016).

Appendix A

Acquisition details

A.1 Sample details

Here follows a detailed description of how the samples used in the experimental work in this thesis have been made.

Table A.1 shows the measured quantities of the varying metabolites, and the final concentration of metabolite in each sample. In addition to the solutions in Table A.1 a sample with both glutamate and creatine was made. To make the sample of glutamate and creatine, 74.575 mg of creatine monohydrate was dissolved in 25 mL of the already prepared solution of 19.9 mM glutamate. It was then diluted with 25 mL buffer containing 75 mM phosphate. To gain samples of 10 mM metabolite concentration all the 20 mM solutions were further diluted with equal parts buffer containing 75 mM phosphate. The exception is the samples used in Section 4.4, where varying phosphate concentrations were tested. The buffer contained 20% D_2O, giving a net D_2O content of 10% in the samples. There is a more detailed description of the buffer in Section A.1.1.

Sample	Molecular weight (g/mol)	Measured quantity (g)	H_2O (mL)	Concentration (mM)
Myo-Inositol	180.16	0.1810	50	20.09
Glutamat	147.13	0.1467	50	19.93
Creatine	149.15	0.1487	50	19.94
Creatine	149.15	0.1862	25	49.94
Creatine	149.15	0.1343	10	90.04

Table A.1: Table of the measured quantities to make the varying metabolite samples. To gain 10 mM samples of the 20 mM samples they were further diluted with equal part sample solution and equal part 75 mM phosphate buffer. The 50 mM creatine sample was once diluted with 10% H_2O and once with D_2O, giving two different 45.0 mM creatine samples. The creatine used to make the samples was in the form of creatine monohydrate.

A.1.1 Buffer for 2K-EDTA-Plasma or similar (500 ml)

The serum buffer used were made with the following procedure. In the sample containing 10 mM phosphate concentration the buffer was further diluted with water containing 20% H_2O.

(a) 0.075 M $Na_2HPO_4 \times 7H_2O$ (=0.142 M without H_2O)

(b) Solution of 4% NaN_3 in H_2O

(c) TSP (=3-(trimethyl-silyl)propionic acid-d4, Aldrich 269913)

1. Dissolve 10.05 g $Na_2HPO_4 \times 7H_2O$in 380 ml H_2O
2. Add 0.4 g TSP (= 0.08%)
3. Mix very well (ultra sonic)
4. Add 5 ml of a 4% NaN_3/H_2O-solution
5. Adjust pH to 7.4 with 1M HCl (1M NaOH)
6. Fill it up to 400 ml with H_2O
7. Add 100 ml D_2O and mix very well

A.2 List of offset frequencies for the CEST experiment in Hz

-300000.0 -6000.0 -4800.0 -4200.0 -3600.0 -3300.0 -3000.0 -2700.0 -2400.0 -2100.0 -1800.0 -1500.0 -1200.0 -900.0 -600.0 -300.0 -240.0 -180.0 -120.0 -60.0 0.0 60.0 120.0 180.0 240.0 300.0 360.0 420.0 480.0 540.0 600.0 690.0 780.0 870.0 960.0 1050.0 1140.0 1230.0 1320.0 1410.0 1500.0 1590.0 1680.0 1770.0 1860.0 1950.0 2040.0 2130.0 2220.0 2310.0 2400.0 2490.0 2580.0 2670.0 2760.0 2850.0 2940.0 3300.0 3600.0 4200.0 4800.0 6000.0 300000.0

Appendix B

Results of saturation recovery

The saturation recovery sequence was run for all the different samples at all relevant temperatures, giving eight mono-exponential fits. These can be found in Figures B.1 to B.8.

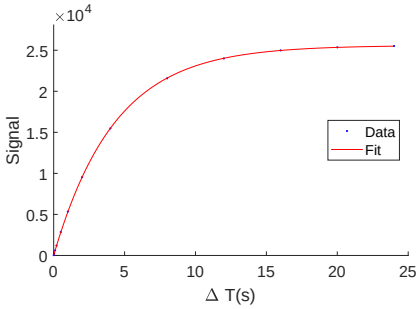

Figure B.1: Exponential fit of 10 mM creatine in a phosphate buffer at 310 K.

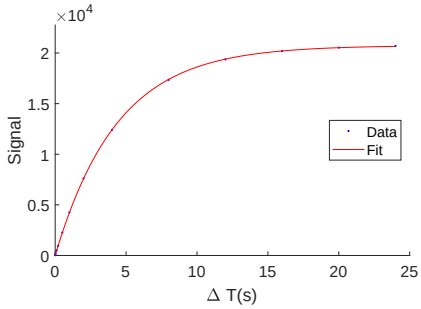

Figure B.2: Exponential fit of 10 mM glutamate in a phosphate buffer at 310 K.

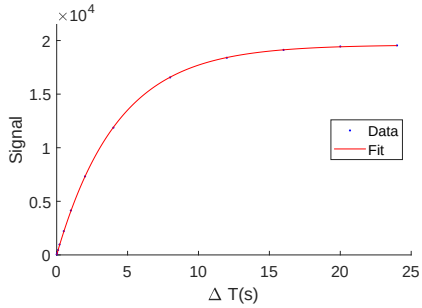

Figure B.3: Exponential fit of 10 mM myo-inositol in a phosphate buffer at 310 K.

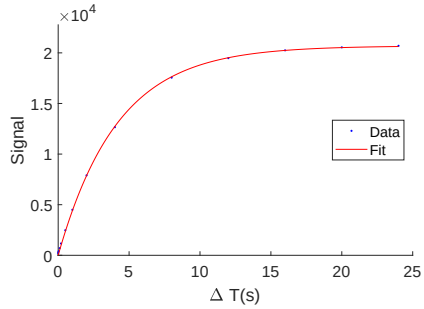

Figure B.4: Exponential fit of 10 mM glutamate and 10 mM creatine in a phosphate buffer at 310 K.

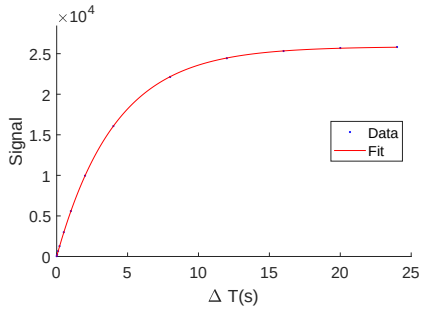

Figure B.5: Exponential fit of 10 mM creatine in a 90% H_2O/10% D_2O solution at 310 K.

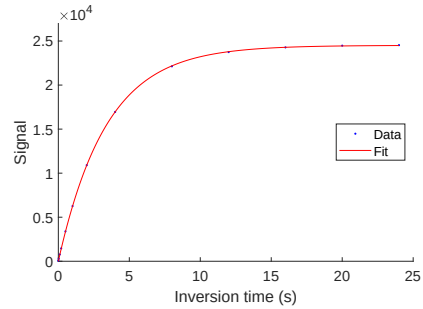

Figure B.6: Exponential fit of 47.5 mM creatine in a phosphate buffer at 298.1 K.

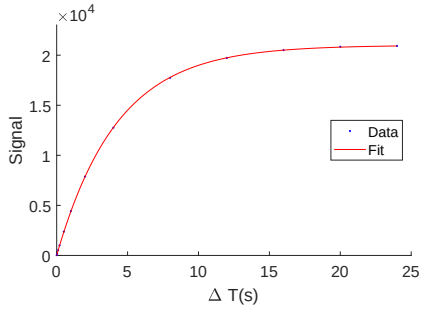

Figure B.7: Exponential fit of 45 mM creatine in a serum buffer containing 10 mM phosphate at 310 K.

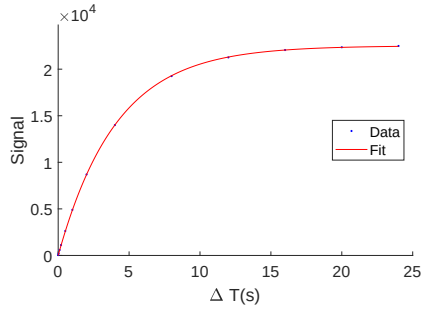

Figure B.8: Exponential fit of 45 mM creatine in a serum buffer containing 37.5 mM creatine at 310 K.

Appendix C

CEST spectra with varying SRD

CEST spectra were obtained on a sample of 47.5 mM creatine at 298.1 K for SR-CEST with varying spoiler recovery delays (SRD). The spectra created can be found in Figure C.1, with SRD = 1 ms, 100 ms, 500 ms, 1 s, 2 s, 3 s, 6 s and 16 s.

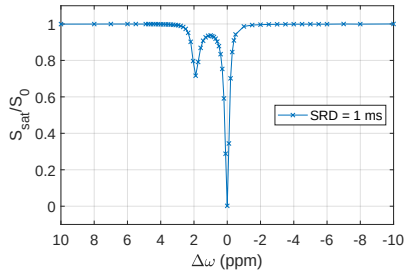

(a) SRD = 1 ms

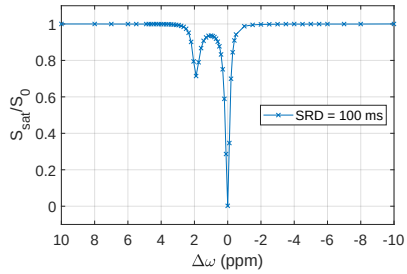

(b) SRD = 100 ms

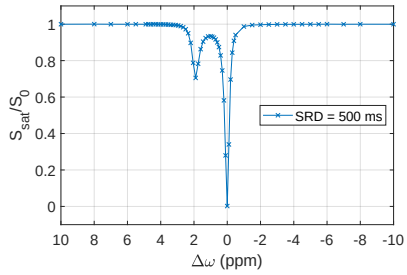

(c) SRD = 500 ms

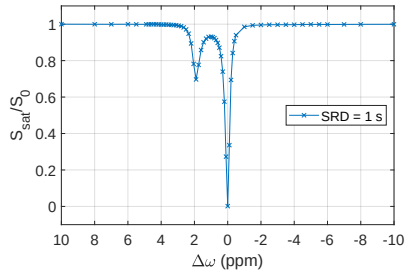

(d) SRD = 1 s

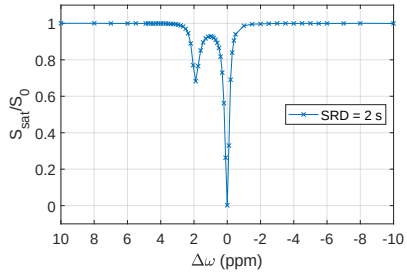

(e) SRD = 2 s

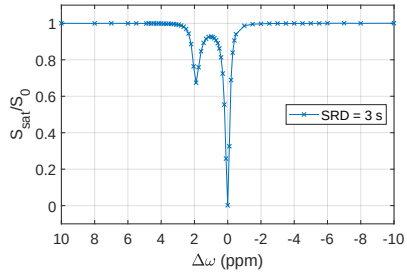

(f) SRD = 3 s

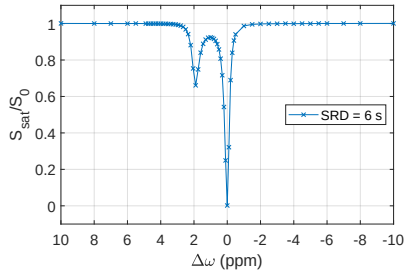

(g) SRD = 6 s

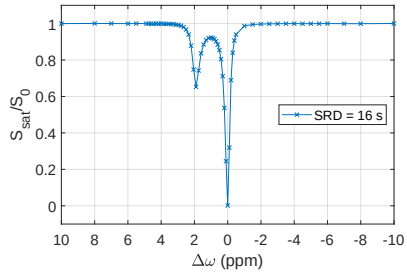

(h) SRD = 16 s

Figure C.1: CEST spectra obtained with SR-CEST using varying spoiler recovery delays (SRD). Temperature is 298.1 K, and the sample is 47.5 mM creatine in a phosphate buffer. B_1 = 1 µT.

Appendix D

BM fitted CEST spectra

In the following section all BM fitted CEST spectra in this thesis work can be found with corresponding residual plots.

D.1 Test and verification of the SR-CEST

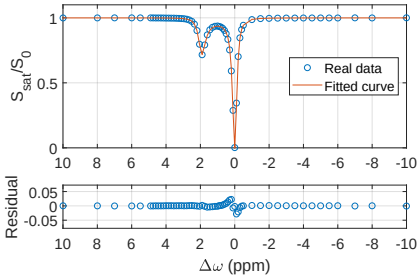

(a) SRD = 1 ms

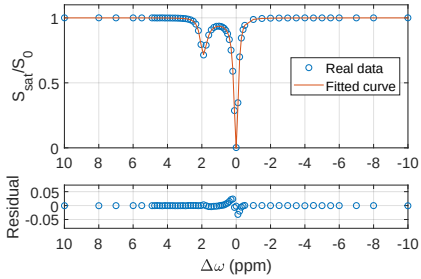

(b) SRD = 100 ms

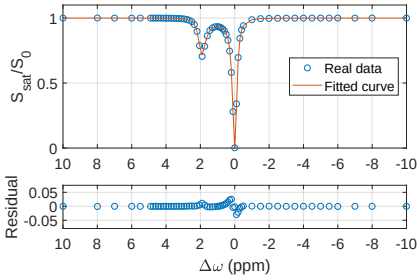

(c) SRD = 500 ms

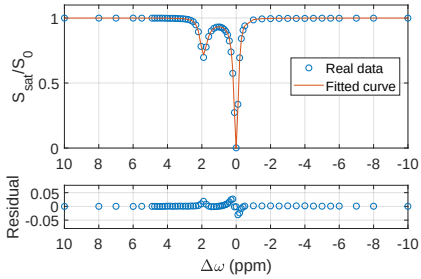

(d) SRD = 1 s

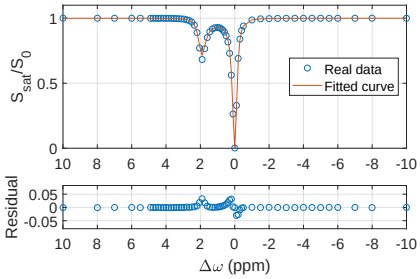

(e) SRD = 2 s

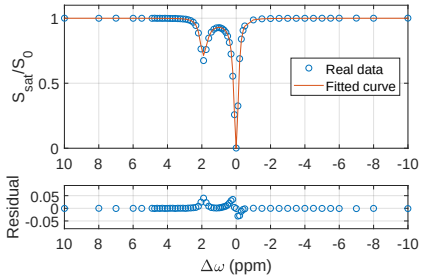

(f) SRD = 3 s

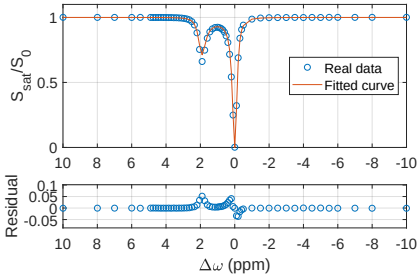

(g) SRD = 6 s

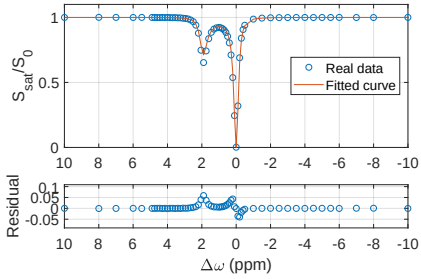

(h) SRD = 16 s.

Figure D.1: BM fitting for CEST spectra obtained with SR-CEST using varying spoiler recovery delays (SRD), and keeping concetrantion a fixed parameter. Temperature is 298.1 K, and the sample is 47.5 mM creatine in a phosphate buffer. B_1 = 1 µT.

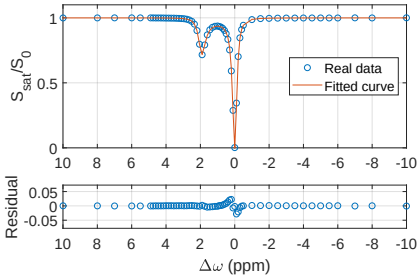

(a) SRD = 1 ms

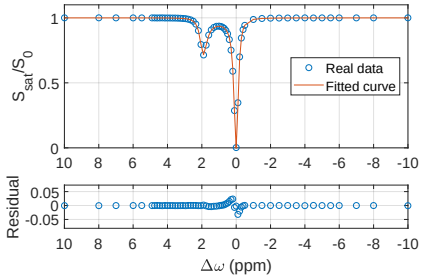

(b) SRD = 100 ms

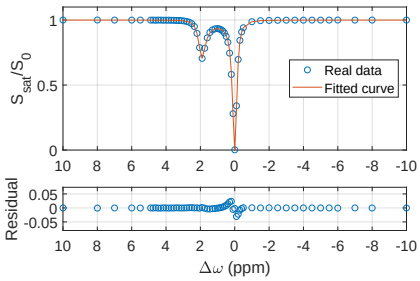

(c) SRD = 500 ms

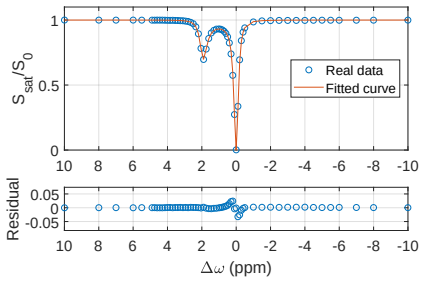

(d) SRD = 1 s

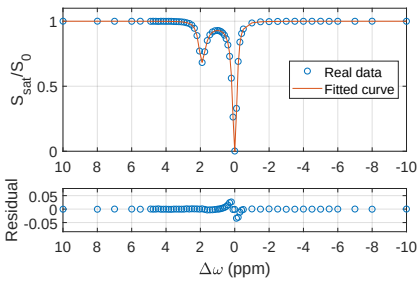

(e) SRD = 2 s

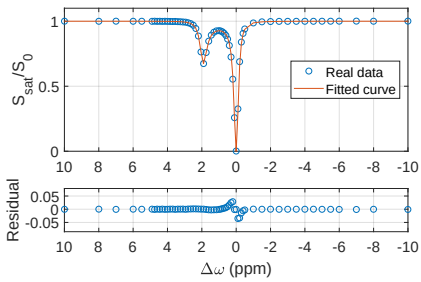

(f) SRD = 3 s

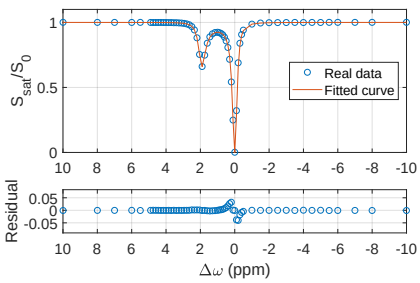

(g) SRD = 6 s

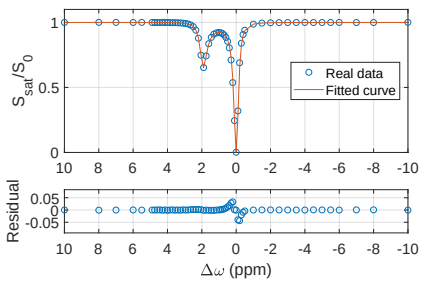

(h) SRD = 16 s.

Figure D.2: BM fitting for CEST spectra obtained with SR-CEST using varying spoiler recovery delays (SRD), and letting concetrantion of creatine vary between 30 and 70 mM. Temperature is 298.1 K, and the sample is 47.5 mM creatine in a phosphate buffer. $B_1 = 1$ µT.

D.2 Sample of 45 mM creatine without phosphate buffer

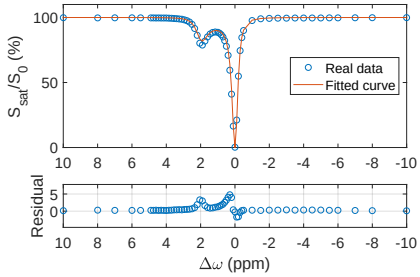

(a) $B_1 = 1$ µT.

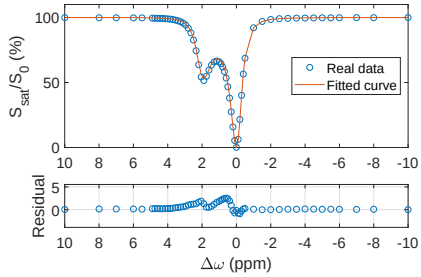

(b) $B_1 = 2$ µT.

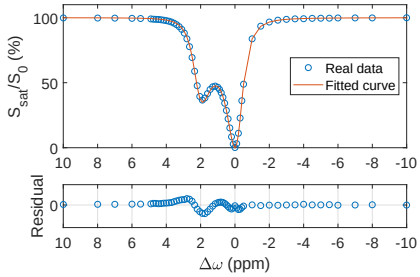

(c) $B_1 = 3$ µT.

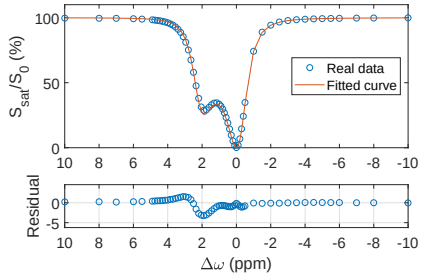

(d) $B_1 = 4$ µT.

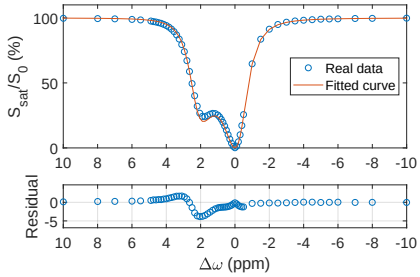

(e) $B_1 = 5$ µT.

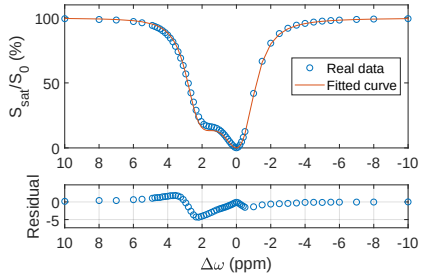

(f) $B_1 = 8$ µT.

Figure D.3: BM fitting for CEST spectra obtained with SR-CEST using an SRD = 200 ms with varying B_1. The temperature is 310 K, and the sample is 45 mM creatine in water with 10% D_2O.

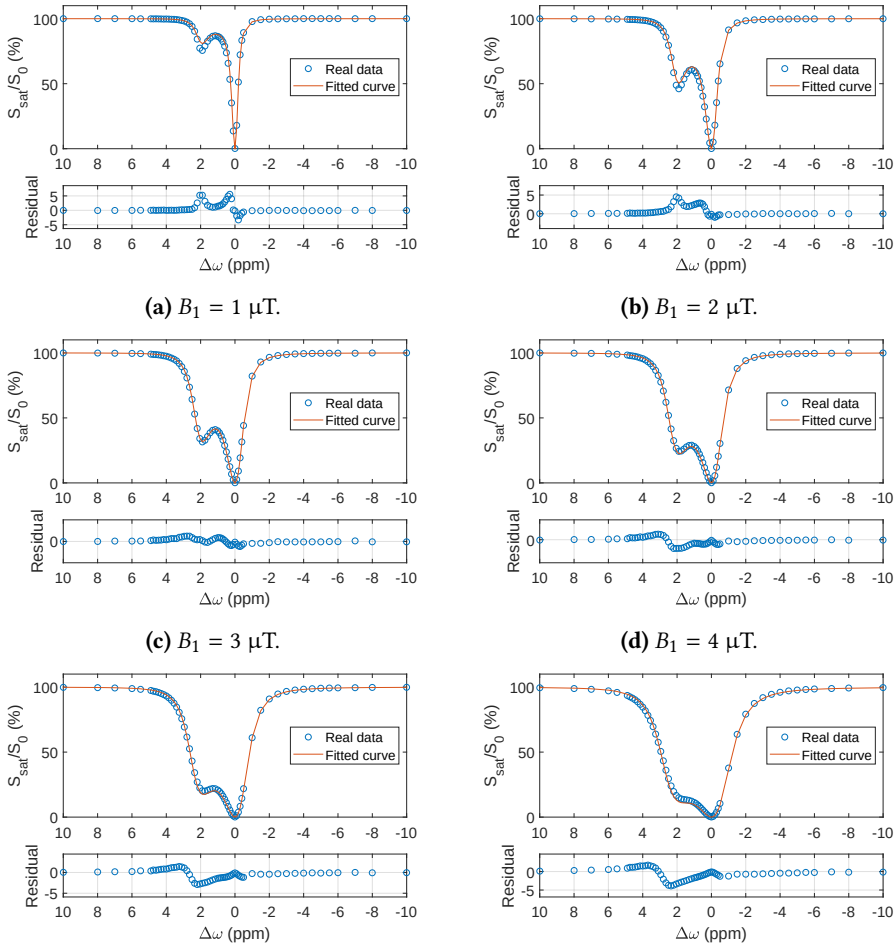

(a) $B_1 = 1$ µT. **(b)** $B_1 = 2$ µT.

(c) $B_1 = 3$ µT. **(d)** $B_1 = 4$ µT.

(e) $B_1 = 5$ µT. **(f)** $B_1 = 8$ µT.

Figure D.4: BM fitting for CEST spectra obtained with SR-CEST using an SRD = 4.1 s with varying B_1. The temperature is 310 K, and the sample is 45 mM creatine in water with 10% D_2O.

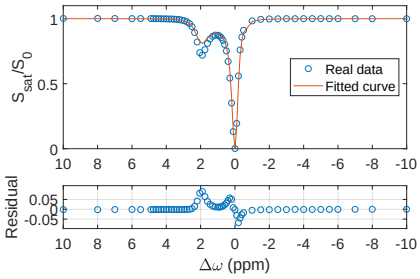

(a) $B_1 = 1$ µT.

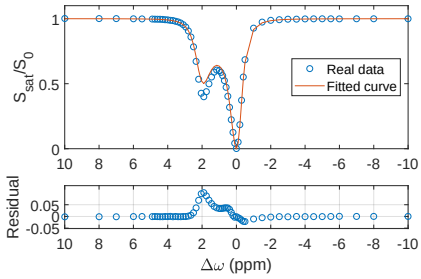

(b) $B_1 = 2$ µT.

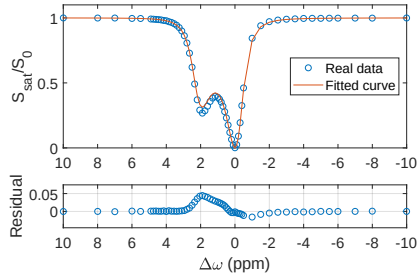

(c) $B_1 = 3$ µT.

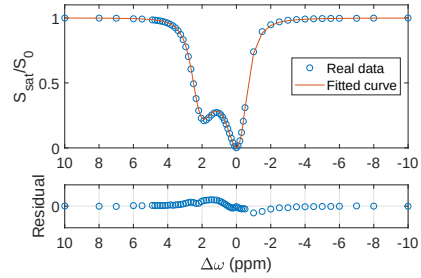

(d) $B_1 = 4$ µT.

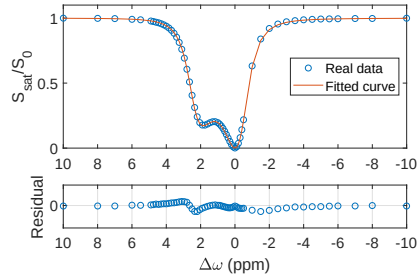

(e) $B_1 = 5$ µT.

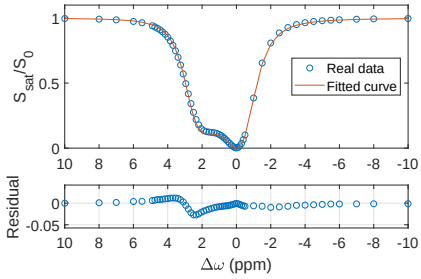

(f) $B_1 = 8$ µT.

Figure D.5: BM fitting for CEST spectra obtained with regular CEST with varying B_1. The temperature is 310 K, and the sample is 45 mM creatine in water with 10% D_2O.

D.3 Sample of 45 mM creatine with 10 mM phosphate buffer

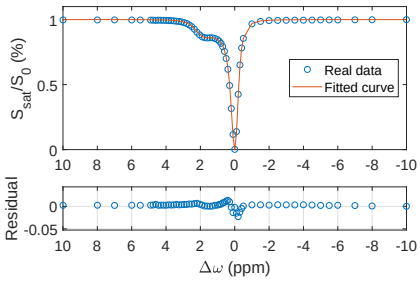

(a) $B_1 = 1$ µT.

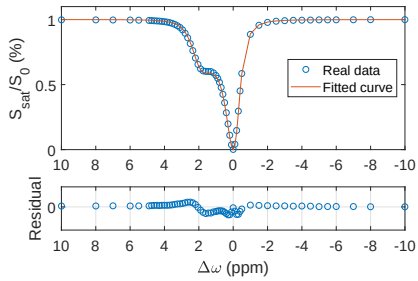

(b) $B_1 = 2$ µT.

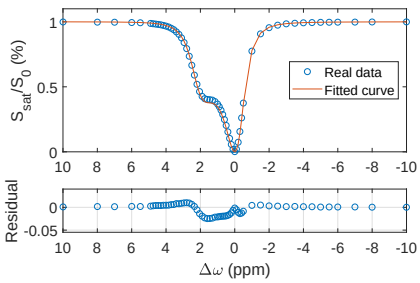

(c) $B_1 = 3$ µT.

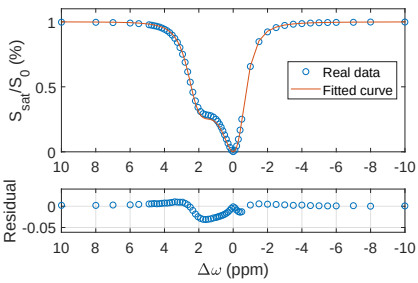

(d) $B_1 = 4$ µT.

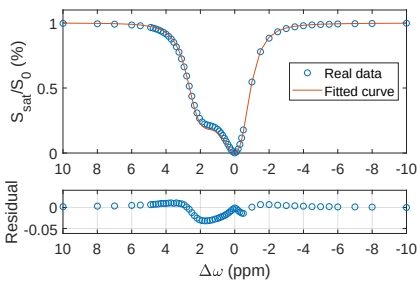

(e) $B_1 = 5$ µT.

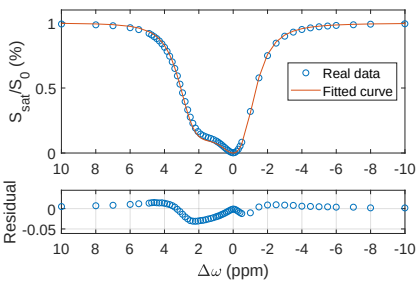

(f) $B_1 = 8$ µT.

Figure D.6: BM fitting for CEST spectra obtained with SR-CEST using an SRD = 200 ms with varying B_1. The temperature is 310 K, and the sample is 45 mM creatine in a buffer containing 10 mM phosphate.

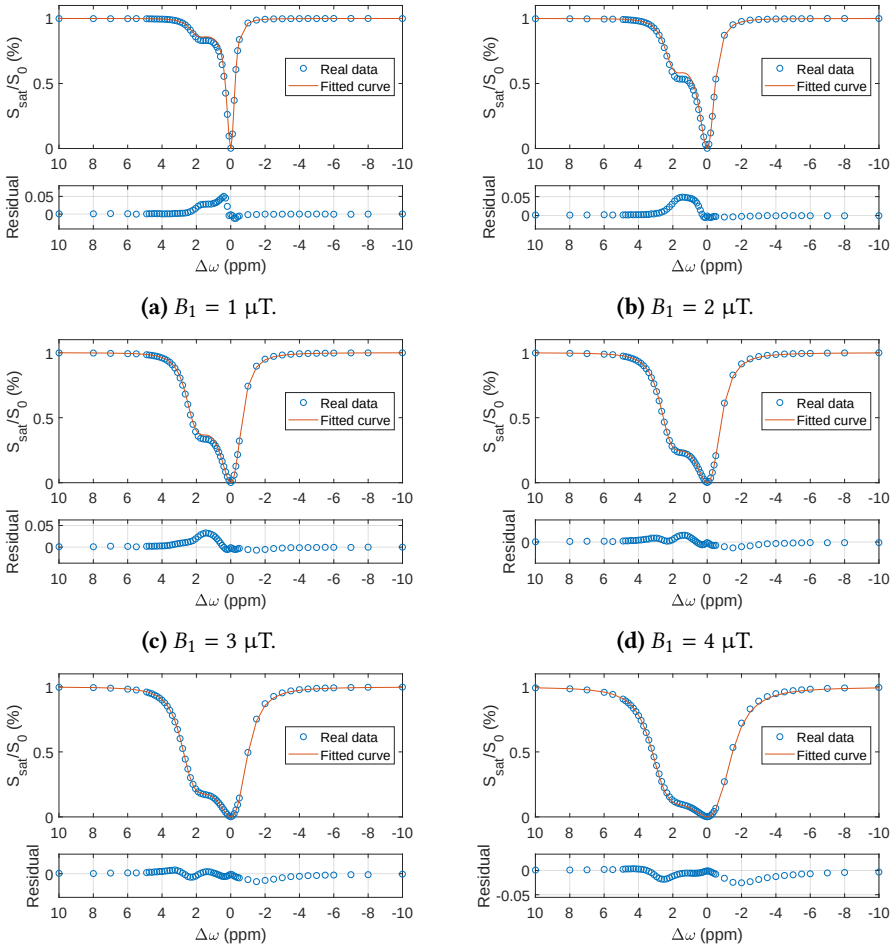

(a) $B_1 = 1$ µT. **(b)** $B_1 = 2$ µT.

(c) $B_1 = 3$ µT. **(d)** $B_1 = 4$ µT.

(e) $B_1 = 5$ µT. **(f)** $B_1 = 8$ µT.

Figure D.7: BM fitting for CEST spectra obtained with SR-CEST using an SRD = 4.3 s with varying B_1. The temperature is 310 K, and the sample is 45 mM creatine in a buffer containing 10 mM phosphate.

D.4 Sample of 45 mM creatine with 37.5 mM phosphate buffer

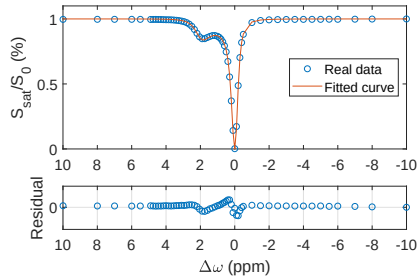

(a) $B_1 = 1$ µT.

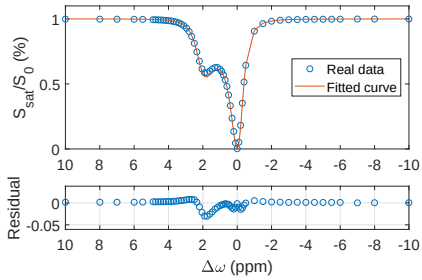

(b) $B_1 = 2$ µT.

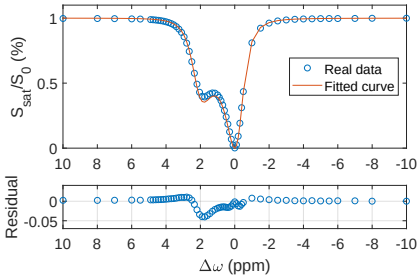

(c) $B_1 = 3$ µT.

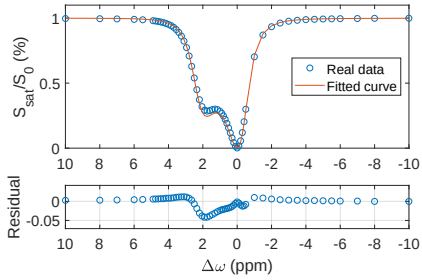

(d) $B_1 = 4$ µT.

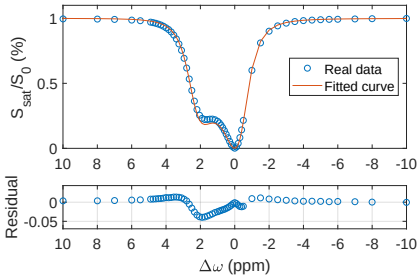

(e) $B_1 = 5$ µT.

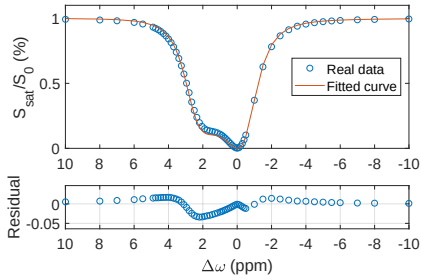

(f) $B_1 = 8$ µT.

Figure D.8: BM fitting for CEST spectra obtained with SR-CEST using an SRD = 200 ms with varying B_1. The temperature is 310 K, and the sample is 45 mM creatine in a buffer containing 37.5 mM phosphate.

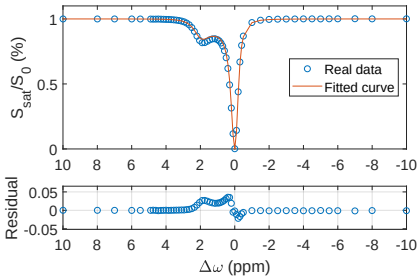

(a) $B_1 = 1$ µT.

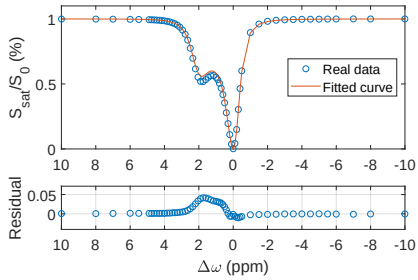

(b) $B_1 = 2$ µT.

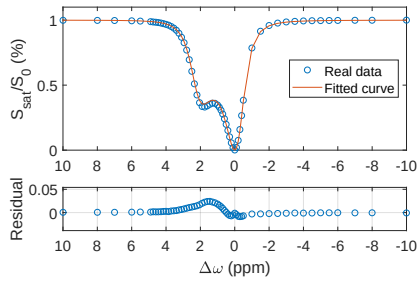

(c) $B_1 = 3$ µT.

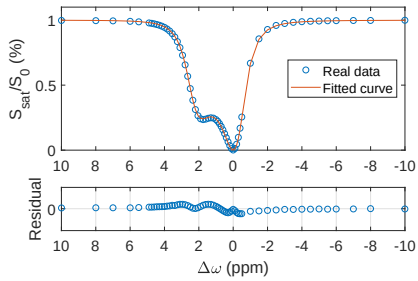

(d) $B_1 = 4$ µT.

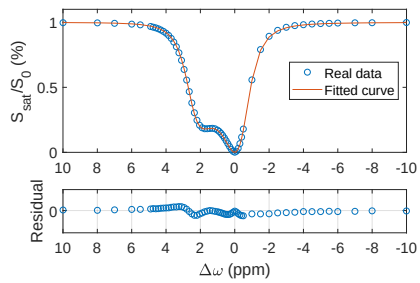

(e) $B_1 = 5$ µT.

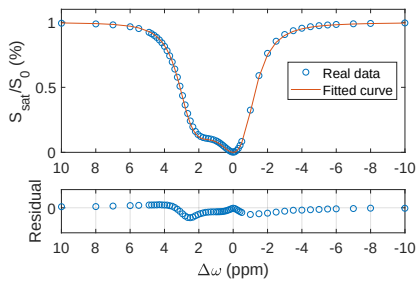

(f) $B_1 = 8$ µT.

Figure D.9: BM fitting for CEST spectra obtained with SR-CEST using an SRD = 4.1 s with varying B_1. The temperature is 310 K, and the sample is 45 mM creatine in a buffer containing 37.5 mM phosphate.

D.5 Sample of 10 mM creatine

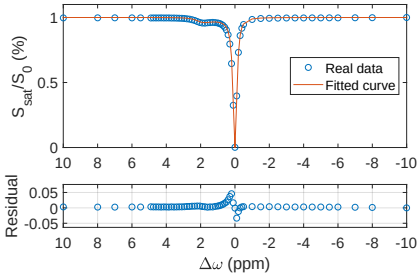

(a) $B_1 = 1$ µT.

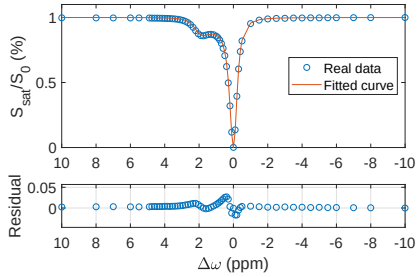

(b) $B_1 = 2$ µT.

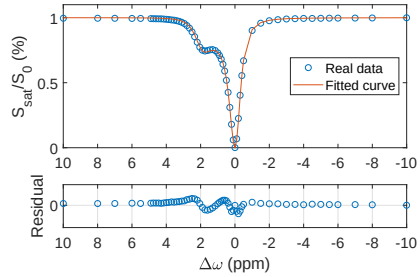

(c) $B_1 = 3$ µT.

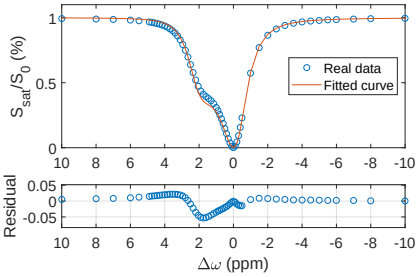

(d) $B_1 = 8$ µT.

Figure D.10: BM fitting for CEST spectra obtained with SR-CEST using an SRD of 200 ms with varying B_1. The temperature is 310 K, and the sample is 10 mM creatine in a phosphate buffer.

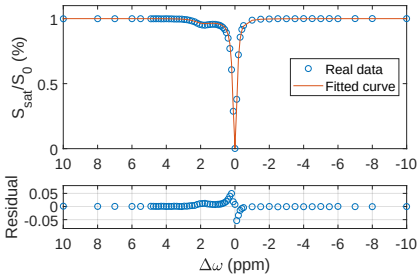

(a) $B_1 = 1$ µT.

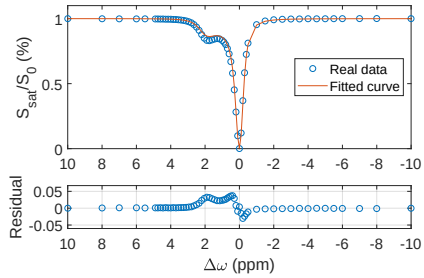

(b) $B_1 = 2$ µT.

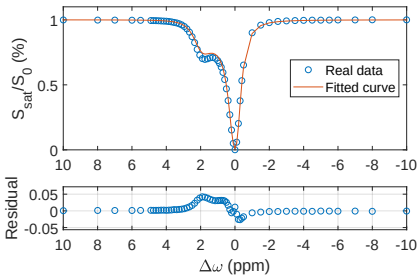

(c) $B_1 = 3$ µT.

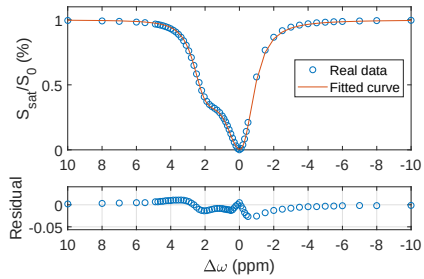

(d) $B_1 = 8$ µT.

Figure D.11: BM fitting for CEST spectra obtained with SR-CEST using an SRD of 4.3 s with varying B_1. The temperature is 310 K, and the sample is 10 mM creatine in a phosphate buffer.

D.6 Sample of 10 mM myo-inositol

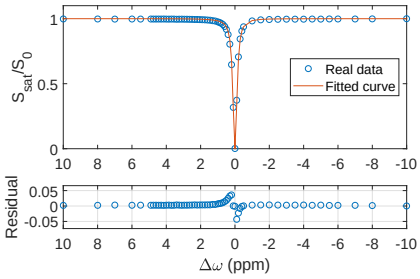

(a) $B_1 = 1$ µT.

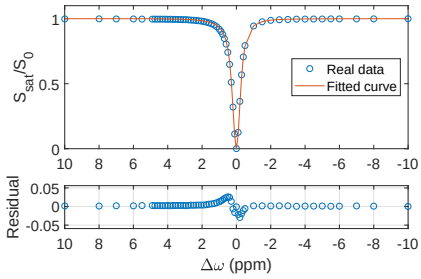

(b) $B_1 = 2$ µT.

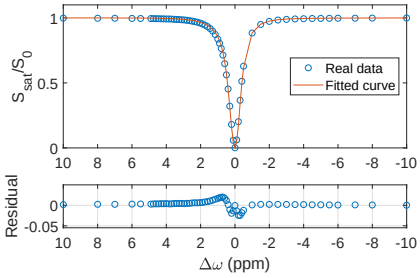

(c) $B_1 = 3$ µT.

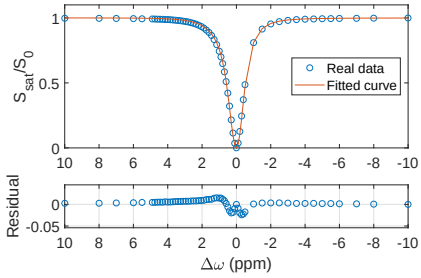

(d) $B_1 = 4$ µT.

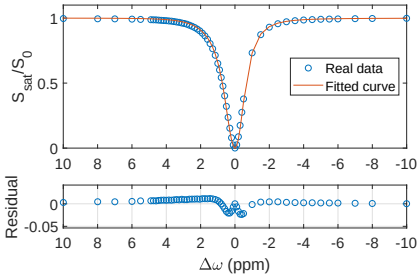

(e) $B_1 = 5$ µT.

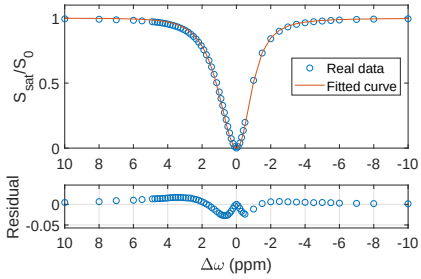

(f) $B_1 = 8$ µT.

Figure D.12: BM fitting for CEST spectra obtained with SR-CEST using an SRD of 200 ms with varying B_1. The temperature is 310 K, and the sample is 10 mM myo-inositol in a phosphate buffer.

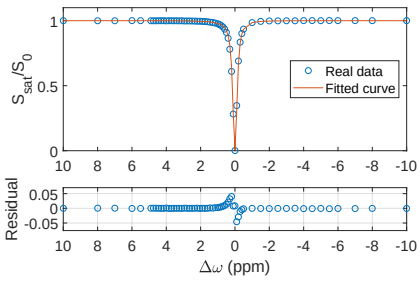

(a) $B_1 = 1$ µT.

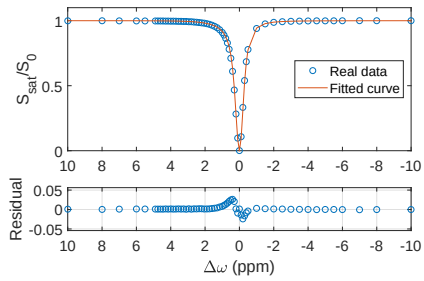

(b) $B_1 = 2$ µT.

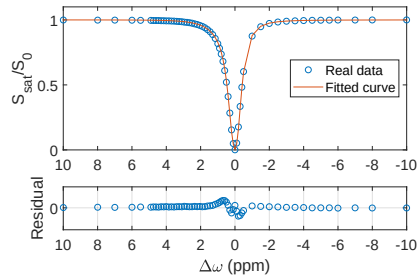

(c) $B_1 = 3$ µT.

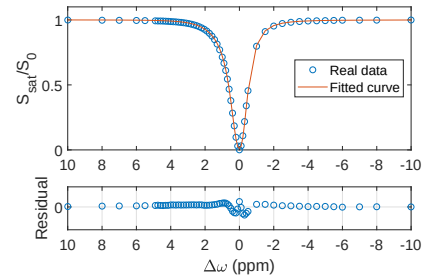

(d) $B_1 = 4$ µT.

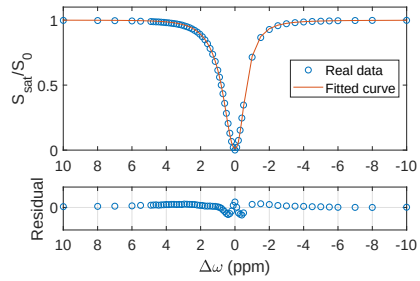

(e) $B_1 = 5$ µT.

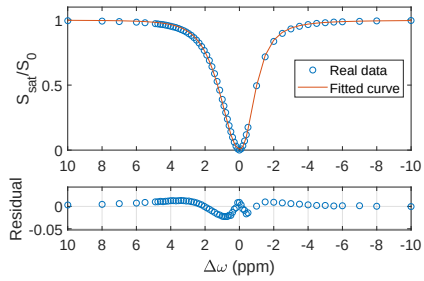

(f) $B_1 = 8$ µT.

Figure D.13: BM fitting for CEST spectra obtained with SR-CEST using an SRD of 4.3 s with varying B_1. The temperature is 310 K, and the sample is 10 mM myo-inositol in a phosphate buffer.

D.7 Sample of 10 mM glutamic acid

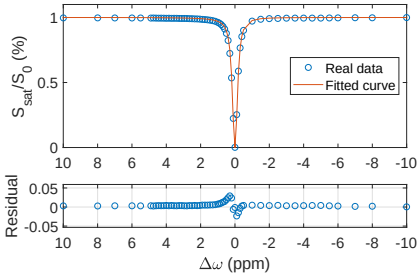

(a) $B_1 = 1$ µT.

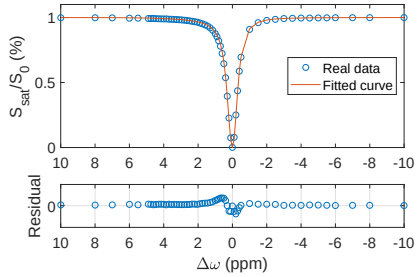

(b) $B_1 = 2$ µT.

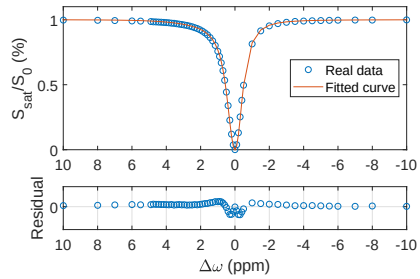

(c) $B_1 = 3$ µT.

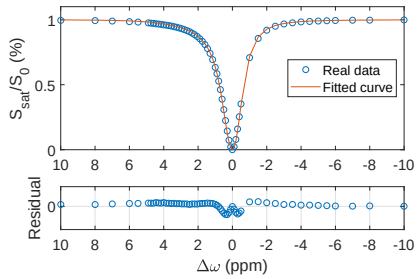

(d) $B_1 = 4$ µT.

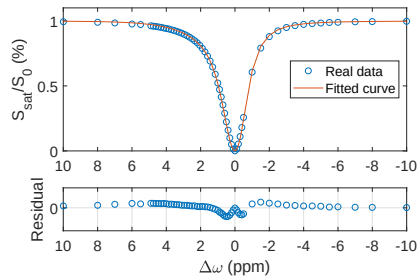

(e) $B_1 = 5$ µT.

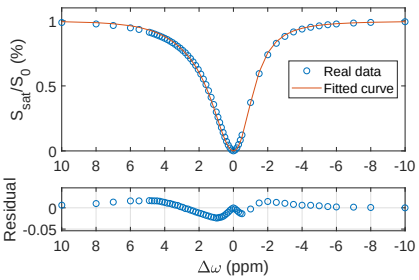

(f) $B_1 = 8$ µT.

Figure D.14: BM fitting for CEST spectra obtained with SR-CEST using an SRD of 200 ms with varying B_1. The temperature is 310 K, and the sample is 10 mM glutamic acid in a phosphate buffer.

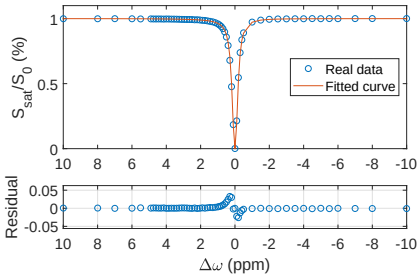

(a) $B_1 = 1$ µT.

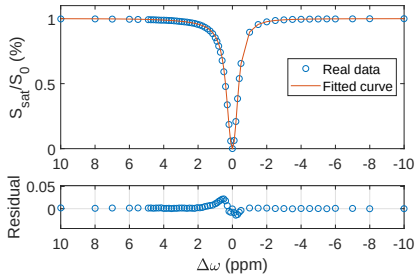

(b) $B_1 = 2$ µT.

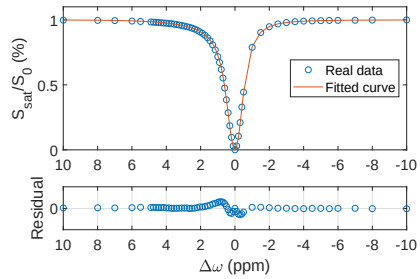

(c) $B_1 = 3$ µT.

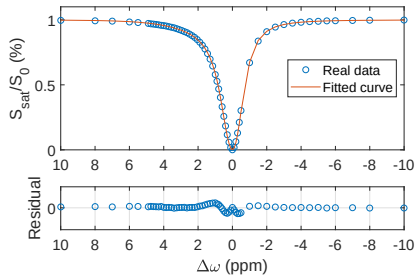

(d) $B_1 = 4$ µT.

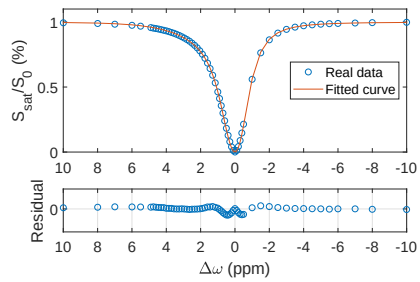

(e) $B_1 = 5$ µT.

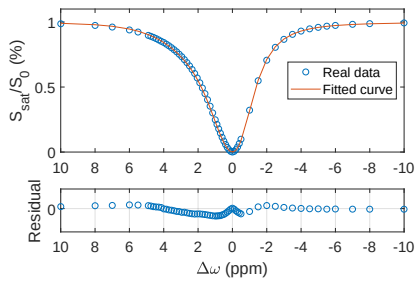

(f) $B_1 = 8$ µT.

Figure D.15: BM fitting for CEST spectra obtained with SR-CEST using an SRD of 4.4 s with varying B_1. The temperature is 310 K, and the sample is 10 mM glutamic acid in a phosphate buffer.

D.8 Sample of 10 mM creatine and 10 mM glutamic acid

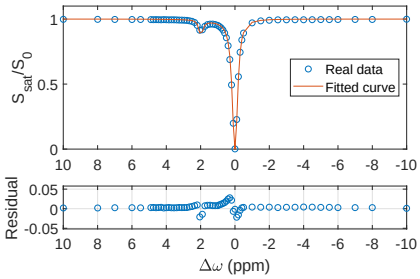

(a) $B_1 = 1$ µT.

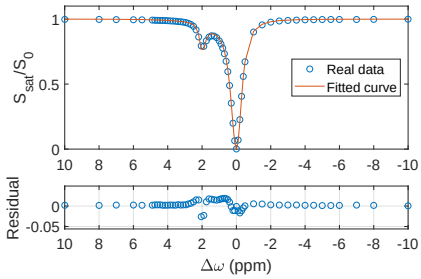

(b) $B_1 = 2$ µT.

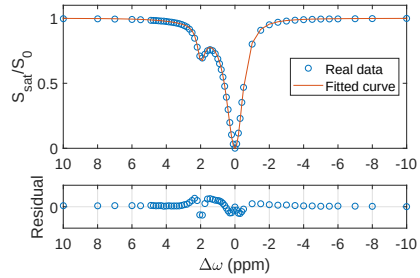

(c) $B_1 = 3$ µT.

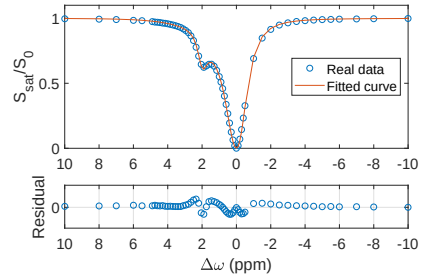

(d) $B_1 = 4$ µT.

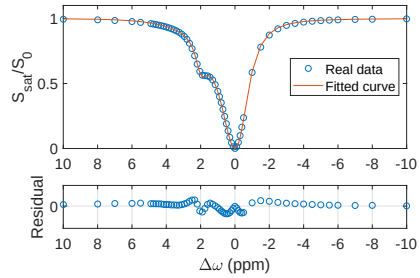

(e) $B_1 = 5$ µT.

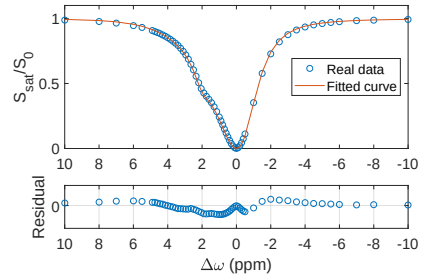

(f) $B_1 = 8$ µT.

Figure D.16: BM fitting for CEST spectra obtained with SR-CEST using an SRD of 200 ms with varying B_1. The temperature is 310 K, and the sample is 10 mM glutamic acid and 10 mM creatine in a phosphate buffer.

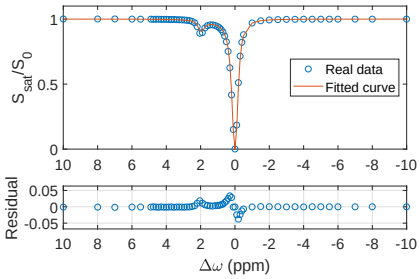

(a) $B_1 = 1$ µT.

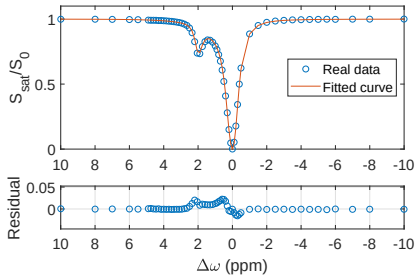

(b) $B_1 = 2$ µT.

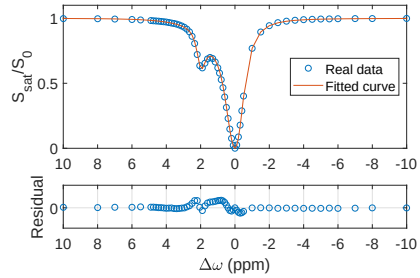

(c) $B_1 = 3$ µT.

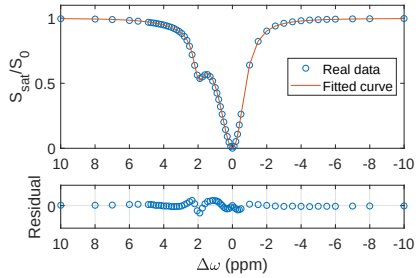

(d) $B_1 = 4$ µT.

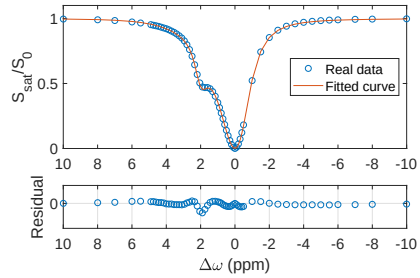

(e) $B_1 = 5$ µT.

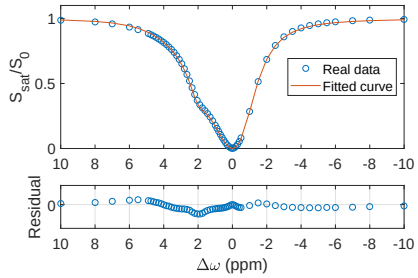

(f) $B_1 = 8$ µT.

Figure D.17: BM fitting for CEST spectra obtained with regular CEST with varying B_1. The temperature is 310 K, and the sample is 10 mM glutamic acid and 10 mM creatine in a phosphate buffer.

Appendix E

Matlab script

A script conducting a numerical BM fit of CEST spectra generated *in vivo*, simultaneously across varying pH and saturation field strength B_1, was provided by Vitaliy Khlebnikov at University Medical Center Utrecht. This script was further modified, adjusted to the *in vitro* setting of this work. It was also modified to account for the new spoiler recovery approach SR-CEST, and to only fit simultaneously across varying B_1.

Below is a particular script used for 10 mM creatine with SRD = 200 ms, as in Section 4.5.1. To use this script on CEST spectra generated for other metabolites certain values have to be exchanged: Water T_1, metabolite concentration, number of labile protons and boundary values and initial guesses for water T_2 and metabolite resonance frequency, T_1, T_2 and exchange rate.

To fit a spectrum generated with regular CEST some justifications have to be made, but the scripts are overall similar. This is why a regular CEST script is not provided for here.

```
function BMfit_creatine_200ms
%% This function generates a numerical BM fit for SR-CEST spectra generated
%% for 10 mM creatine, with SRD = 200 ms. The fit is conducted simultaneosly
%% for multiple saturation field strengths.

fieldStrength = 600.23;
T1_par='free';

simulation_start=tic;
Path=pwd; %path is current folder
NewPath=strcat(Path,'/','fit_200ms');
```

```
offset=[];

load offset %List of offset frequencies

if ~exist(strcat(NewPath,'/','multistart','_',T1_par),'dir')
    mkdir(NewPath,strcat('multistart','_',T1_par))
else
    rmdir(strcat(NewPath,'/','multistart','_',T1_par),'s')
    mkdir(NewPath,strcat('multistart','_',T1_par))
end

copyfile('BMfit_creatine_200ms.m',strcat(NewPath,'/','multistart','_',
    T1_par))

metabolite_name={'200ms'}; %

folders_b1=[4:-1:1]; % Each folder corresponds to a SR-CEST spectrum
    generated for a certain B1
b1_ut=[8 3 2 1]; % Which saturation field strength corresponds to each
    folder

fits_n_b1=length(b1_ut);
fits_n_srd=1;

power=cell(1,length(b1_ut));
for ii=1:length(b1_ut)
    power{ii}=strcat(num2str(b1_ut(ii)),'ut');
end


t_srd=0.2; %The SRD, set to 200 ms.

par=[];
ci=[];
delta=[];
T_1=[];


T_1 = 4.31; %Water T1 of the sample, measured with saturation recovery.


%% Loading all SR-CEST spectra
cest_data=zeros(length(offset),fits_n_srd*fits_n_b1);
title_fig=cell(fits_n_srd*fits_n_b1);
count=0;
for n_srd = 1:fits_n_srd
```

```
    for n_b1=1:fits_n_b1
        count=count+1;
        cd(strcat(Path,'/', metabolite_name{n_srd},'/',num2str(folders_b1(
    n_b1))))
        load('data_real_cest','spec');
        cest_data(:,count)=spec;
        title_fig{count}=strcat(metabolite_name{n_srd},'_',power{n_b1});
    end
end


cd(strcat(NewPath,'/',strcat('multistart','_',T1_par)))

%% Boundary values for the fit

%  watert2       exchrate  resonance     mett2       mett1
x0 = [  T_1        810       2             T_1           T_1   ];
lb = [  0.4        200         1.7           0.4         2       ];
ub = [  T_1     3000      2.3            T_1         T_1];


cest_data=cest_data(2:end-1,:);
yy=cest_data;
offset_w=offset(2:end-1)/fieldStrength; % real data

weights=ones(length(offset_w),fits_n_srd*fits_n_b1); %All weights are set
    to 1
zcal=zeros(length(offset_w),fits_n_srd*fits_n_b1);
[~, n1]=min(abs(1.0-offset_w));
[~, n2]=min(abs(5-offset_w));
%weights(n1:n2,:)=10e8; %Selected weights can be set here


%% Conducting the fit with lsqcurvefit
options = optimset('MaxFunEvals', 1000, 'MaxIter', 500, 'TolFun',1e-6,'
    TolX',1e-6, 'UseParallel','always', 'display', 'off');
[x,~,RESIDUAL,~,OUTPUT,~,J]= lsqcurvefit(@B1amp_function, x0, offset_w, yy
    .*weights, lb,ub,options);


save cest_data cest_data

%% Printing out estimated parameters and plotting the resulting fittings
CI = nlparci(x,RESIDUAL,'jacobian',J);
feil = [x(1) - CI(1,1),x(2) - CI(2,1),x(3) - CI(3,1),x(4) - CI(4,1),x(5) -
     CI(5,1)];
```

```
fprintf(['k_sw in Hz: %f pm %f \n Offset in ppm: %f pm %f \n',...
    'T2_solute: %f pm %f \n T2_water: %f pm %f \n T1_solute: %f pm %f \n'
    ], ...
    x(2), feil(2), x(3), feil(3), x(4), feil(4), x(1), feil(1), x(5), feil
    (5));

count=0;
for n_srd = 1:fits_n_srd
    for n_b1=1:fits_n_b1
        count=count+1;
        zcal(:,count)  = cest_sim_slave_creatine(x, offset_w, count,t_srd,
     T1_par,fits_n_srd,b1_ut);

        pos1 = [0.15 0.45 0.8 0.5];
        pos2 = [0.15 0.17 0.8 0.15];
        error(:, count) = (zcal(:,count)- yy(:,count));

        errorLimMax = max(error(:, count))+0.03;
        errorLimMin = min(error(:, count))-0.03;


        h=figure(count);
        grid on, box on
        subplot('Position',pos1)
        plot(offset_w, yy(:,count), 'o');
        hold on
        plot(offset_w, zcal(:,count),'linewidth', 1);
        set(gca, 'xdir','reverse','fontsize', 15, 'XTick', -10:2:10)
        ylabel('S_{sat}/S_0 (%)')
        legend({'Real data','Fitted curve'}, 'Location','east')
        axis([-10 10 0 1.10])


        subplot('Position',pos2)
        plot(offset_w,zcal(:,count)-yy(:,count), 'o')
        hold on
        grid on
        xlabel('\Delta\omega (ppm)')
        ylabel('Residual');
        set(gca, 'xdir','reverse','fontsize', 15, 'XTick', -10:2:10, '
    YTick', -0.05:0.05:0.05)
        axis([-10 10 errorLimMin errorLimMax])


        set(h,'name',title_fig{count},'numbertitle','off')
        fig = gcf;
```

```
        fig.PaperUnits = 'inches';
        fig.PaperPosition = [0 0 6 4];
        saveas(h,title_fig{count},'pdf')

    end
end

figure;
hold on, box on, grid on
for i = 1:4
    yl1 = yline(-i*0.1,'HandleVisibility','off');
    yl2 = yline(-i*0.1 + -0.05,'HandleVisibility','off');
    yl1.Alpha = 0.2;
    yl2.Alpha = 0.2;
    scatter(offset_w, error(:,i)-i*0.1, 'filled', 'MarkerFaceAlpha', .6)
end
set(gca, 'xdir','reverse','fontsize', 18, 'XTick', -10:2:10, 'YTick', [])
axis([-10 10 -0.475 -0.025])
yl3 = yline(0.05,'HandleVisibility','off');
yl3.Alpha = 0.2;
legend('1 uT', '2 uT', '3 uT','4 uT')
xlabel('\Delta\omega (ppm)')
ylabel('CEST_{fitted}-CEST_{experimental}')
fig = gcf;
fig.PaperUnits = 'inches';
fig.PaperPosition = [0 0 6 6];
cd(Path)
saveas(fig, 'residualsCr200', 'pdf')



ElapsedScript=toc(simulation_start);
fprintf('Elapsed time is %d minutes and %f seconds\n', floor(ElapsedScript
    /60),rem(ElapsedScript,60))
%display('Statistics')


function spectra=B1amp_function(x, offset_w)
        spectra=zeros(length(offset_w),size(cest_data,2));
        B1_n_2=0;
        parfor B1_n_2=1:size(cest_data,2)
            spectra(:,B1_n_2)=cest_sim_slave_creatine(x, offset_w, B1_n_2,
     t_srd, T1_par,fits_n_srd,b1_ut).*weights(:,B1_n_2);
        end
    end
end
```

```
182
183
184 function varargout=cest_sim_slave_creatine(x, offset_w,B1_n_2,t1_sr,
        T1_par,fits_n_srd,b1_ut)
185 concentration = 9.9712; % Concentration of creatine in mM
186 T1w = 4.31; %T1 of water in s
187 count2 = 1;
188 count=B1_n_2;
189
190 if count > length(b1_ut)
191     count2 = count2+1;
192     B1amp = b1_ut(count-length(b1_ut));
193 else
194     B1amp=b1_ut(count);
195 end
196 np=4; %Number of labile protons
197
198 pools={...
199     {'H2O',T1w, x(1), 0, 2*55.15*1000, 0}...
200     {'met',x(5), x(4), x(3), np*concentration, x(2)}...
201     };
202
203
204 offset=[offset_w' 499.97];
205 fs=14.1; %Spectrometer field strength in T
206 spoilRec = t1_sr(count2);
207
208 cwpe=B1amp;
209 pulse_cest_dur(:,1)=cwpe*42.576;
210 pulse_cest_dur(:,2)=5;
211
212 name=cell(1,length(pools));
213 t1=zeros(1,length(pools));
214 t2=zeros(1,length(pools));
215 w_pool_ppm=zeros(1,length(pools));
216 Con=zeros(1,length(pools));
217 Rate=zeros(1,length(pools));
218 C=zeros(1,length(pools));
219 Ca=zeros(1,length(pools)-1);
220 k1=zeros(1,length(pools));
221 k2=zeros(1,length(pools));
222
223 for ii=1:length(pools)
224     name{ii}=pools{ii}{1};
225     t1(ii)=pools{ii}{2};
226     t2(ii)=pools{ii}{3};
```

```
227     w_pool_ppm(ii)=pools{ii}{4};
228     Con(ii)=pools{ii}{5};
229     Rate(ii)=pools{ii}{6};
230 end
231
232 estCon = (1- exp(-(pulse_cest_dur(:,2)+spoilRec)/t1(1))); %Regained net
        magnetization after gradient spoiling
233
234 Con(:)=Con(:)./(Con(1)*estCon);
235 C(2:end)=Rate(2:end);
236 Ca=Con.*C;
237 C(1)=sum(Ca);
238 k1=1./t1+C;
239 k2=1./t2+C;
240 C=C(2:end);
241 Ca=Ca(2:end);
242
243 % w should be in rad/s
244 ww=offset.*fs.*42.576.*2.*pi;
245 w_pool=w_pool_ppm*fs*42.576*2*pi;
246
247 Za=zeros(length(offset),1);
248
249 b=[zeros(1,length(pools)*2) Con./t1]';
250
251 for n=1:length(ww)
252     y=zeros(1,length(pools)*3);
253     w=ww(n);
254
255     %% saturation
256     expmA_cest_dur = zeros(1,length(pools)*3,length(pools)*3);
257     Ainvbm_cest_dur = zeros(1, length(pools)*3);
258
259     m=1;
260     w1=2.0*pi*pulse_cest_dur(m,1);
261     add_lineshape=zeros(1,length(pools));
262
263     % diagonal
264     A=zeros(length(pools)*3,length(pools)*3);
265     A=A+diag([-k2 -k2 -(k1+add_lineshape)]);
266
267     % off diagonals
268     for ii=1:length(pools)-1
269         upperC=repmat([C(ii) zeros(1,length(pools)-1)],[1,3]);
270         upperC=upperC(1:end-ii);
271         A=A+diag(upperC,ii);
```

```
272
273         lowerC=repmat([Ca(ii) zeros(1,length(pools)-1)],[1,3]);
274         lowerC=lowerC(1:end-ii);
275         A=A+diag(lowerC,-ii);
276     end
277     A=A+diag([-(w_pool-w) repmat(-w1,[1,length(pools)])],length(pools));
278     A=A+diag([(w_pool-w) repmat(w1,[1,length(pools)])],-length(pools));
279
280     saveA = A;
281
282     %% Spoiler recovery
283
284     A(A==w1)=0;
285     A(A==-w1)=0;
286
287     [T,D] = eig(A);
288     eAt = T*diag(exp(diag(D)*spoilRec))/T;
289     expmA_spoilRec=abs(eAt);
290     Ainvbm_spoilRec = A\b;
291
292     y = expmA_spoilRec*(y+Ainvbm_spoilRec)-Ainvbm_spoilRec; % recovery
293
294     A = saveA;
295
296     %% Saturation
297     [T,D] = eig(A);
298     eAt = T*diag(exp(diag(D)*pulse_cest_dur(m,2)))/T;
299     expmA_cest_dur(m,:,:)=abs(eAt);
300     Ainvbm_cest_dur(m,:) = A\b;
301
302     y = reshape(expmA_cest_dur(m,:,:),[length(pools)*3, length(pools)*3])
        *(y+Ainvbm_cest_dur(m,:)')-Ainvbm_cest_dur(m,:)';
303
304     y(1:length(pools)*2)=0; % spoiling
305
306
307     %% The magnetization from the water pool
308     Za(n) = abs(y(length(pools)*2+1));
309
310 end
311
312
313 Za_new=Za./Za(end);
314 Za_new(isnan(Za_new)) = 0;
315 Za_new(~isfinite(Za_new))=0;
316 varargout{1}=Za_new(1:end-1);
```

```
317 clearvars -except varargout
318 end
```